

LA-UR-21-22406

Approved for public release; distribution is unlimited.

Title: PHELIX Shallow Cassette Liner Performance Tests 1 and 2 Post-Shot
Simulation Report

Author(s): Zocher, Marvin Anthony
Rousculp, Christopher L.

Intended for: Report

Issued: 2021-03-10

Disclaimer:

Los Alamos National Laboratory, an affirmative action/equal opportunity employer, is operated by Triad National Security, LLC for the National Nuclear Security Administration of U.S. Department of Energy under contract 89233218CNA000001. By approving this article, the publisher recognizes that the U.S. Government retains nonexclusive, royalty-free license to publish or reproduce the published form of this contribution, or to allow others to do so, for U.S. Government purposes. Los Alamos National Laboratory requests that the publisher identify this article as work performed under the auspices of the U.S. Department of Energy. Los Alamos National Laboratory strongly supports academic freedom and a researcher's right to publish; as an institution, however, the Laboratory does not endorse the viewpoint of a publication or guarantee its technical correctness.

PHELIX
Shallow Cassette Liner Performance
Tests 1 and 2
Post-Shot Simulation Report

Marvin A. Zocher and Christopher L. Rousculp

March 01, 2021

1 Introduction

PHELIX shallow cassette liner performance Tests 1 (PHELIX No. 151) and 2 (PHELIX No. 156) were conducted on August 07, 2020, and September 16, 2020, respectively. The primary purpose for these tests was to assess liner performance within the new shallow cassette PHELIX design configuration. Specific goals included: (1) an assessment of liner performance in terms of velocity and symmetry (both axial and azimuthal), and (2) an assessment of our ability to accurately predict liner performance. Test 1 was conducted with a driving potential of 70 kV. Test 2 was conducted with a driving potential of 75 kV.

The new shallow cassette configuration was designed with the following objectives in mind: (1) improved containment/confinement capabilities, and (2) ease of installation and removal. In this new design the upper and lower conductors are now of approximately equal mass and thickness with the liner and target region located between the two rather than in an elevated position. This makes for a more compact overall assembly. It also allows for a more efficient use of mass for the inhibition of motion. Note that the power flow channel in the new design is T-shaped as opposed to top-hat or L-shaped as in previous designs.

Addressing design features that relate to ease of installation and removal; a few comments are in order. First, the reader may recall that in previous designs the top and bottom conductors were not mechanically connected after the shot. This necessitated their removal as separate pieces which exposed the liner/target region. While it is true that a single-piece removal technique was developed for the previous configuration, that technique proved to be complicated involving post-shot drilling, tapping, and bolting of the upper and lower conductors. The new design includes four insulated post-hole bolts that enable efficient installation and removal of the cassette as a single unit.

A cross-sectional drawing of the new shallow cassette assembly is provided in Fig. 1. Major components include: (1) the return conductor (item 1, colored green, and constructed from aluminum 6061), (2) the liner (item 2, colored red, and constructed from aluminum 1100-0), (3) the liner extension (item 3, colored “the color of brass,” and constructed from soft yellow brass), (4) the insulator (item 4, colored grey, and constructed from polyether ether keytone, generally denoted as PEEK), (5) the upper glide plane (item 5, colored approximately blue (or perhaps turquoise), and constructed from aluminum 7075), (6) the lower glide plane (item 6, colored a somewhat darker blue than the upper glide plane, and constructed from aluminum 7075), (7) the lower glide plane extension (item 7, colored approximately blue (or perhaps turquoise), and constructed from aluminum 7075), (8) a photon doppler velocimetry (PDV) assembly (item 9, colored dark grey, and situated at the center of the overall assembly where a sample canister would normally sit), (10) upper and lower low Z windows (items 10 and 11, colored white), and (11) four durostone threaded rods (the post-hole bolts, item 15, colored brown), two of which are shown in Fig. 1.

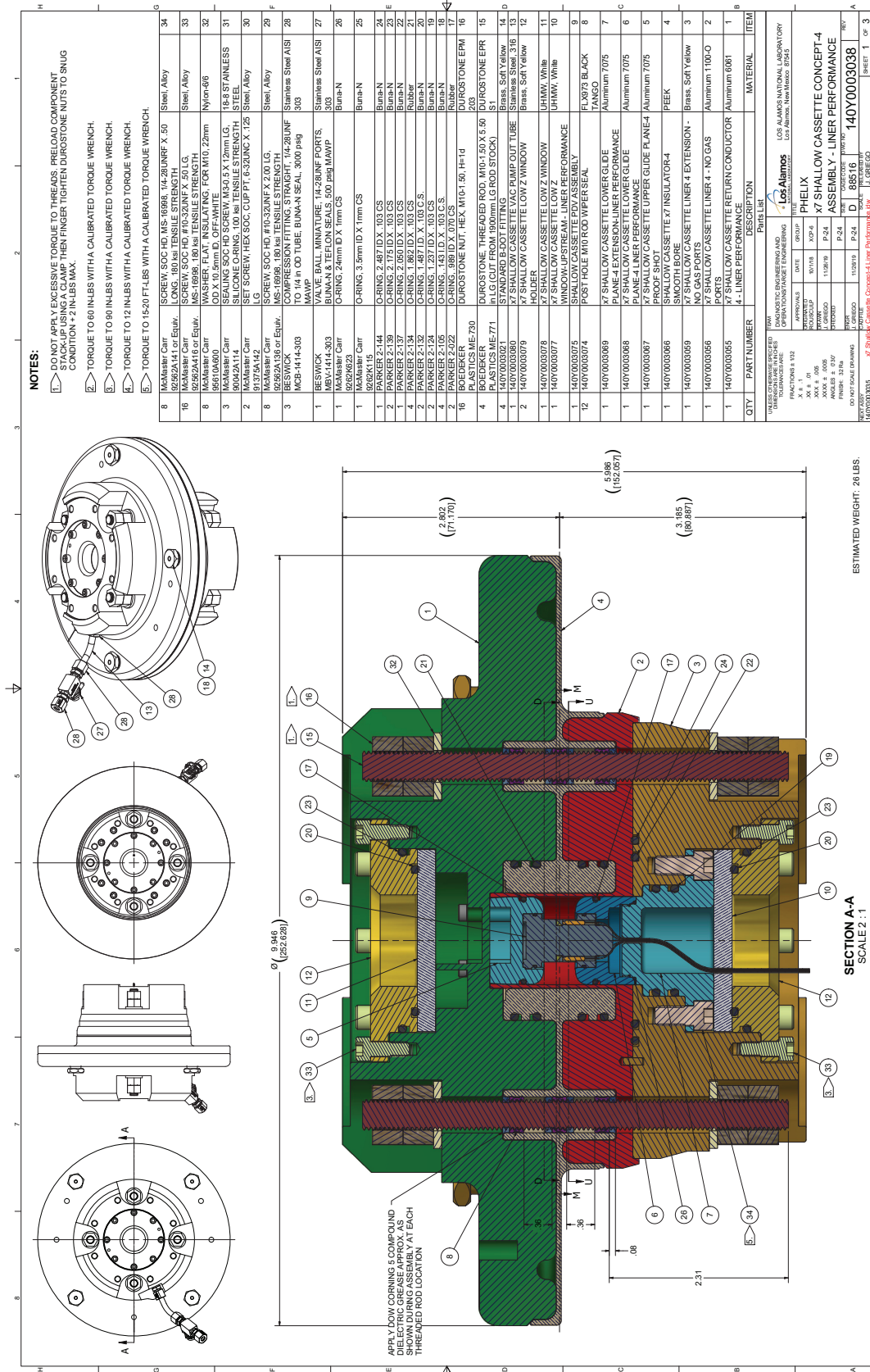


Figure 1: Cutaway of the PHELIX shallow cassette used in liner performance Tests 1 and 2

2 Diagnostics

Diagnostics for the experiments included measurement of velocities and currents. Faraday gauges were used for measurement of current. These involved two channels with two polarizations per channel. Velocities were measured using PDV probes. Twelve PDV probes were used in each of the experiments (Test 1 and Test 2). The PDV probes were configured in each experiment such that there were 6 probes focused on the midplane (M), 3 probes focused downstream (D), and 3 probes focused upstream (U) (see Fig. 2 and Table 1. Note (see Fig. 2) that all twelve probes focus on a different azimuth. This is to enable an assessment of symmetry as the liner converges toward the centerline.

Table 1: Probes identifiers

Probe ID	M, U, or D
1	M
2	M
3	D
4	U
5	M
6	M
7	D
8	U
9	M
10	M
11	D
12	U

3 Experimental Results

3.1 Test 1

The current measured in Test 1 is presented in Fig. 3. The velocities measured in Test 1 by the midplane (M) probes are presented in Fig. 4. The velocities measures in Test 1 by both the upstream (U) and downstream (D) probes are presented in Fig. 5. All velocities measured in Test 1 are presented in Fig. 6.

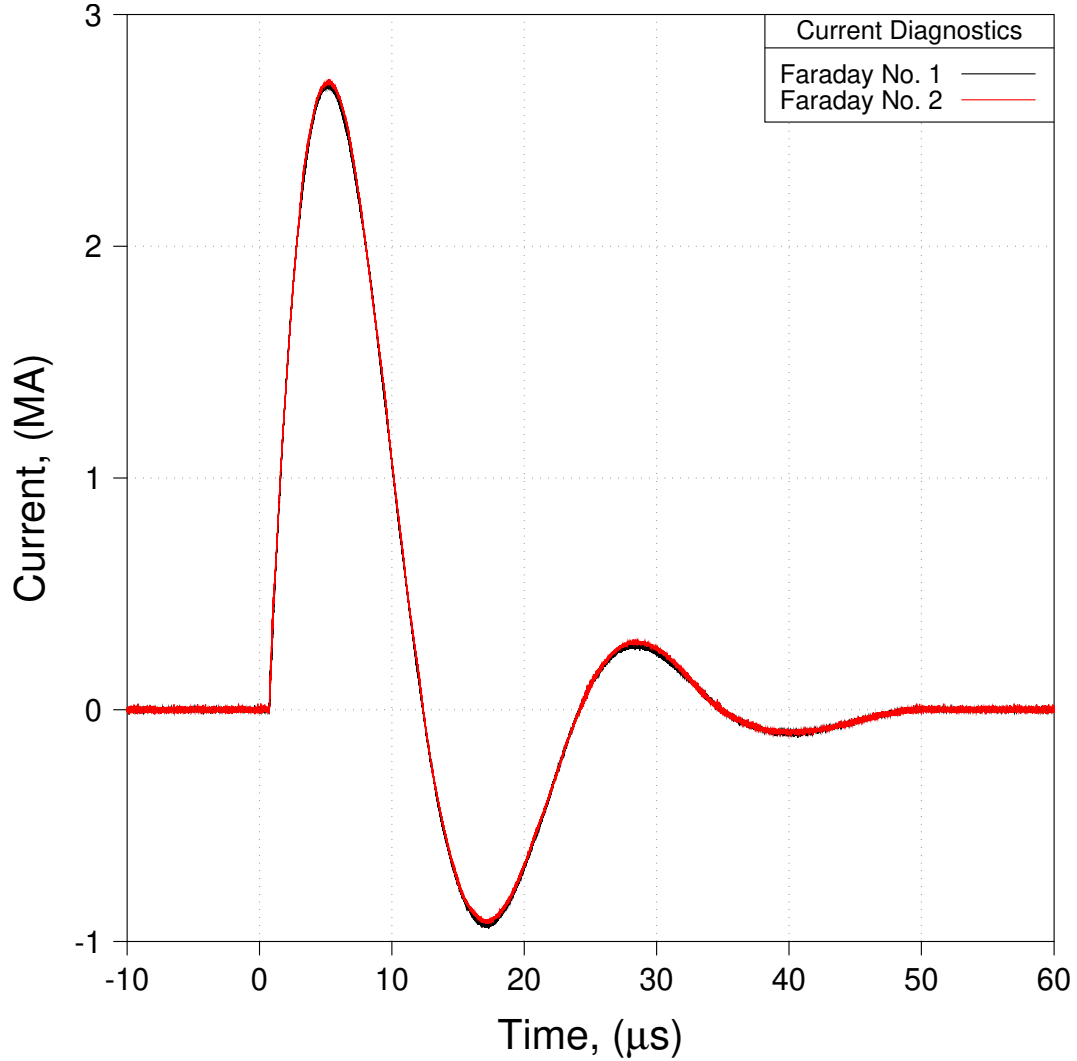


Figure 3: Current measurements – Test 1

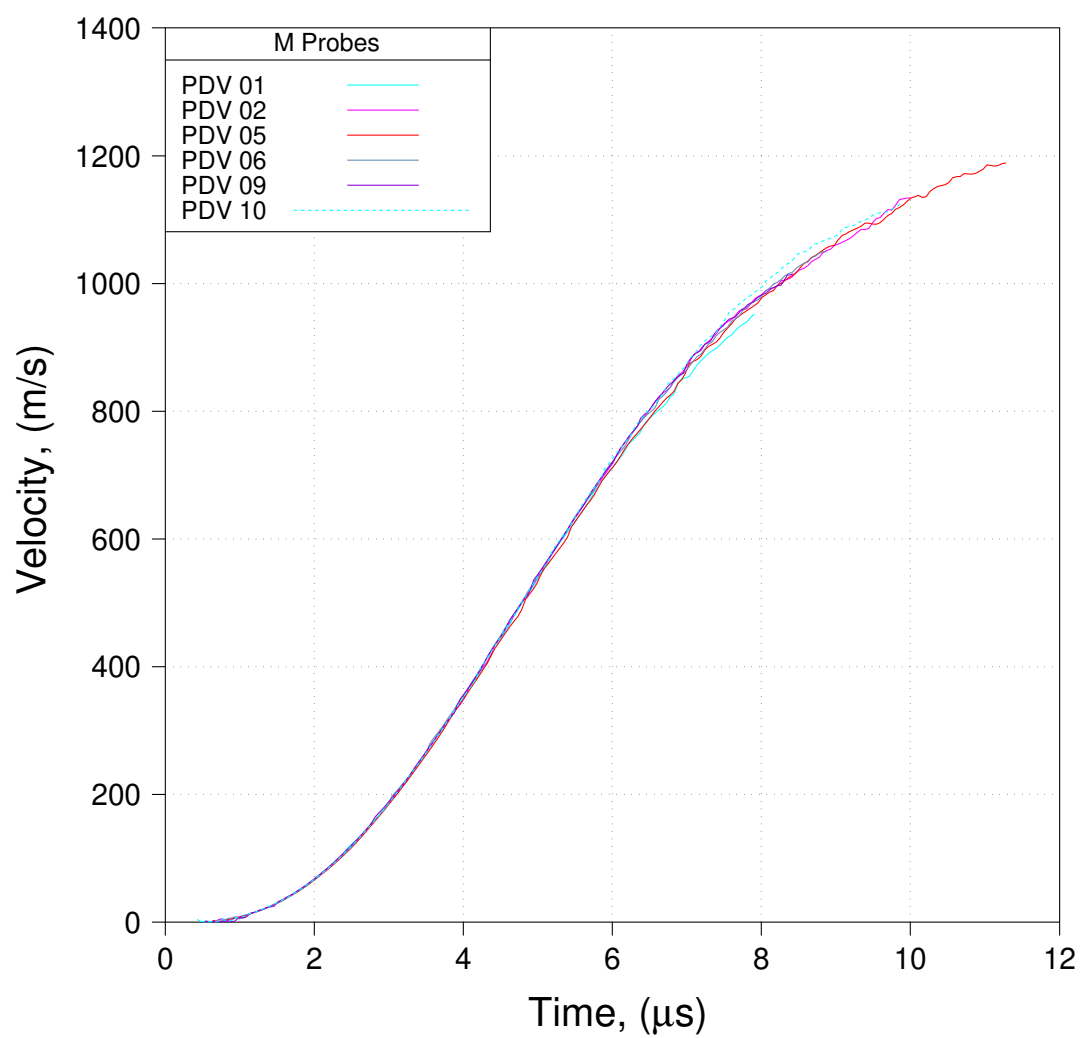


Figure 4: Midplane velocity measurements – Test 1

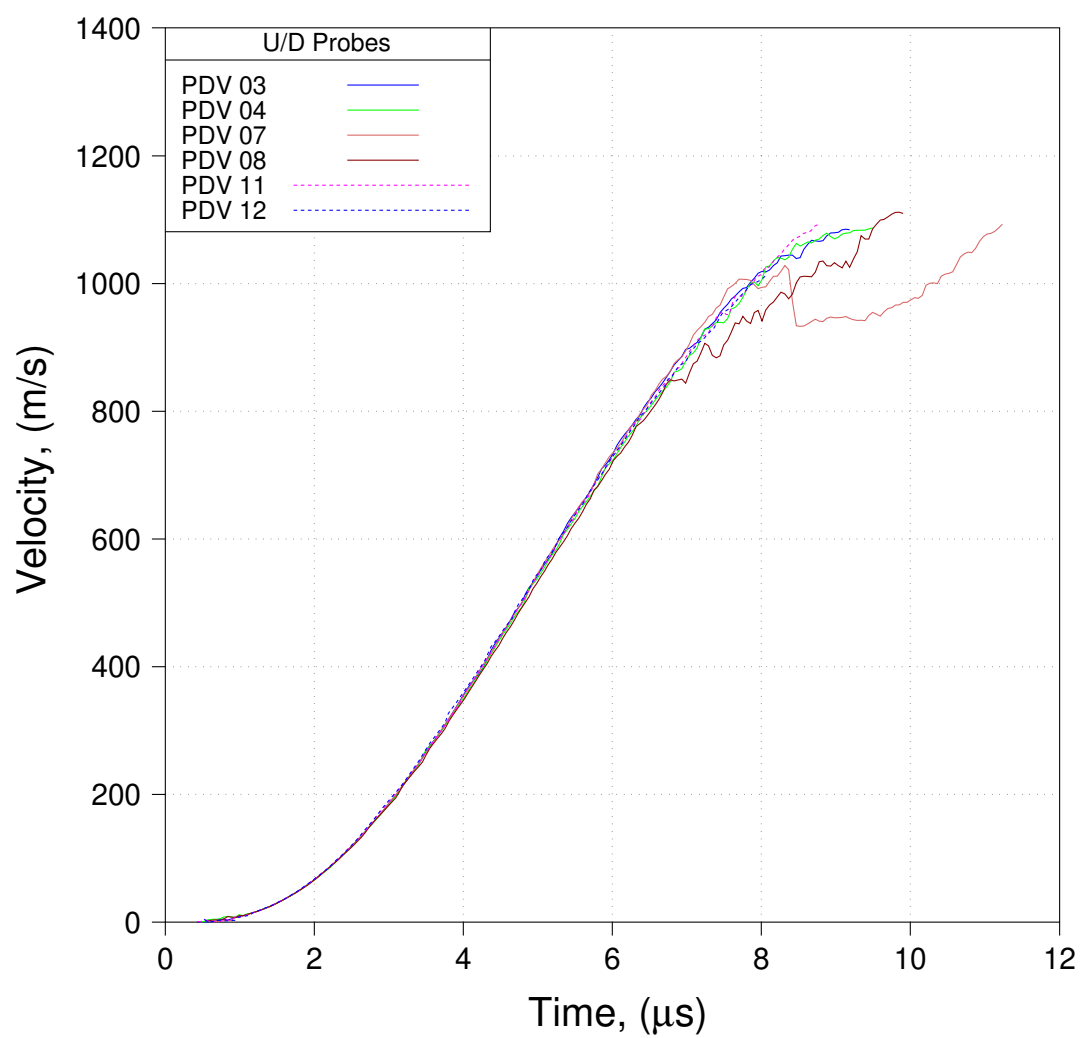


Figure 5: Upstream and downstream velocity measurements – Test 1

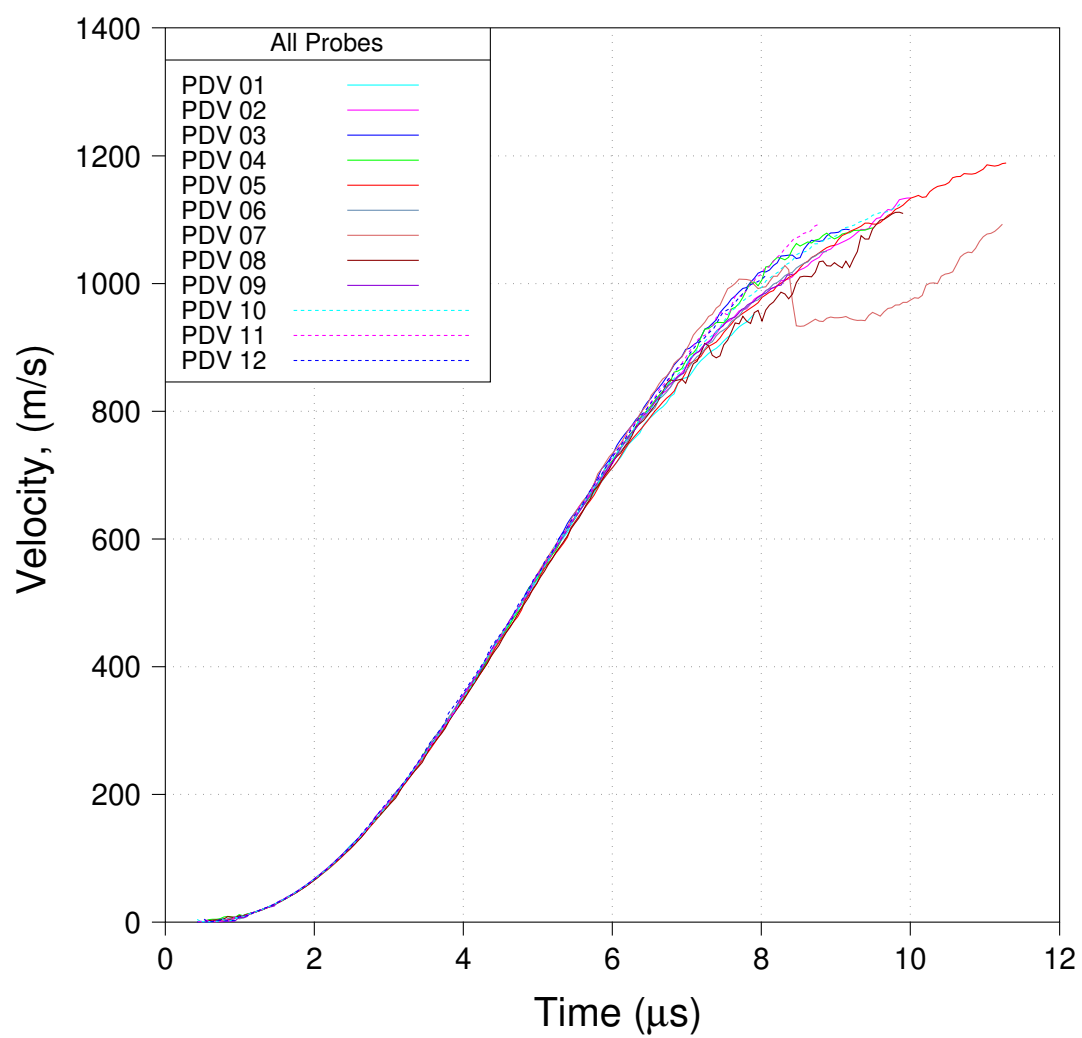


Figure 6: All velocity measurements – Test 1

3.2 Test 2

The current measured in Test 2 is presented in Fig. 7. The velocities measured in Test 2 by the midplane (M) probes are presented in Fig. 8. The velocities measures in Test 2 by both the upstream (U) and downstream (D) probes are presented in Fig. 9. All velocities measured in Test 2 are presented in Fig. 10.

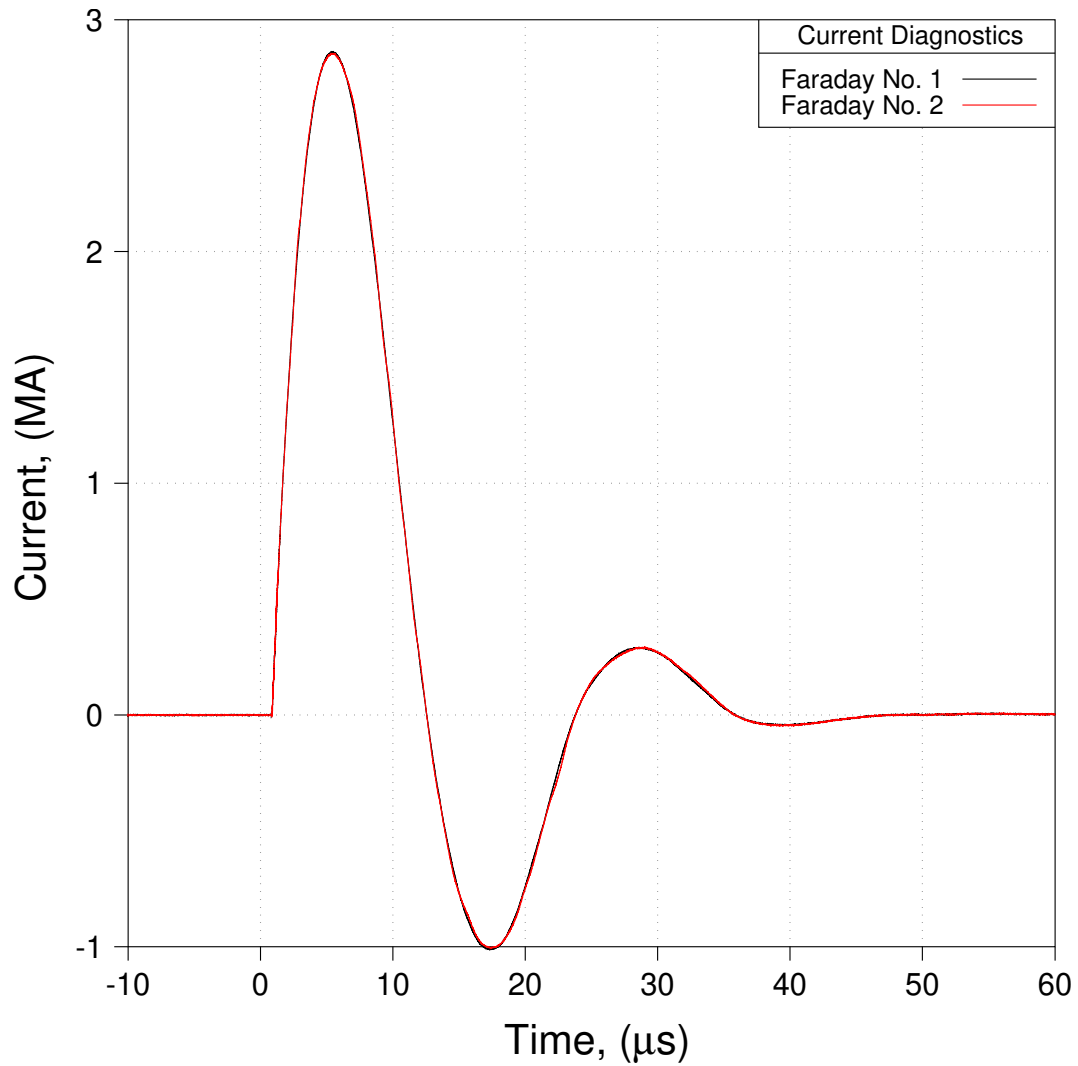


Figure 7: Current measurements – Test 2

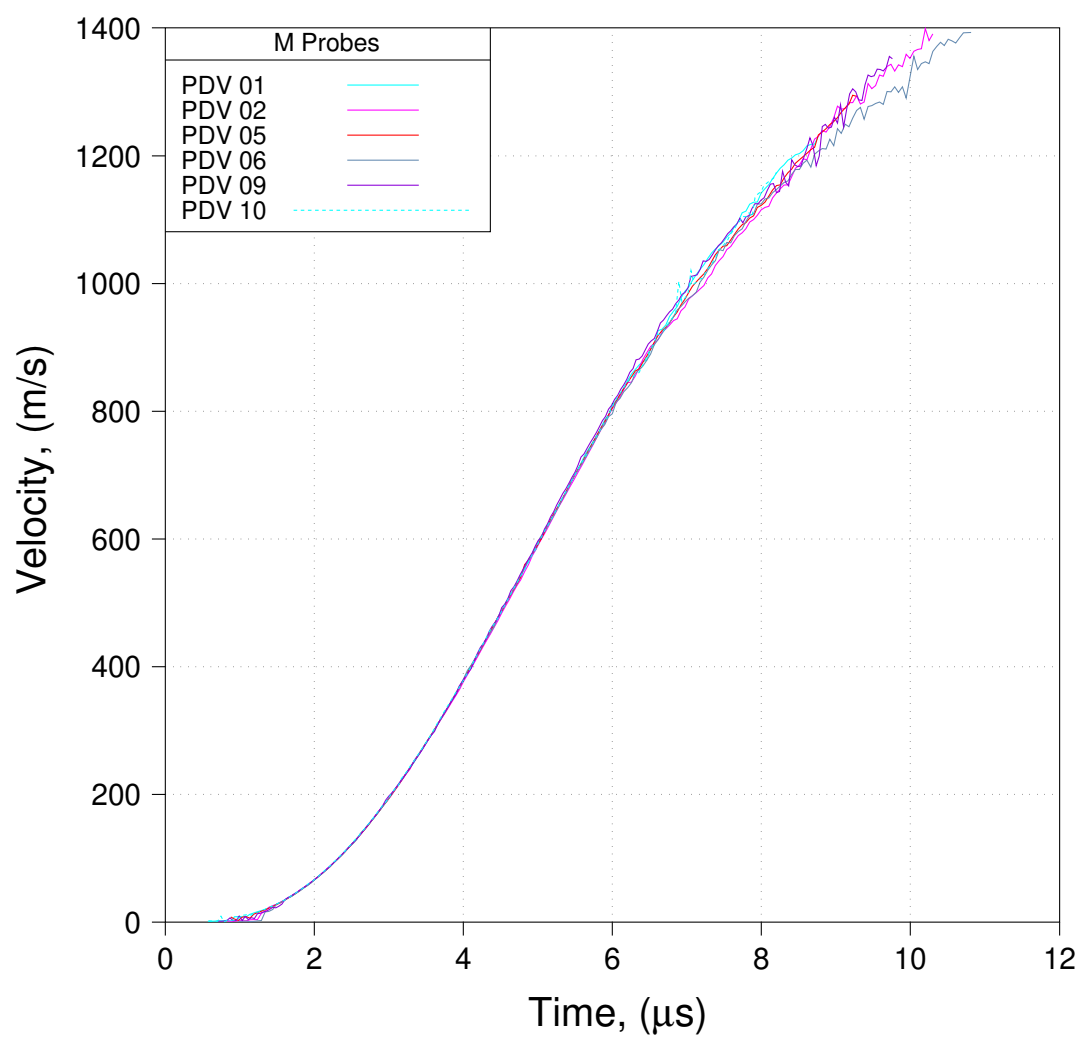


Figure 8: Midplane velocity measurements – Test 2

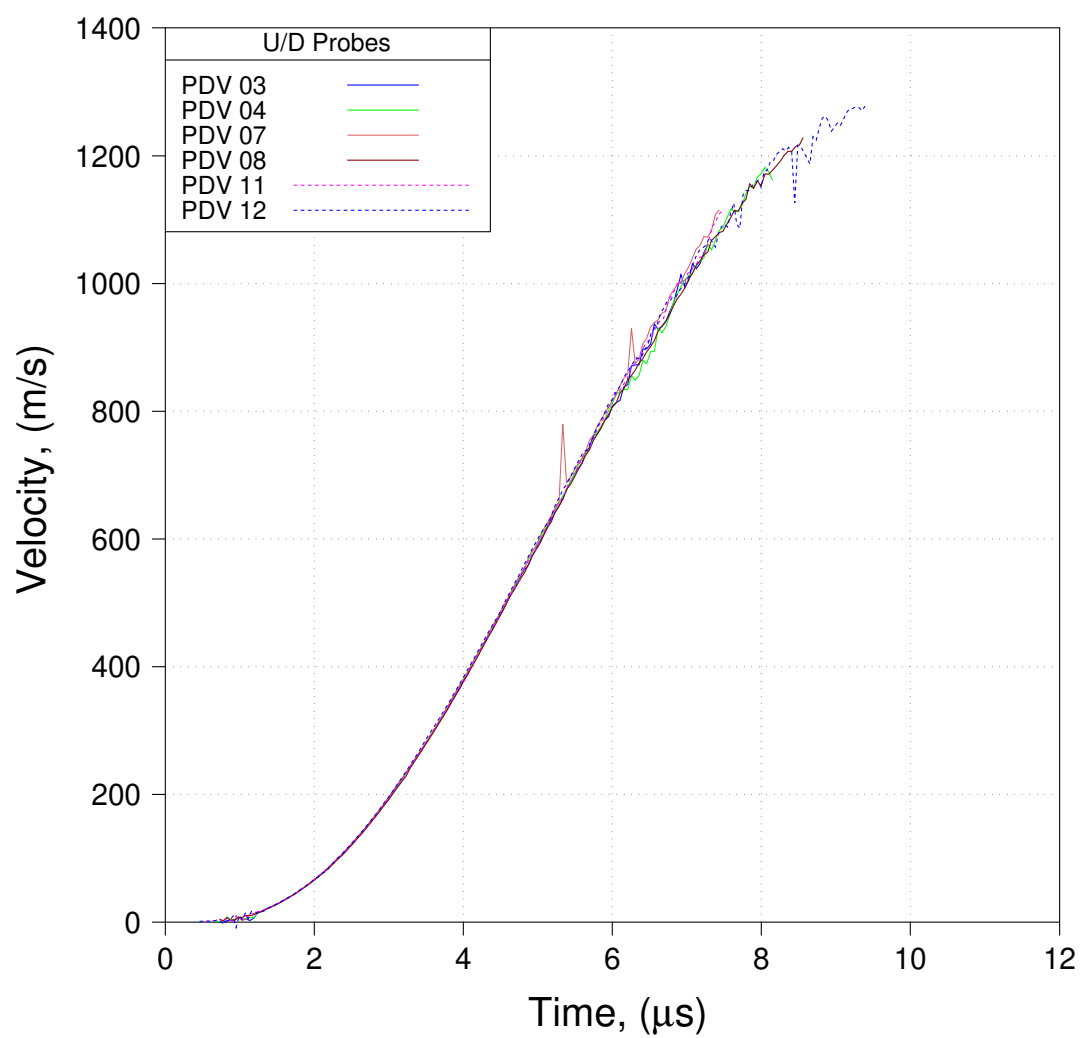


Figure 9: Upstream and downstream velocity measurements – Test 2

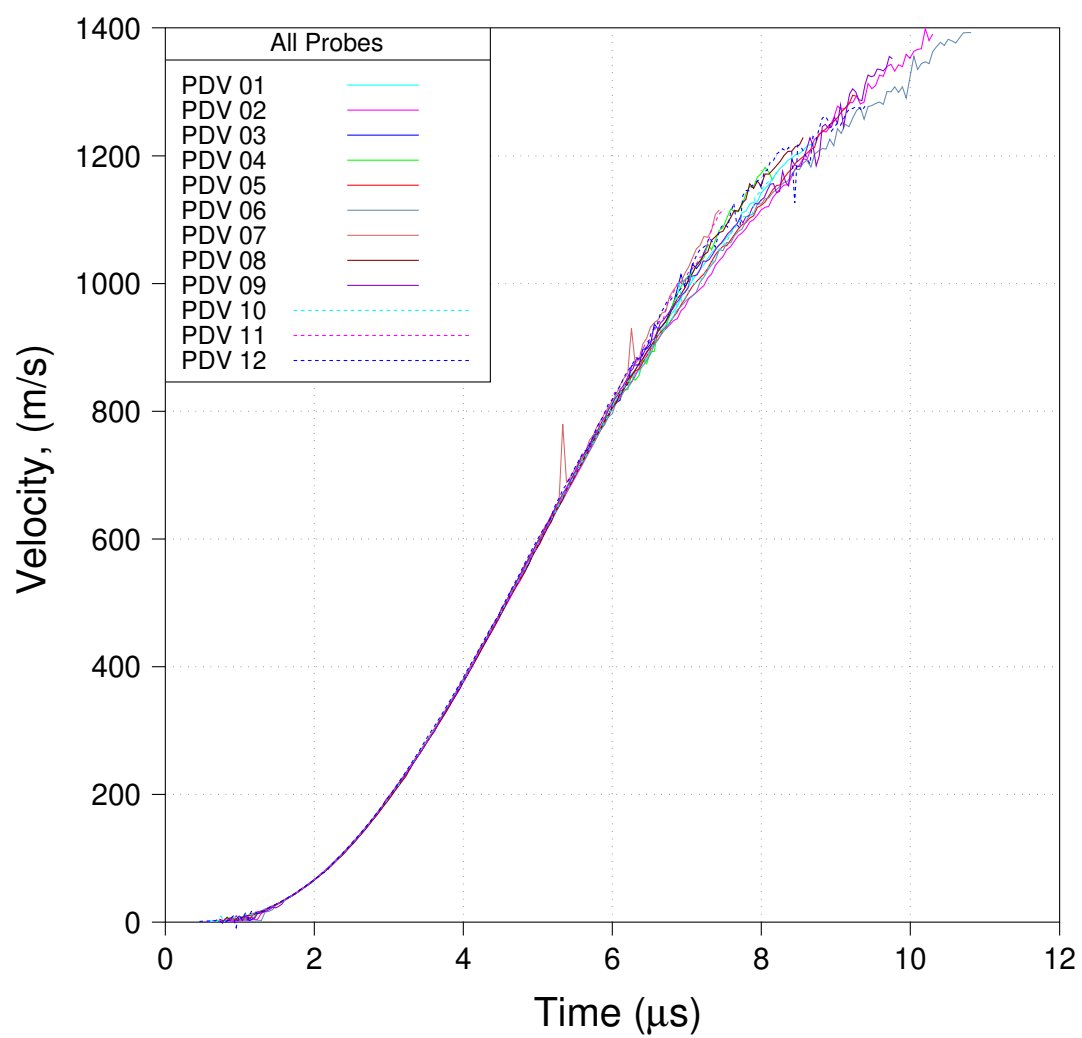


Figure 10: All velocity measurements – Test 2

4 Numerical Model

4.1 Simplifying Assumptions and Approximations

The experiments discussed herein were modeled using the LANL simulation code FLAG [1], in particular, FLAG versions 3.8.Alpha.18 and 3.8.Alpha.21. FLAG is a finite volume continuum mechanics code that incorporates arbitrary Lagrangian-Eulerian (ALE) capabilities. FLAG's ALE capabilities include a number of different nodal relaxation models as well as some limited remap capability. In our analysis we made liberal use of the feasibility set relaxer [2].

In addition to classical continuum mechanics, FLAG has an MHD package that computes resistive diffusion of the magnetic field from the delivered current as well as the Lorentz forces that act on conductors. A simplified lumped circuit element solver couples a model of the PHELIX driver to the finite volume calculations.

In all of our modeling we make the assumption that the experiments can be adequately simulated assuming 2d-axisymmetry. We also make numerous simplifications as to geometry and system complexity. These assumptions were driven, in large part, by an anticipation that liner convergence would be relatively symmetric (thereby validating the 2d-axisymmetry assumption), and that simplifying approximations to many of the engineering details could be made without profoundly affecting simulation accuracy, at least with respect to the primary diagnostics. By in large, as will be demonstrated, these assumptions were found to be justified.

Figure 11 provides the reader with a sketch of the PHELIX components that were included in our numerical model, which serves to illustrate many of our simplifications. Note that there are only nine components in this model: return conductor, insulator, liner, glide plane, driver, end cap, upper air, lower air, and vacuum. Note that the light blue lines in Fig. 11 denote lines of symmetry. Since the numerical analysis is conducted assuming 2d-axisymmetry, the assembly shown in Fig. 11 should be thought of as being first reflected about the horizontal line of symmetry and then spun about the vertical line of symmetry. Our 2d-axisymmetric meshes were created using the LANL mesh generator InGen. Our meshes involved quadrilateral elements only, which were approximately, on average, $100\ \mu\text{m}$ on a side. Our meshes all had 10 elements numbered in the liner through-thickness direction. Note that the components labeled end cap and driver in Fig. 11 are artificial, they did not exist in the actual experiments. Had there been a sample canister at the center of the assembly, then these components would have existed as components of that canister. However, in the experiments modeled here, the PDV probe assembly sat where the sample canister would normally sit (see Figs. 1 and 2), hence what is labeled here as end cap and driver was, in reality, portions of the PDV probe assembly. The end cap and driver exist in our meshes simply for the purpose of having a smooth surface for the liner to follow as it slides past the glide plane.

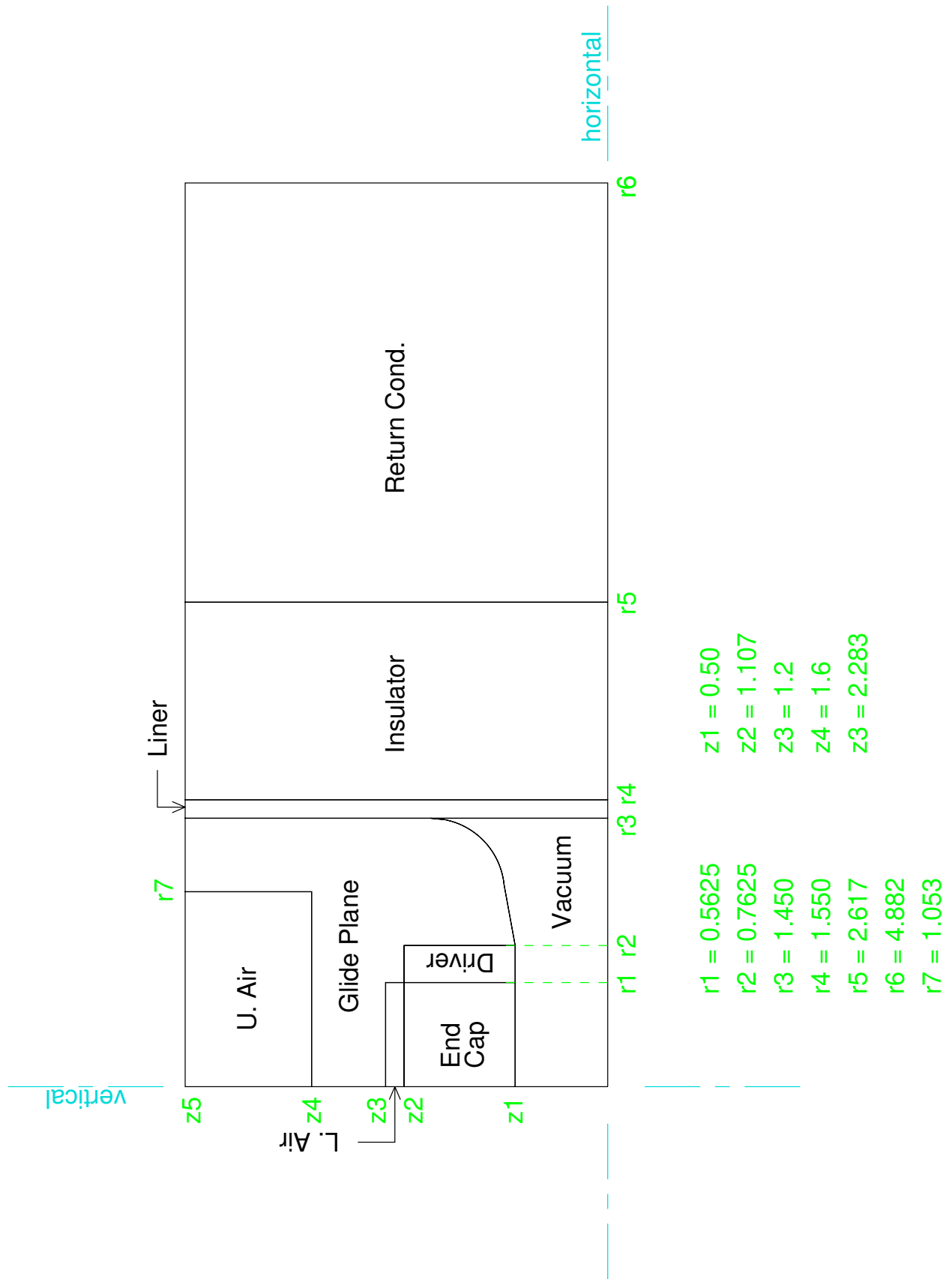


Figure 11: Sketch of components included in 2d-axisymmetric mesh (all dimensions in cm)

4.2 Material Models

4.2.1 Aluminum 6061-T6 components (driver end cap, and return conductor)

Several of the components in our assembly were modeled as constructed from aluminum 6061-T6. These include the driver, return conductor, and end cap. The constitutive behavior of the 6061-T6 aluminum was modeled in two parts – hydrostat and deviator. The hydrostat was determined using a SESAME tabular equation of state (EOS). The EOS that we employed for 6061-T6 is 3720. We chose to model the flow stress (which provides the deviator with any hardening/softening response that may occur during plastic flow) using the model of Steinberg, Cochran, and Guinan (SCG) [3]. The SCG model is a simple history independent model that is dependent upon the current values of plastic strain, pressure, and temperature, thus $\sigma = \sigma(\epsilon, p, T)$. The SCG model in FLAG is slightly modified from that given in [3] and is given as:

$$G = G_0 \left\{ 1 + A \frac{p}{\eta^{1/3}} - B(T - T_r) \right\} \exp \left\{ -f_g \left(\frac{T}{T_m(\eta) - T} \right) \right\} \quad (1)$$

$$Y = \min \left[Y_0 \{1 + \beta (\epsilon^p + \epsilon_i)\}^n, Y_{\max} \right] \left\{ 1 + q_y A \frac{p}{\eta^{1/3}} - B(T - T_r) \right\} \exp \left\{ -f_y \left(\frac{T}{T_m(\eta) - T} \right) \right\} \quad (2)$$

where G_0 is the shear modulus at the reference state ($T_r = 300$ K, $p = 0$, $\epsilon^p = 0$), η is the compression (ρ/ρ_0), Y_0 is the reference state uniaxial yield strength, ϵ_i is the initial equivalent plastic strain, n and β are work hardening parameters, Y_{\max} is the maximum value of uniaxial yield (at $T = 300$ K and $p = 0$) that can be found in the literature. This model requires twelve input parameters: ρ_0 , G_0 , Y_0 , β , n , Y_{\max} , A , B , q_y , f_y , f_g , and ϵ_i . The values of the SCG model parameters used in this analysis for 6061-T6 are given in Table 2.

Table 2: SCG parameter set for 6061-T6

Model Parameter	Designated Value
ρ_0	2.703 g/cm ³
G_0	0.276 Mbar
Y_0	2.9E-03 Mbar
β	125.0
n	0.1
Y_{\max}	6.8E-03 Mbar
A	6.52 Mbar ⁻¹
B	6.16E-04 K ⁻¹
q_y	1.0
f_y	0.0
f_g	0.0
ϵ_i	0.0

Note that the SCG model as presented in [3] incorporates the Lindemann [4] model for melt. In our analysis we have chosen to use a SESAME table for melt as opposed to the Lindemann model. For 6061-T6 we use table 33717. For artificial viscosity we employed the model of Barton [5]. This model

has four input parameters: q_1 , q_2 , q_{1n} , and q_{2n} . The values used in this analysis for 6061-T6 are given in Table 3

Table 3: Barton artificial viscosity parameter set for 6061-T6

Model Parameter	Designated Value
q_1	0.15
q_2	1.35
q_{1n}	0.15
q_{2n}	0.0

4.2.2 Aluminum 7075 component (the glide plane)

The glide plane was constructed from aluminum 7075. For this material we used SESAME for both the constitutive hydrostat (3719) and for melt (33717). As with the 6061-T6 components we chose to use the SCG model to calculate the flow stress. SCG parameters used for this material are given in Table 4. For 7075 we employed the Barton model for artificial viscosity using the same parameter set as was given in Table 3.

Table 4: SCG parameter set for aluminum 7075

Model Parameter	Designated Value
ρ_0	2.703 g/cm ³
G_0	0.267 Mbar
Y_0	4.2E-03 Mbar
β	965.0
n	0.1
Y_{\max}	8.1E-03 Mbar
A	6.52 Mbar ⁻¹
B	6.16E-04 K ⁻¹
q_y	1.0
f_y	1.0
f_g	0.0
ϵ_i	0.0

4.2.3 Aluminum 1100 component (the liner)

The liner was constructed from aluminum 1100-0. For this material we used SESAME for the constitutive hydrostat (3720), the shear modulus (33710), and for melt (33720). Instead of the SCG model for calculating the flow stress we chose to use the model of Preston, Tonks, and Wallace (PTW) [6]. Note that the PTW model as described in [6] includes an analytical model for the shear stress and a constant melt temperature, which input as a parameter. Since we chose to use SESAME for melt temperature and for shear stress, those aspects of the model presented in [6] are not pertinent here. The aspects of the PTW model that are pertinent are outlined in the following paragraph [7].

Let the variable $\dot{\xi}$ be defined as follows:

$$\dot{\xi} = \frac{1}{2} \left(\frac{4\pi\rho}{3M} \right)^{1/3} \sqrt{\frac{G}{\rho}} \quad (3)$$

where $\dot{\xi}$ is the reciprocal of the time required for a shear wave to traverse an atom (units are s^{-1}), ρ is the density, and M is the atomic mass (mass of a single atom).

Let a dimensionless saturation stress, $\hat{\tau}_s$, be defined as follows:

$$\hat{\tau}_s = \max \left\{ s_0 - (s_0 - s_\infty) \operatorname{erf} \left[\kappa \hat{T} \ln \left(\frac{\gamma \dot{\xi}}{\dot{\epsilon}} \right) \right], s_0 \left(\frac{\dot{\epsilon}}{\gamma \dot{\xi}} \right)^\beta \right\} \quad (4)$$

where $\hat{\tau}_s$ is a dimensionless saturation stress, and s_0 , s_∞ , κ , γ , and β are dimensionless parameters.

Let a dimensionless dynamic yield stress, $\hat{\tau}_y$, be defined as follows:

$$\hat{\tau}_y = \max \left\{ y_0 - (y_0 - y_\infty) \operatorname{erf} \left[\kappa \hat{T} \ln \left(\frac{\gamma \dot{\xi}}{\dot{\epsilon}} \right) \right], \min \left[y_1 \left(\frac{\dot{\epsilon}}{\gamma \dot{\xi}} \right)^{y_2} s_0 \left(\frac{\dot{\epsilon}}{\gamma \dot{\xi}} \right)^\beta \right] \right\} \quad (5)$$

where $\hat{\tau}_y$ is a dimensionless dynamic yield stress, and y_0 , and y_∞ are dimensionless parameters.

Finally a dimensionless flow stress $\hat{\tau}$, is given as:

$$\hat{\tau} = \begin{cases} \hat{\tau}_s & \text{if } a \\ \hat{\tau}_s - (\hat{\tau}_s - \hat{\tau}_y) \exp \left(-\frac{1}{k} \epsilon \right) & \text{if } b \\ \hat{\tau}_s + \frac{1}{p} (s_0 - \hat{\tau}_y) \ln \left[1 - \left[1 - \exp \left(-p \frac{\hat{\tau}_s - \hat{\tau}_y}{s_0 - \hat{\tau}_y} \right) \right] \exp \left\{ -\frac{p\theta\epsilon}{(s_0 - \hat{\tau}_y) \left[\exp \left(p \frac{\hat{\tau}_s - \hat{\tau}_y}{s_0 - \hat{\tau}_y} \right) - 1 \right]} \right\} \right] & \text{if } c \end{cases} \quad (6)$$

where,

- a: if $\hat{\tau}_s = \hat{\tau}_y$;
- b: if $p = 0$ (Voce equation applies);
- c: otherwise;
- $k = (\hat{\tau}_s - \hat{\tau}_y) / \theta$ (θ and p are dimensionless parameters).

The flow stress is now given as:

$$\sigma = 2 \hat{\tau} G \quad (7)$$

As presented here the PTW model requires 12 input parameters: p , θ , κ , γ , M , s_0 , s_∞ , y_0 , y_1 , y_2 , y_∞ , and β . The parameter set used in this work is given in Table 5.

Table 5: PTW parameter set for aluminum 1100

Model Parameter	Designated Value
p	3.0
θ	0.0184
κ	0.2
γ	5.0E-05
M	4.496E-23
s_0	0.0142
s_∞	0.00856
y_0	0.00898
y_1	0.0142
y_2	0.4
y_{infty}	0.00596
β	0.23

For aluminum 1100 we employed the Barton model for artificial viscosity using the same parameter set as was given in Table 3. We initialized with density $\rho = 2.7 \text{ g/cm}^3$, and with energy $e = 0.0 \text{ Mbar-cm}^3 / \text{g}$.

4.2.4 Insulator

The insulator was modeled as a fluid (*i.e.*, no deviator). For the hydrostat we used an analytical γ -law EOS:

$$e = C_v(T) (T - T_0) \quad (8)$$

$$p = (\gamma - 1) \rho e - \gamma p^* \quad (9)$$

The γ -law EOS given above requires 5 input parameters: C_v , γ , ρ , p^* , and T_0 . The parameter set used in this work is given in Table 6.

Table 6: γ -law EOS parameter set for the insulator

Model Parameter	Designated Value
C_v	1.E06
γ	2.333333
ρ	2.0 g/cm ³
p^*	0.0
T_0	273.0

For the insulator we employed the Barton model for artificial viscosity using the same parameter set as was given in Table 3. We initialized with density $\rho = 2.0 \text{ g/cm}^3$, and with energy $e = 0.0 \text{ Mbar-cm}^3 / \text{g}$.

4.2.5 Air and Vacuum

Lower air, upper air, and vacuum were all modeled the same, as low density γ -law gases (the same γ -law as that given in Eqs. 8 and 9). The γ -law parameter set was the same for each of these components and is given in Table 7. We initialized with density $\rho = 1.0\text{E-}06 \text{ g/cm}^3$, and with energy $e = 0.0 \text{ Mbar-cm}^3 / \text{g}$.

Table 7: γ -law EOS parameter set for lower air, upper air, and vacuum

Model Parameter	Designated Value
C_v	1.E06
γ	1.66667
ρ	1.0E-06 g/cm ³
p^*	0.0
T_0	273.0

4.3 MHD Circuit

FLAG incorporates a single-loop resistor-inductor-capacitor (LRC) circuit model with coupling to an MHD mesh via a time varying material-dependent inductance. The model provides the user with two options: option 1, which involves constant coefficients, and option 2, which allows for time varying inductance. In the analysis conducted here constant coefficients were employed. The model requires, in this case, 4 input parameters: an initial inductance, cl0, an initial resistance, cr0, an initial capacitance, cc0, and the value of the driving potential, cv0. The Value given to these four parameters is provided to the reader in Table 8.

Table 8: RLC circuit parameter set

Model Parameter	Designated Value	Corrsponds To
cr0	0.0191	1.91 m Ω
cl0	0.0924	9.24 nH
cc0	103.322	1033.22 μ F
cv0	0.1474	70 kV

5 Numerical Analysis

The discussion of our numerical analysis will be presented in two phases: (1) baseline modeling that was conducted pre-shot, and (2) refined modeling that was conducted post-shot. We discuss herein both pre-shot and post-shot analysis because it is believed that there is benefit to the reader in observing, at least to some degree, the refinement that took place in order to go from: (a) predictions that are perhaps reasonable but not sufficiently accurate, to, (b) predictions that are considerably more accurate. We shall discuss the analysis of Test 1 first followed by a discussion of the analysis of Test 2.

5.1 Test 1 Pre-Shot Analysis

Our pre-shot simulation of Test 1 was conducted using FLAG version 3.8.Alpha.18. Recall that in Test 1 the driving potential was set at 70 kV. The experiment was modeled assuming 2d-axisymmetry. The mesh for this analysis is depicted in Fig. 12. Note the one-to-one correspondence between Figs. 11 and 12. Figures 13 - 24 depict the evolution of the assembly from 0 to 11 μ s. Note that the results depicted in Figs. 12 - 24 are labeled R002. The R002 label is merely a “bookkeeping” identifier used by the authors to keep track of the many simulations conducted in the course of this study (more than one hundred simulations were conducted and the results with identifier R002 were obtained from simulation (or run) number 2, i.e., R002). Note also that in Figs 13 - 24 the results are reflected about both lines of symmetry so that what is depicted in these figures is a cross-section of the simulated cylindrical assembly, not merely a quarter-quadrant of that assembly. Figures 25 and 26 illustrate with the red lines the location of midplane, upstream, and downstream PDV lines of sight. However, keep in mind that since we modeled only one quarter of the assembly, and since our simulations were conducted assuming 2d-axisymmetry, in our analysis there is no difference between upstream and downstream, and differences in azimuth are not accounted for.

In Fig. 27 predicted midplane velocity is compared to empirical data. In Fig. 28 predicted upstream/downstream velocities are compared to empirical data. Some observations on Figs. 27 and 28 are in order. We observe (in Fig. 27) that our pre-shot prediction of midplane velocity is somewhat reasonable, peak velocity is overpredicted by an appreciable amount (on the order of 19%). In Fig. 28 we observe that our pre-shot prediction of upstream/downstream peak velocities is not so far off (compared to our prediction of midplane velocity), but there are other troubling features depicted in Fig. 28. First of all, we predict that at the upstream/downstream locations the liner starts off moving in the wrong direction (negative velocity), which is unrealistic. Second, we predict an appreciable drop in velocity starting at about 9 μ s that does not appear to be measured (though it appears that PDV 07 might hint at something of a drop off in velocity). Note that impact time depicted in Figs. 27 and 28 represents an estimation of the time of impact between liner and sample canister if a sample canister were present.

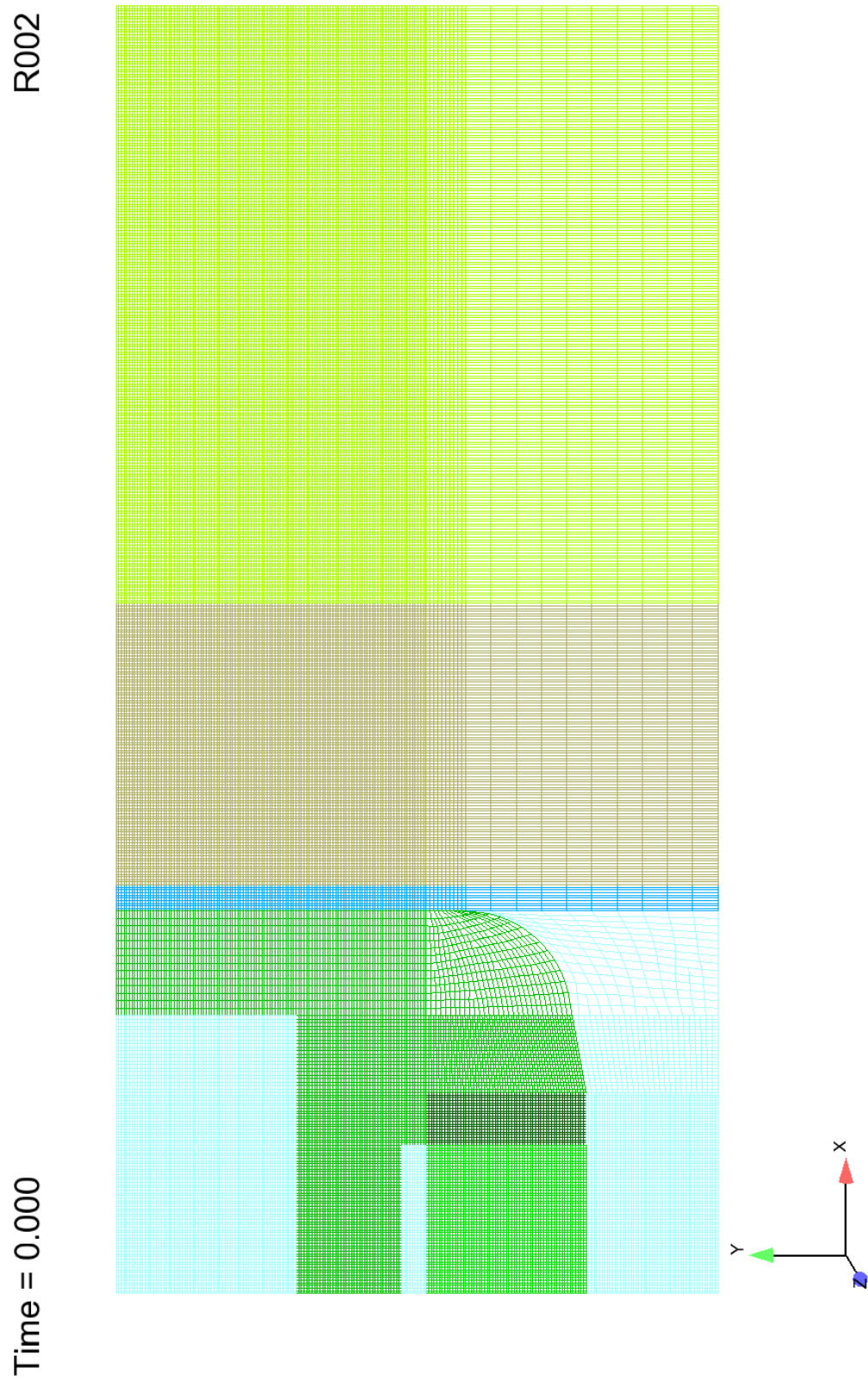


Figure 12: Mesh used for R002

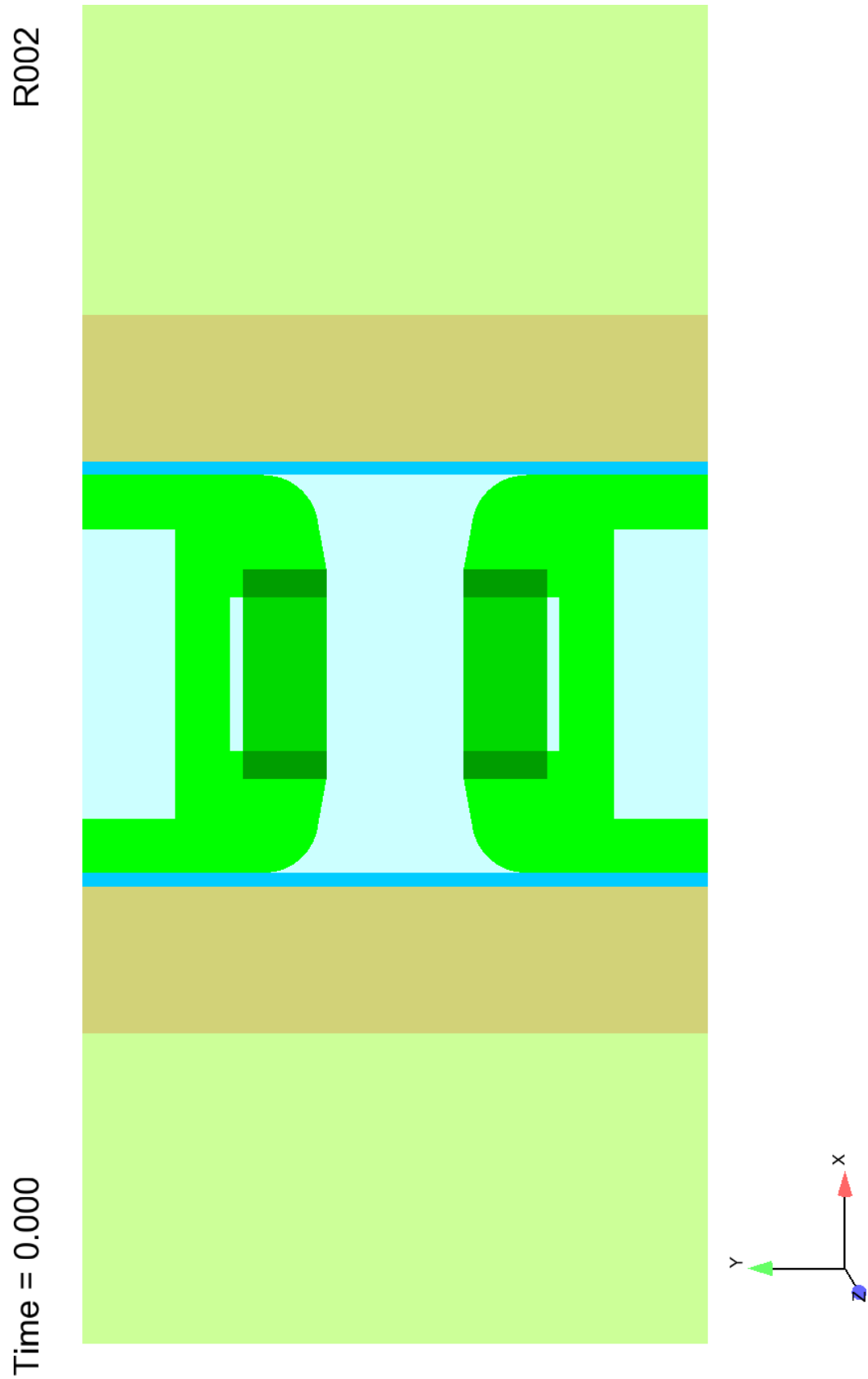


Figure 13: Test 1 configuration $t = 0 \mu s$

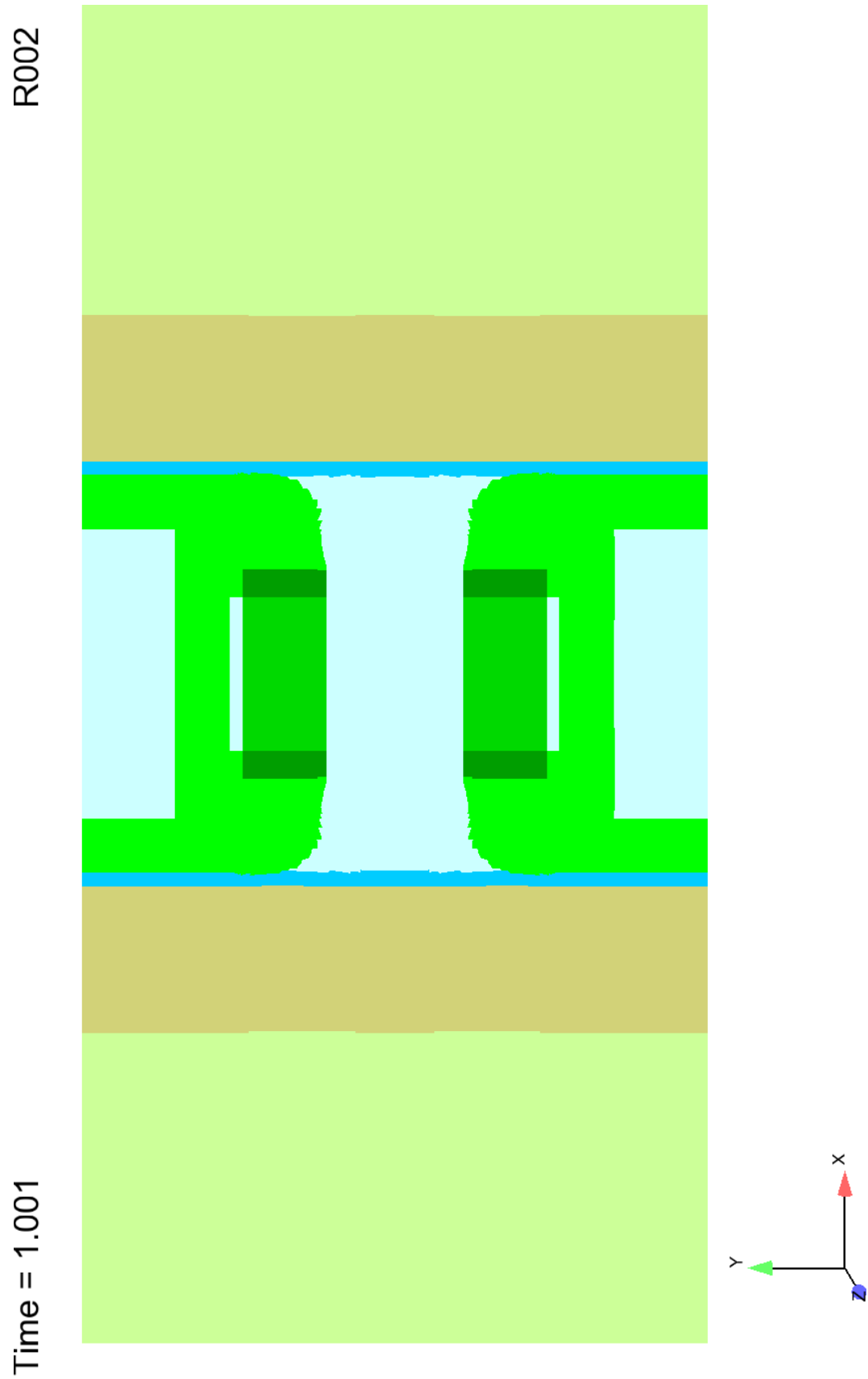


Figure 14: Predicted Test 1 configuration $t = 1 \mu s$

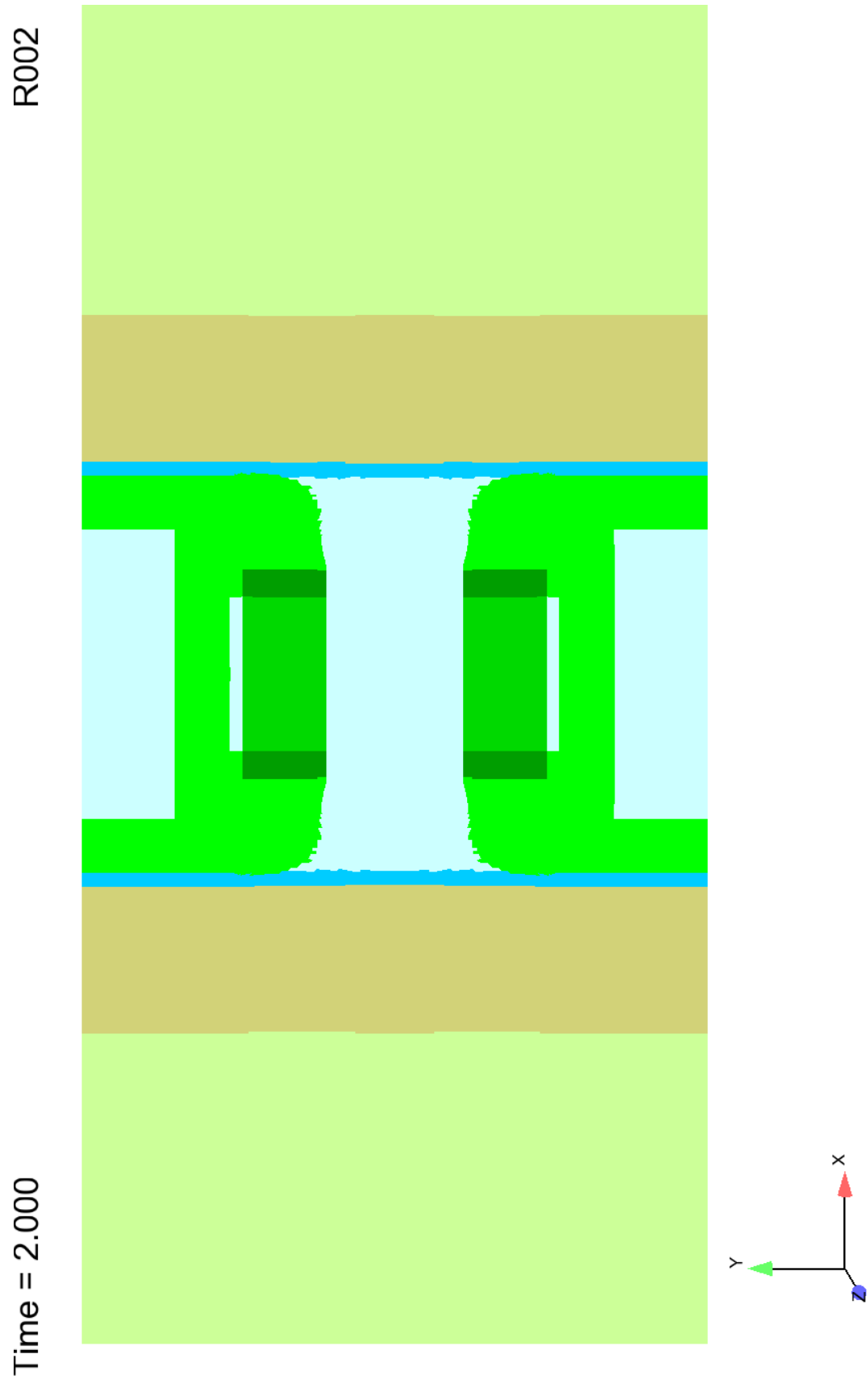


Figure 15: Predicted Test 1 configuration $t = 2 \mu s$

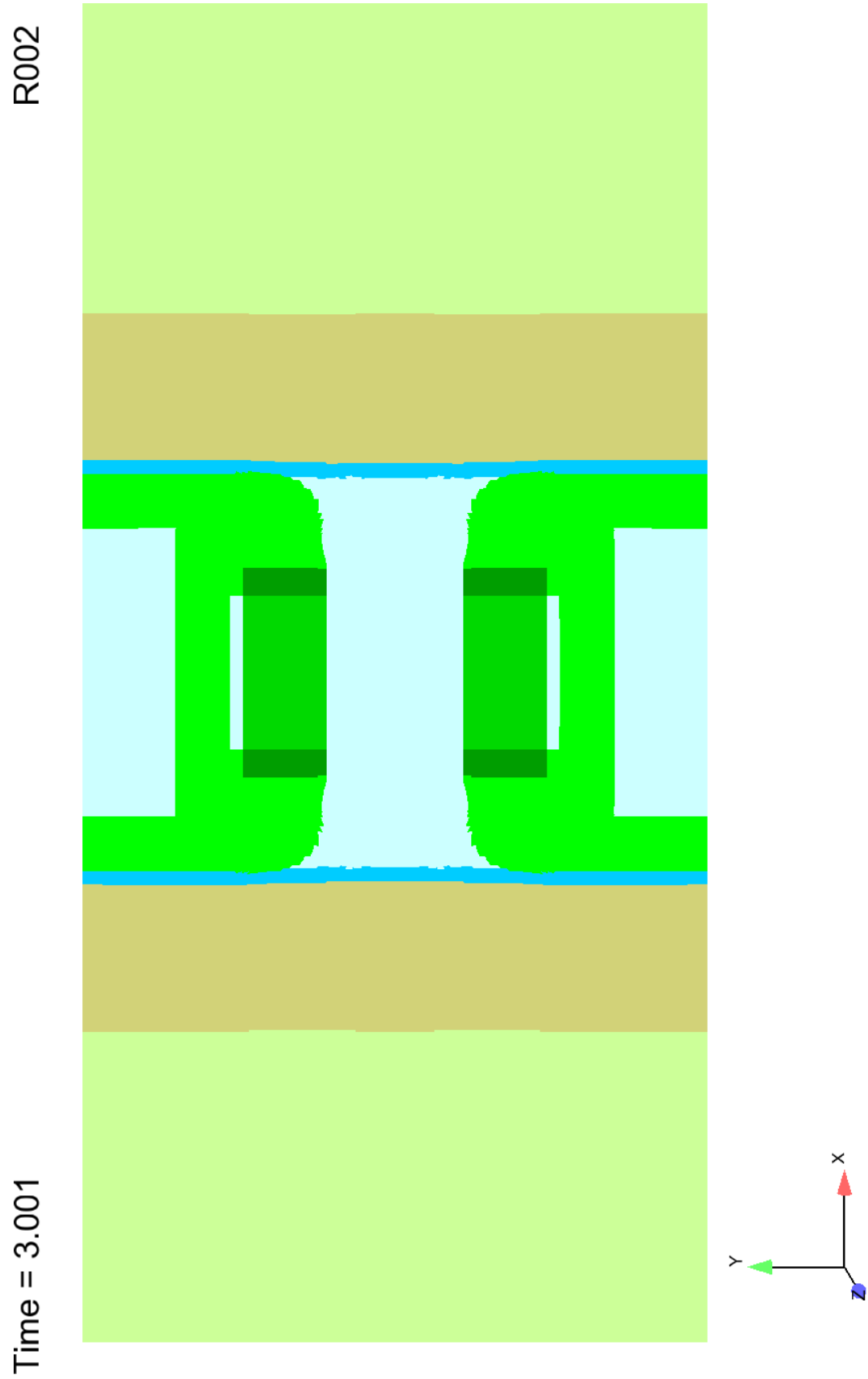


Figure 16: Predicted Test 1 configuration $t = 3 \mu s$

R002

Time = 4.000

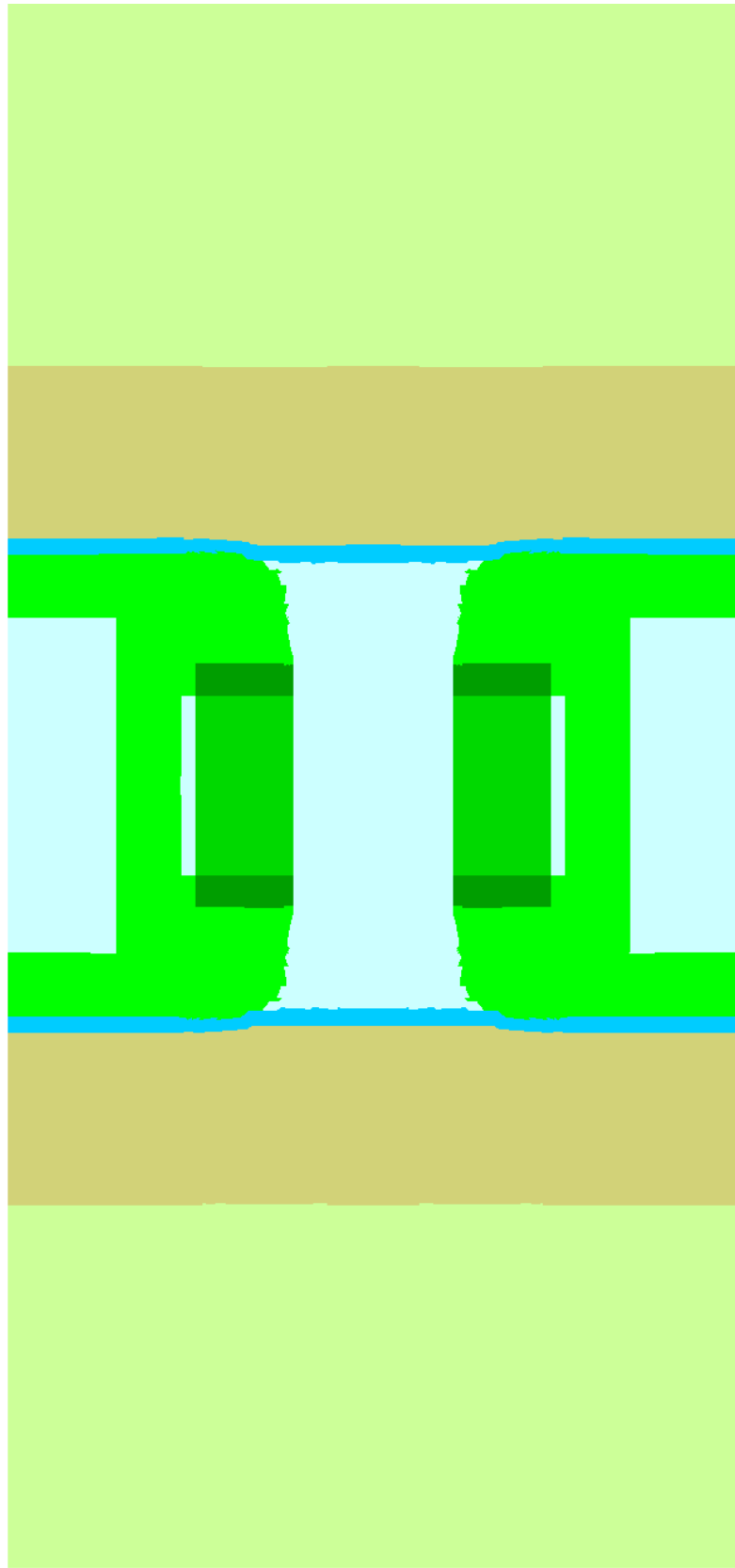


Figure 17: Predicted Test 1 configuration $t = 4 \mu s$

R002

Time = 5.002

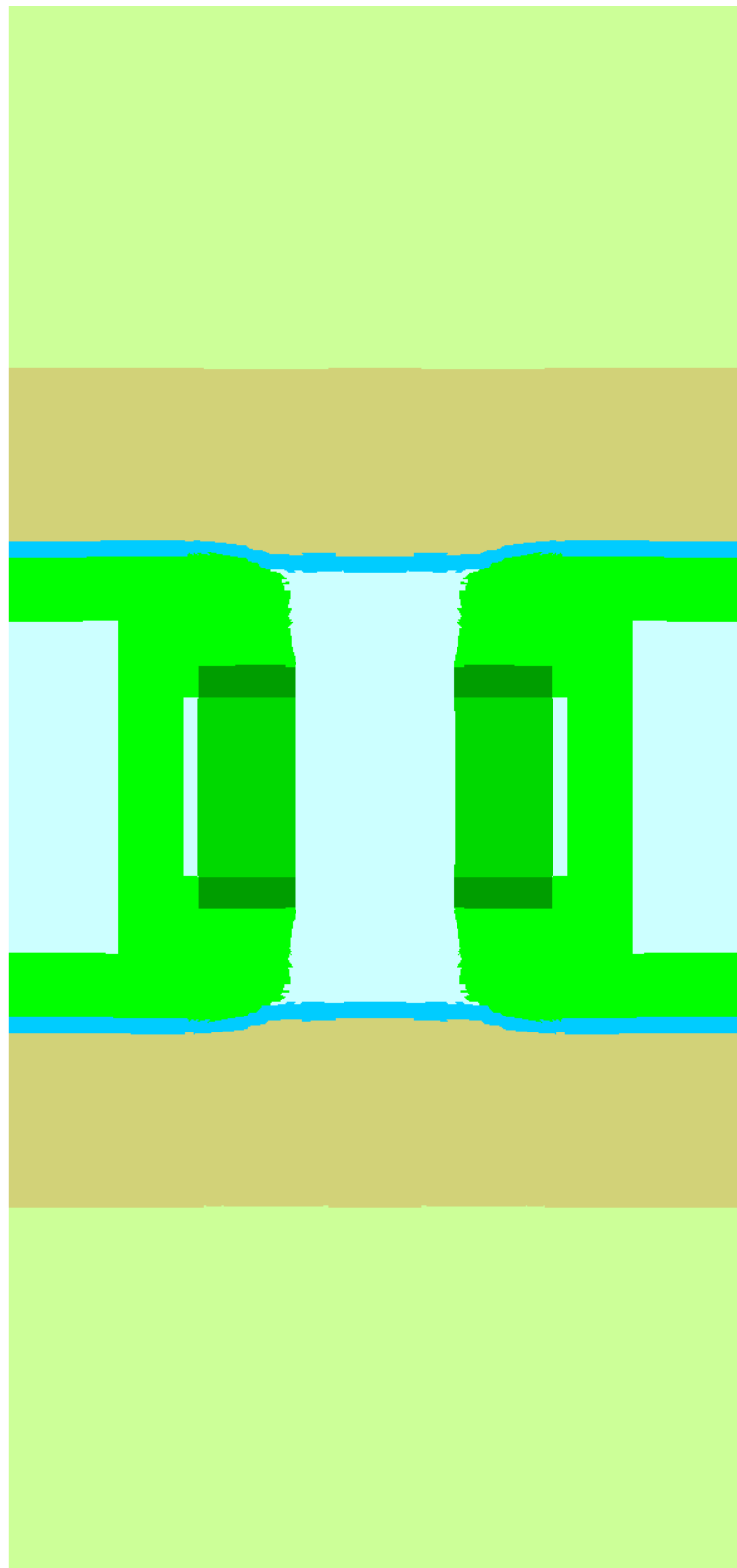


Figure 18: Predicted Test 1 configuration $t = 5 \mu s$

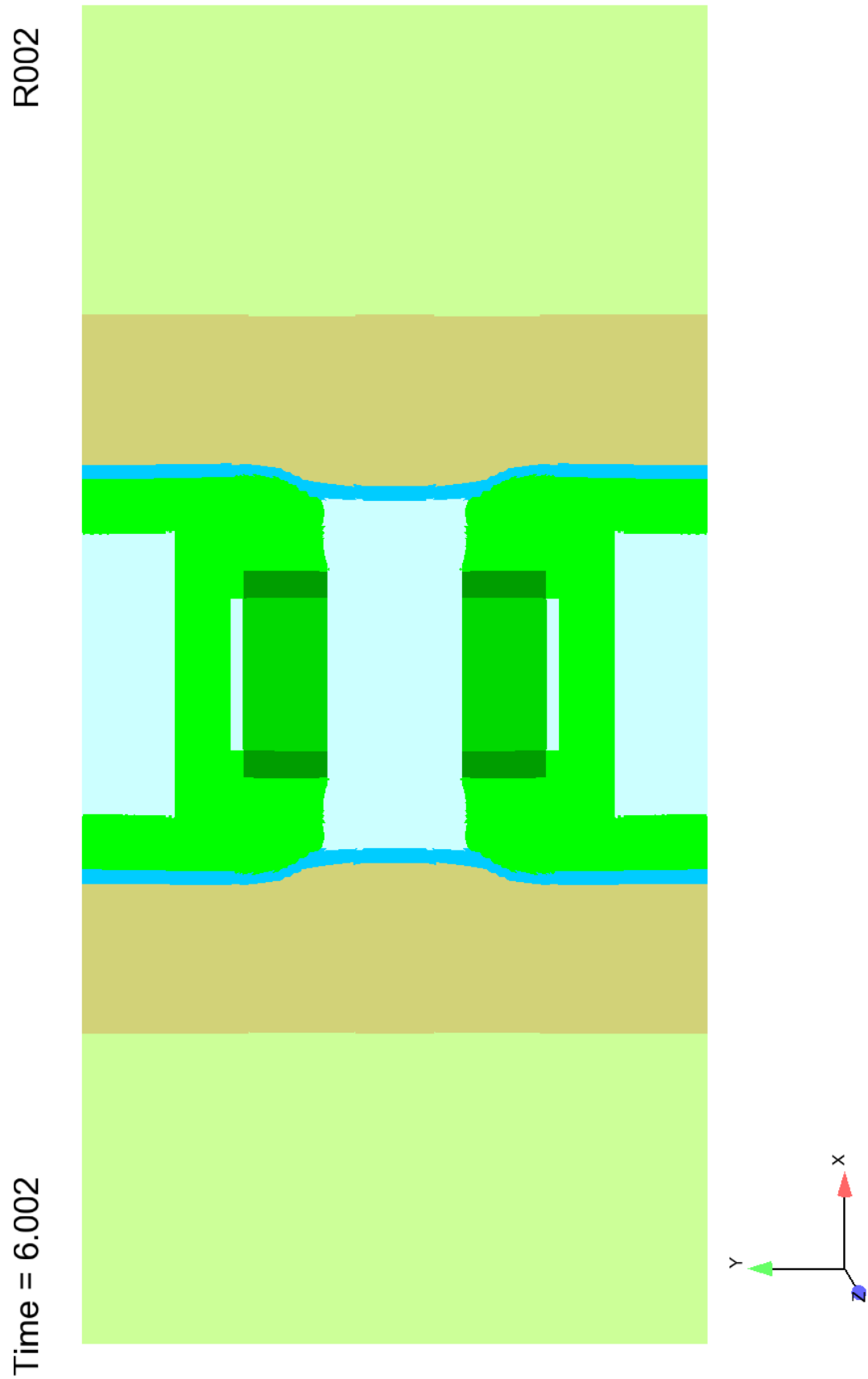


Figure 19: Predicted Test 1 configuration $t = 6 \mu s$

R002

Time = 7.002

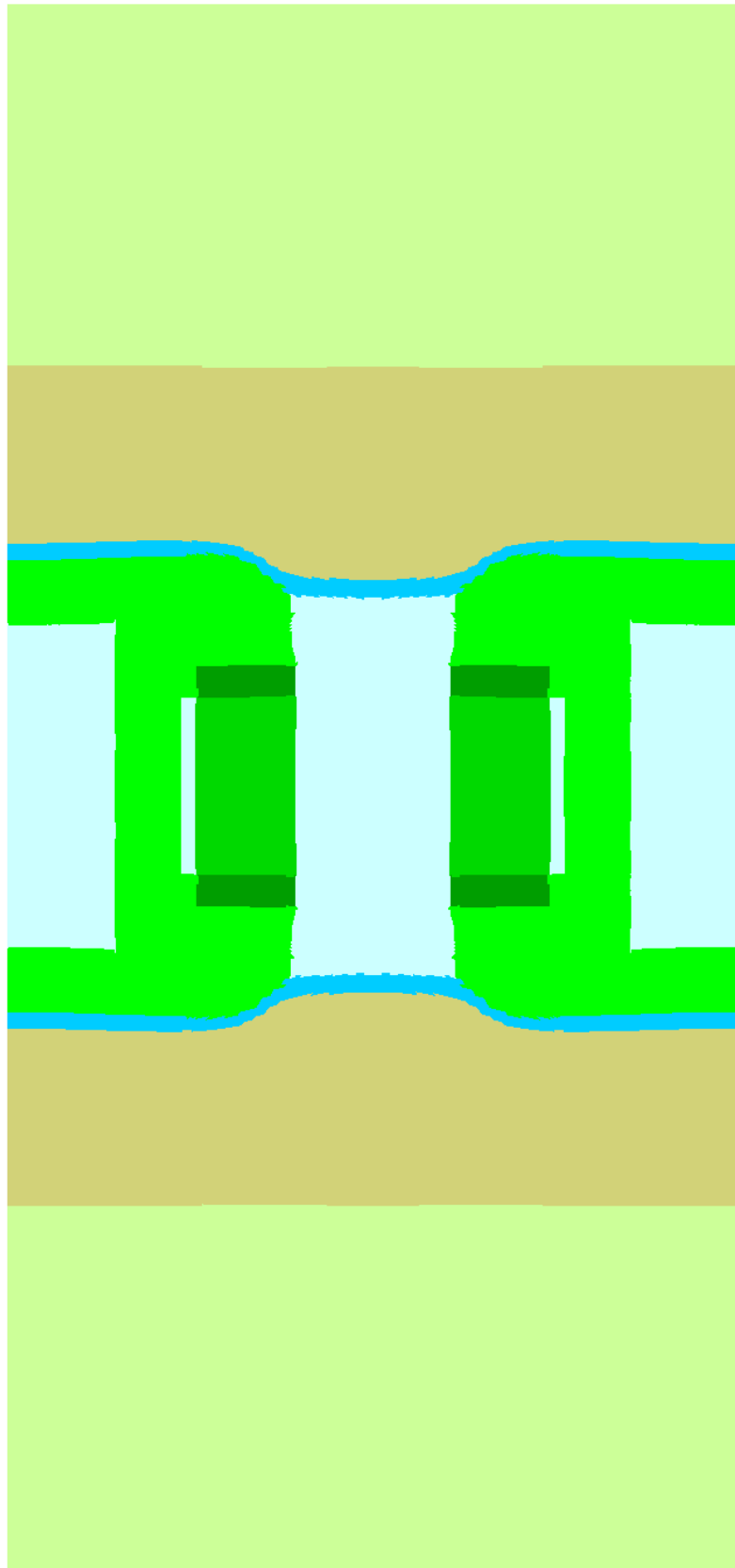


Figure 20: Predicted Test 1 configuration $t = 7 \mu s$

R002

Time = 8.002

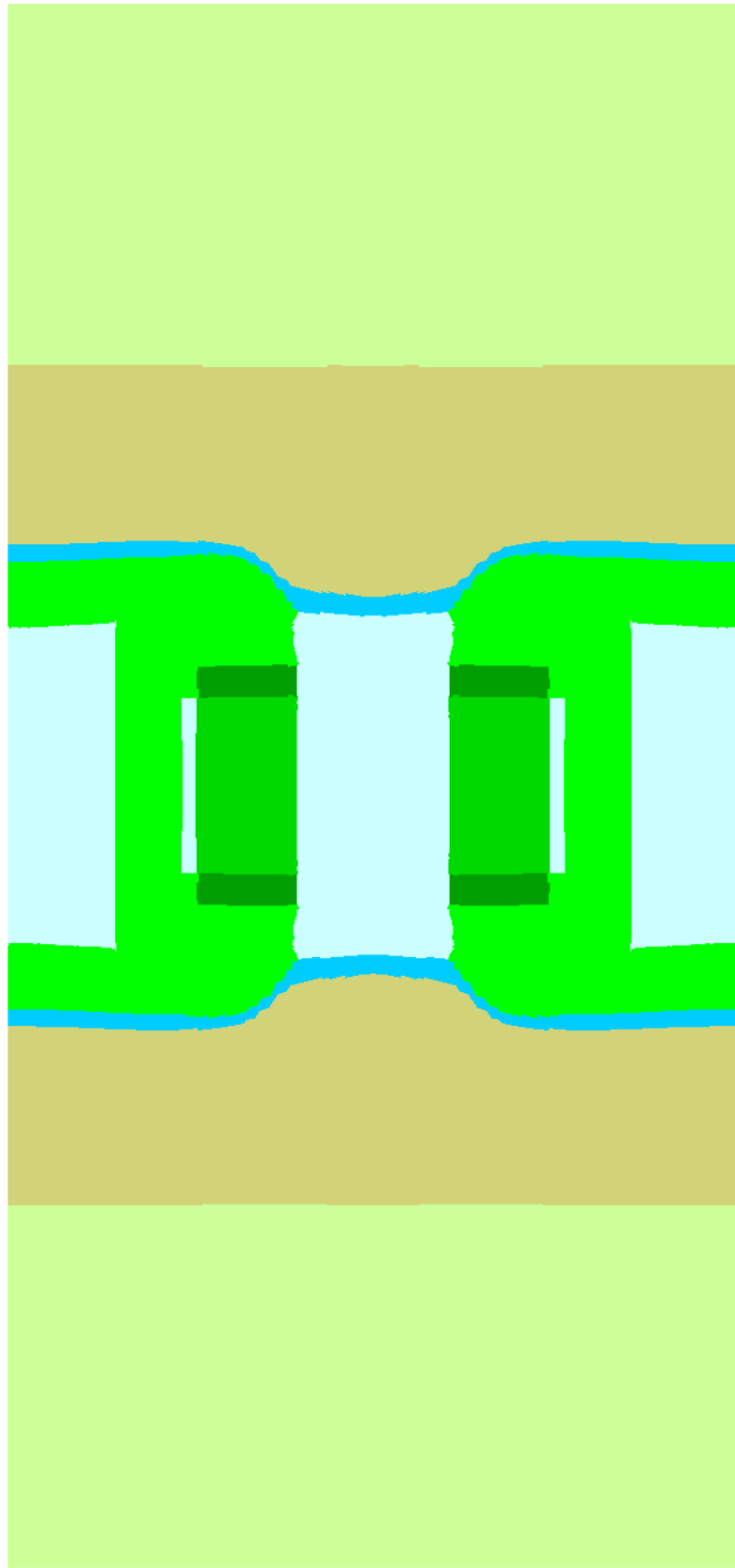


Figure 21: Predicted Test 1 configuration $t = 8 \mu s$

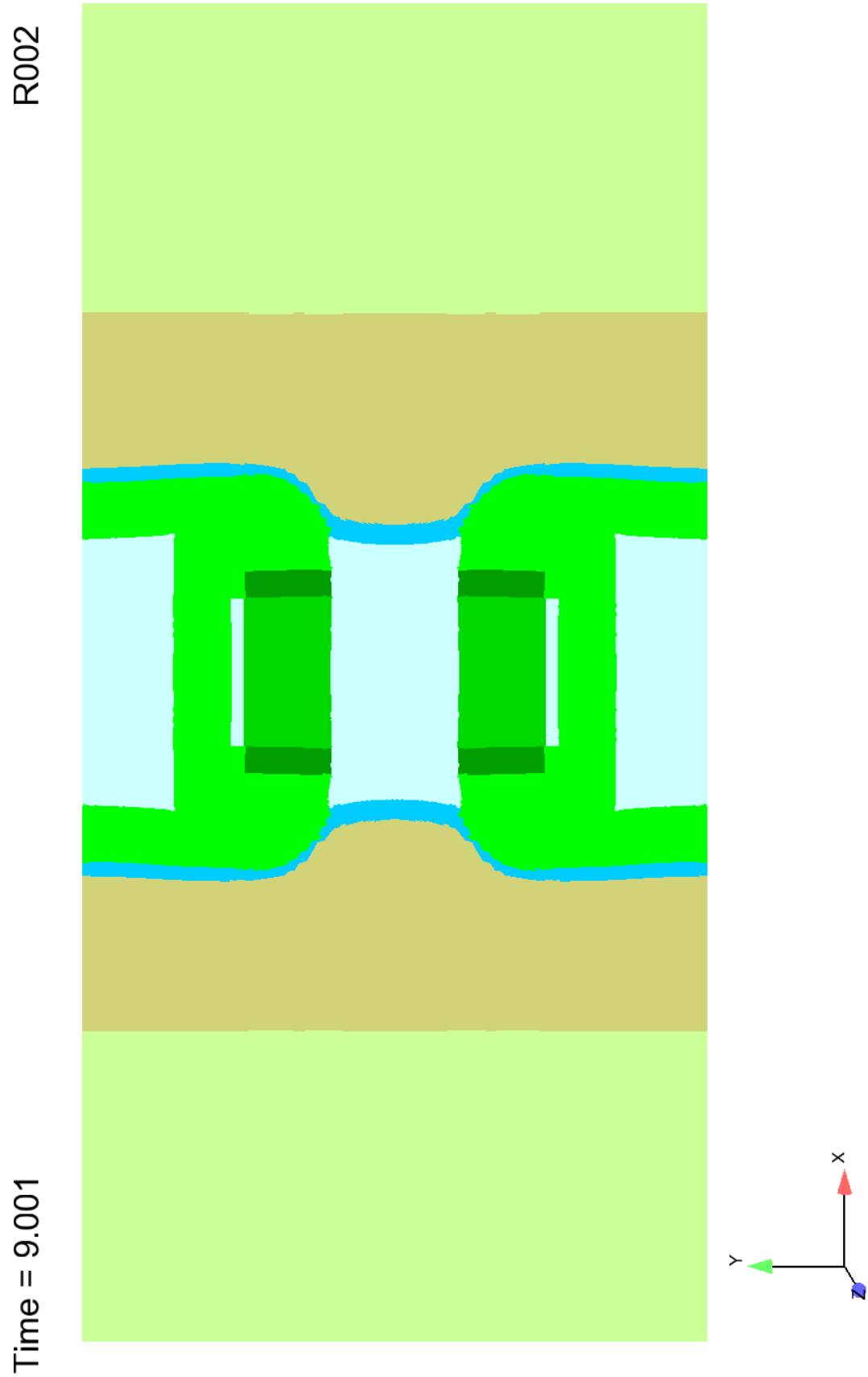


Figure 22: Predicted Test 1 configuration $t = 9 \mu s$

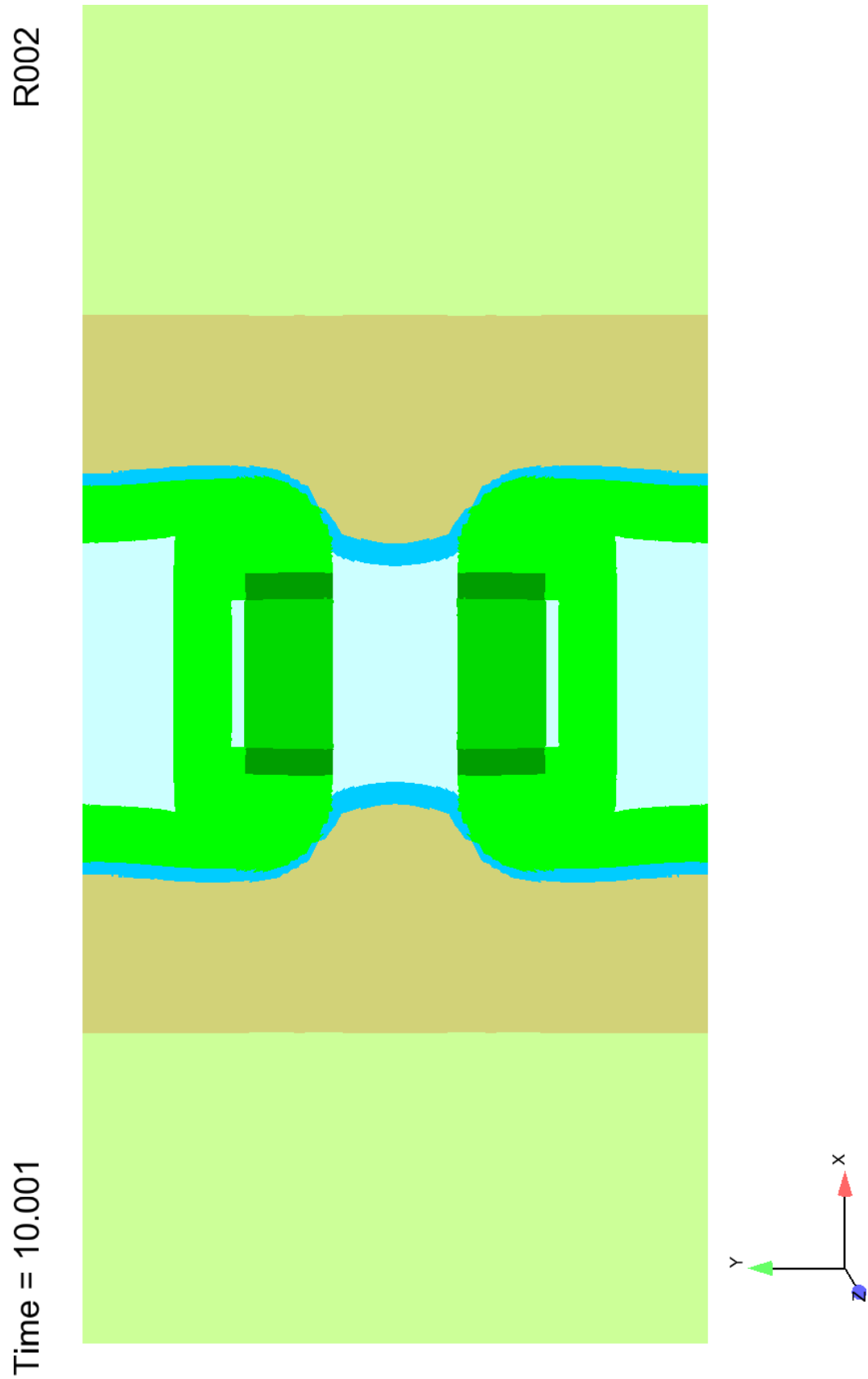


Figure 23: Predicted Test 1 configuration $t = 10 \mu s$

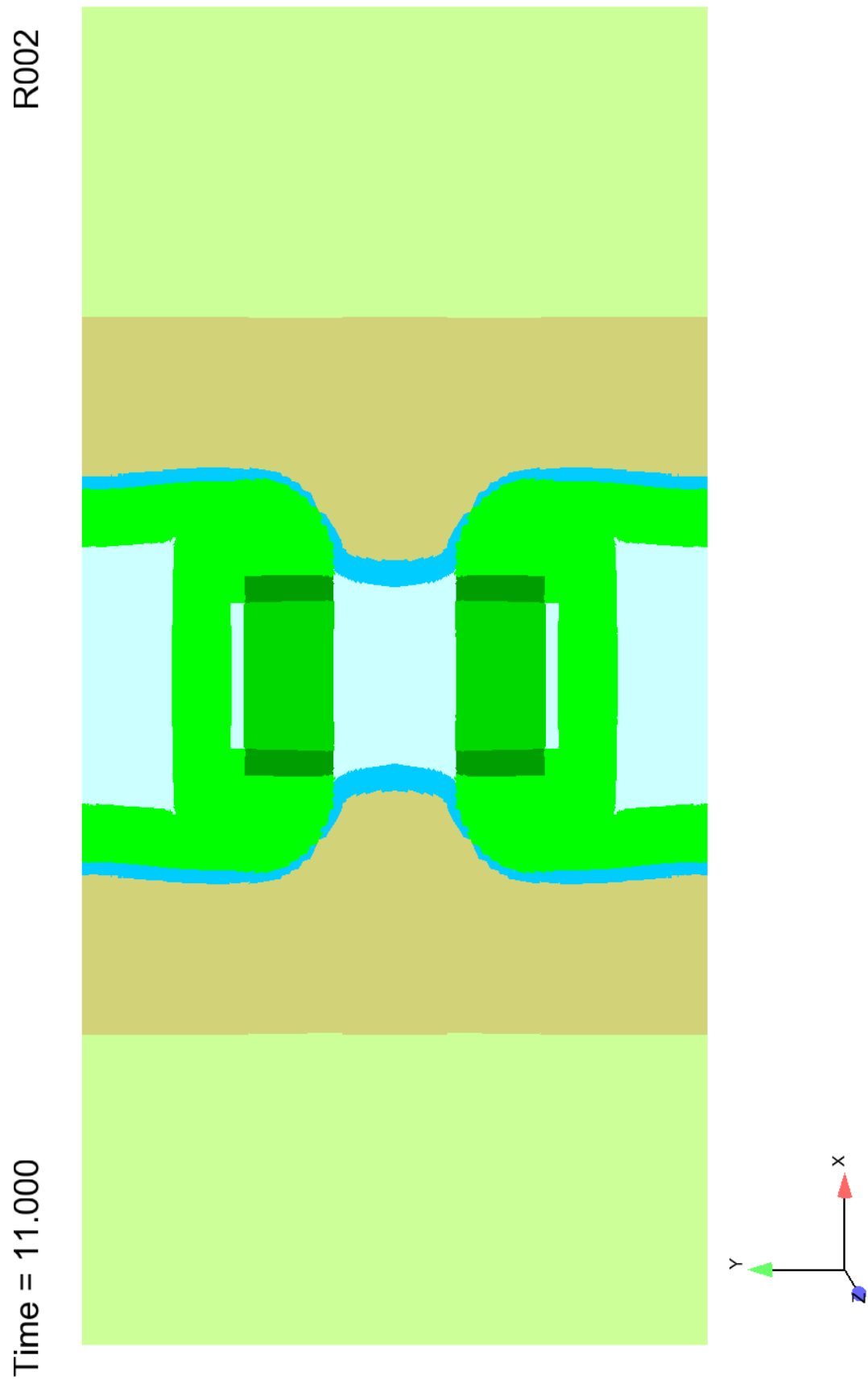


Figure 24: Predicted Test 1 configuration $t = 11 \mu s$

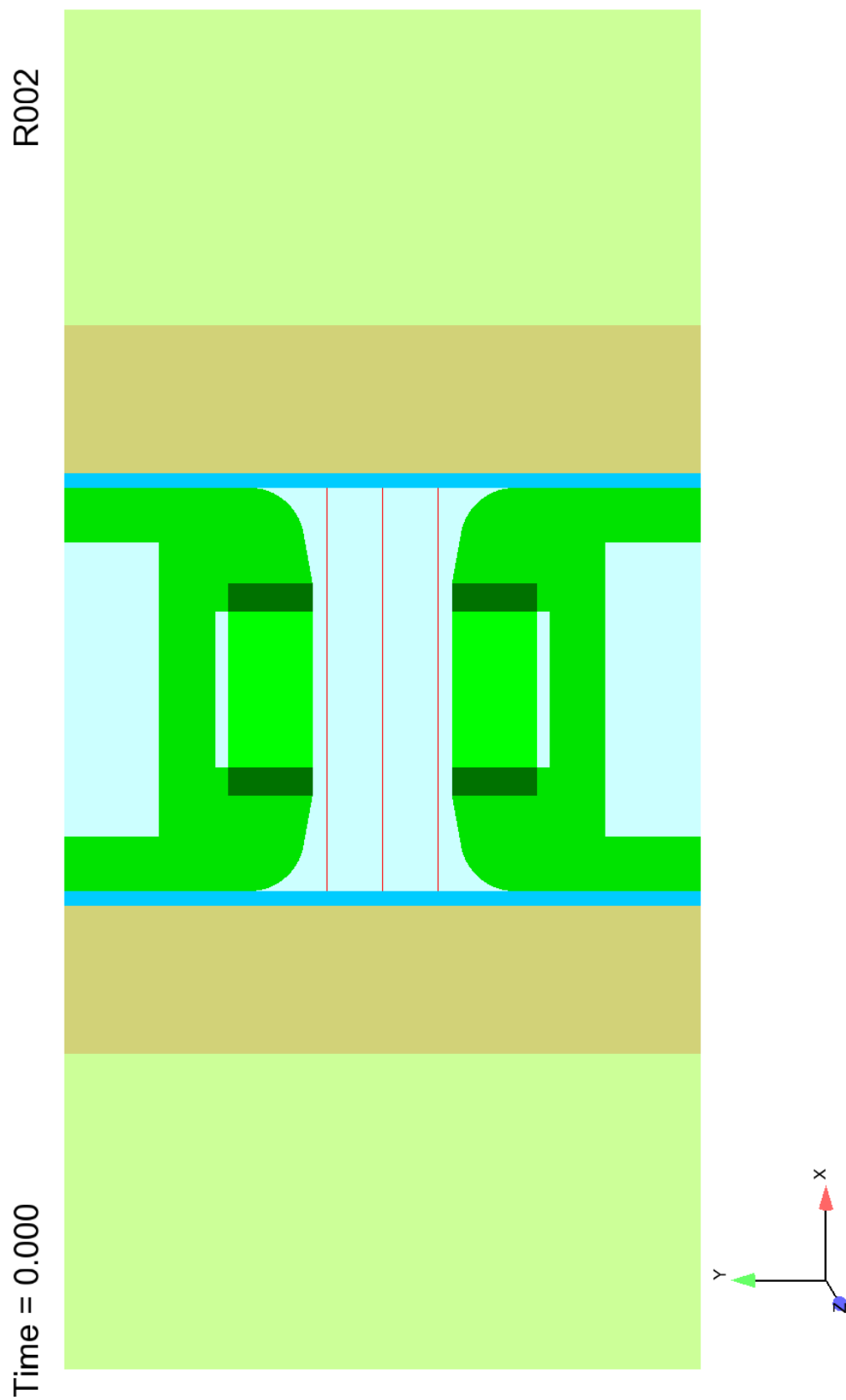


Figure 25: Test 1 configuration $t = 0 \mu s$ with PDV lines of sight depicted

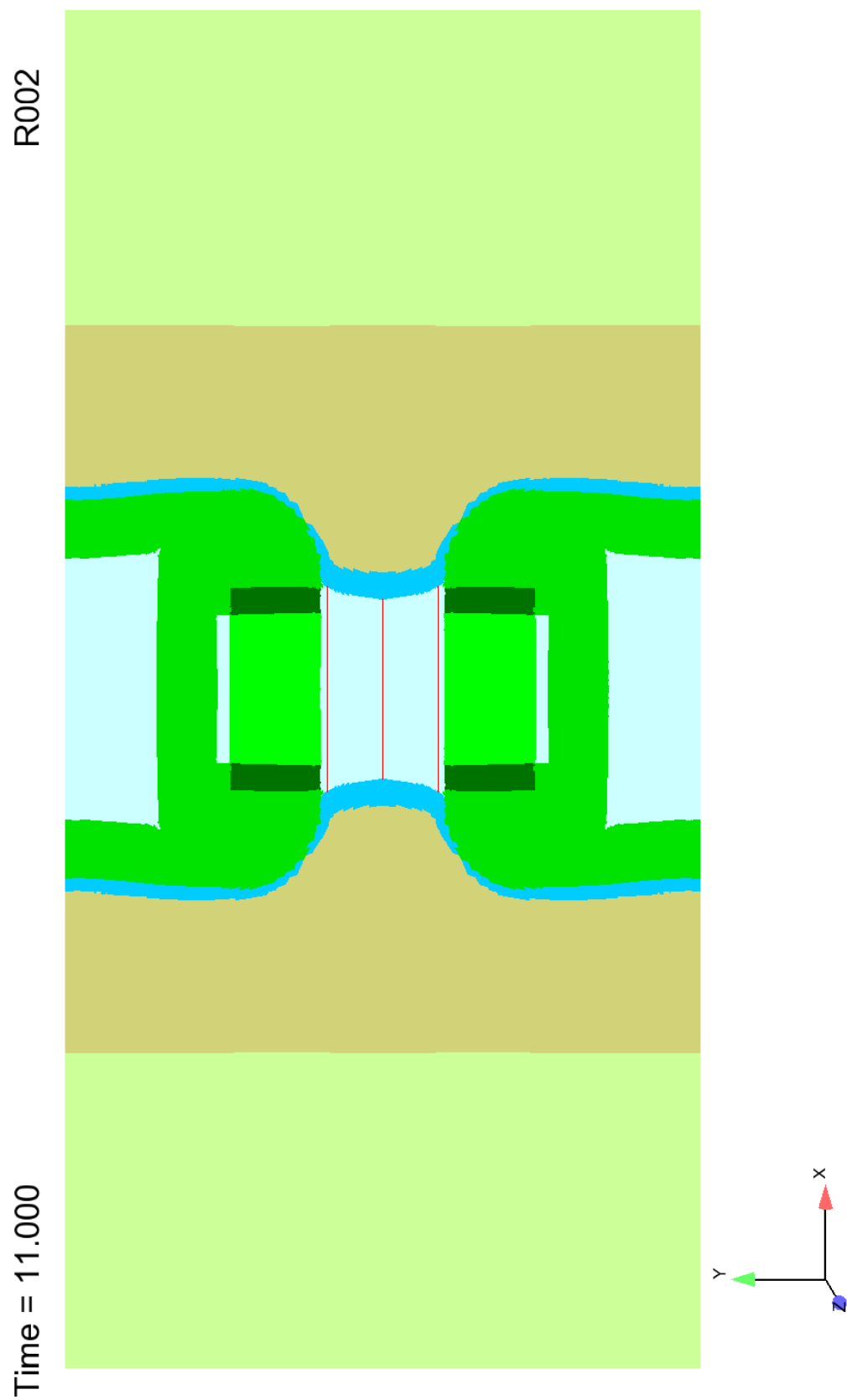


Figure 26: Predicted Test 1 configuration $t = 11 \mu\text{s}$ with PDV lines of sight depicted

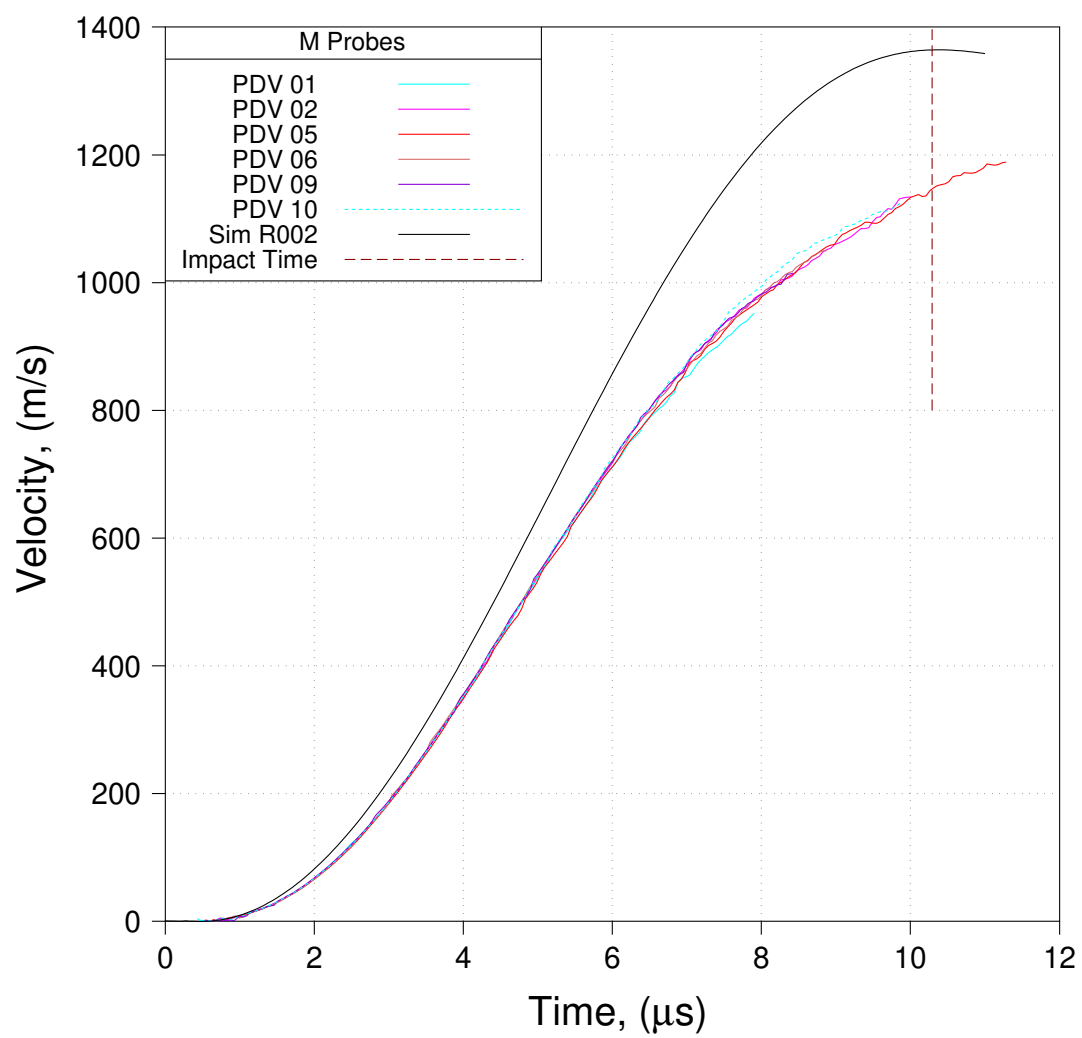


Figure 27: Test 1 Pre-Shot simulation compared to data (M Probes)

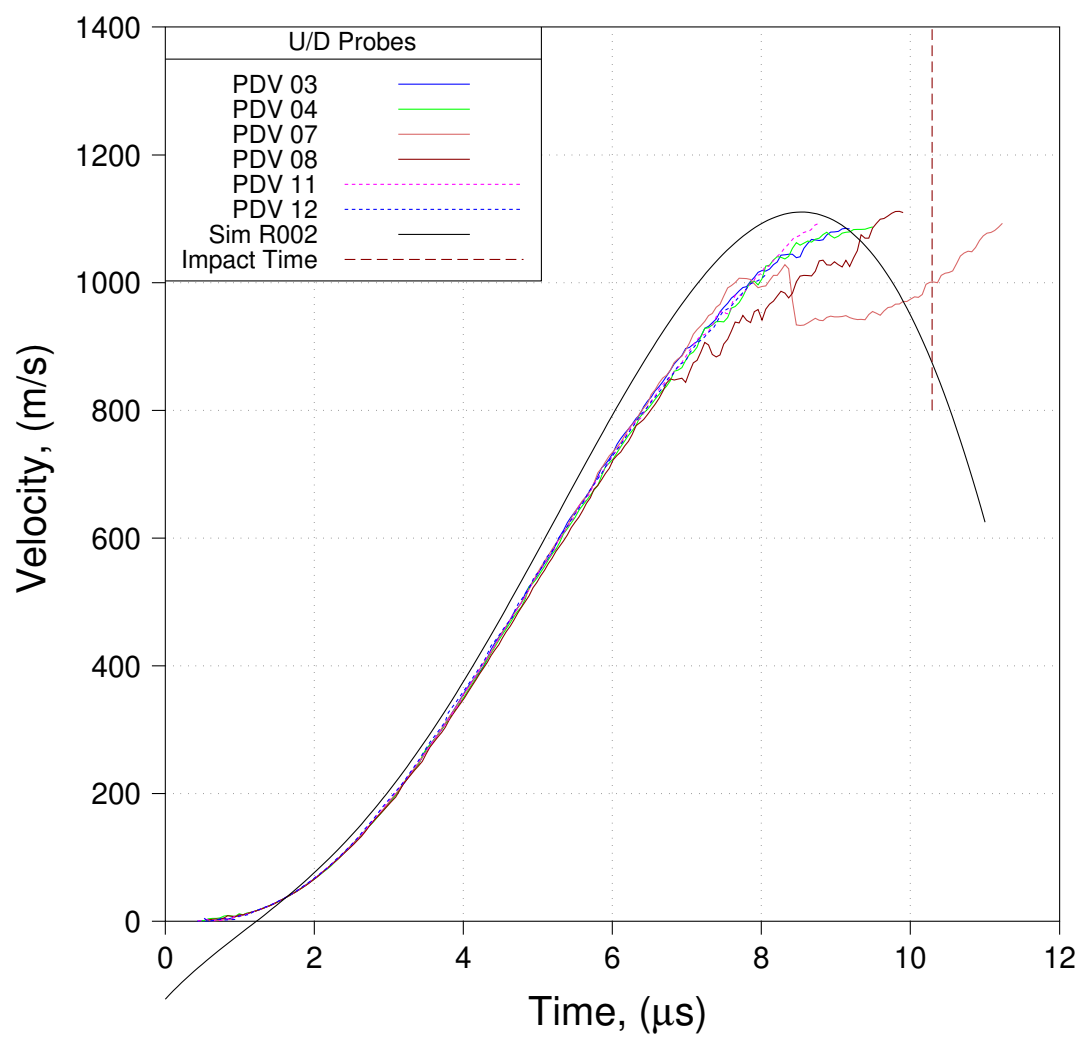


Figure 28: Test 1 Pre-Shot simulation compared to data (U/D Probes)

5.2 Test 1 Post-Shot Analysis

5.2.1 R015

As mentioned in the previous section, our R002 prediction of midplane velocity was significantly too high (recall Fig. 27). When we saw this we immediately suspected that our RLC circuitry was producing predicted currents that were too high. This suspicion was confirmed when we compared our predicted current to the current that was measured. That comparison is presented in Fig. 29.

FLAG provides an alternative to the RLC circuitry that delivers current to the MHD package. That alternative is to input the current from a table. In R015 we did just that. Instead of calculating the current, we entered the current in tabular form, using the measured current shown in Fig. 29 as input. Thus we used experimental output as input to our MHD calculations. Simulation results compared to empirical data from R015 are shown in Figs. 30 and 31.

We observe (Fig. 30) that by using tabular input of the measured current our prediction of midplane velocity is greatly improved. However, there remain some unsettling features in the prediction of upstream/downstream velocities. We still predict that the liner moves in the wrong direction at early time (negative velocity) and we still have a significant drop in velocity at late times that is not seen in the empirical data. Moreover, the R015 prediction of U/D velocities is worse than that of R002 (compare Fig. 28 to Fig. 31).

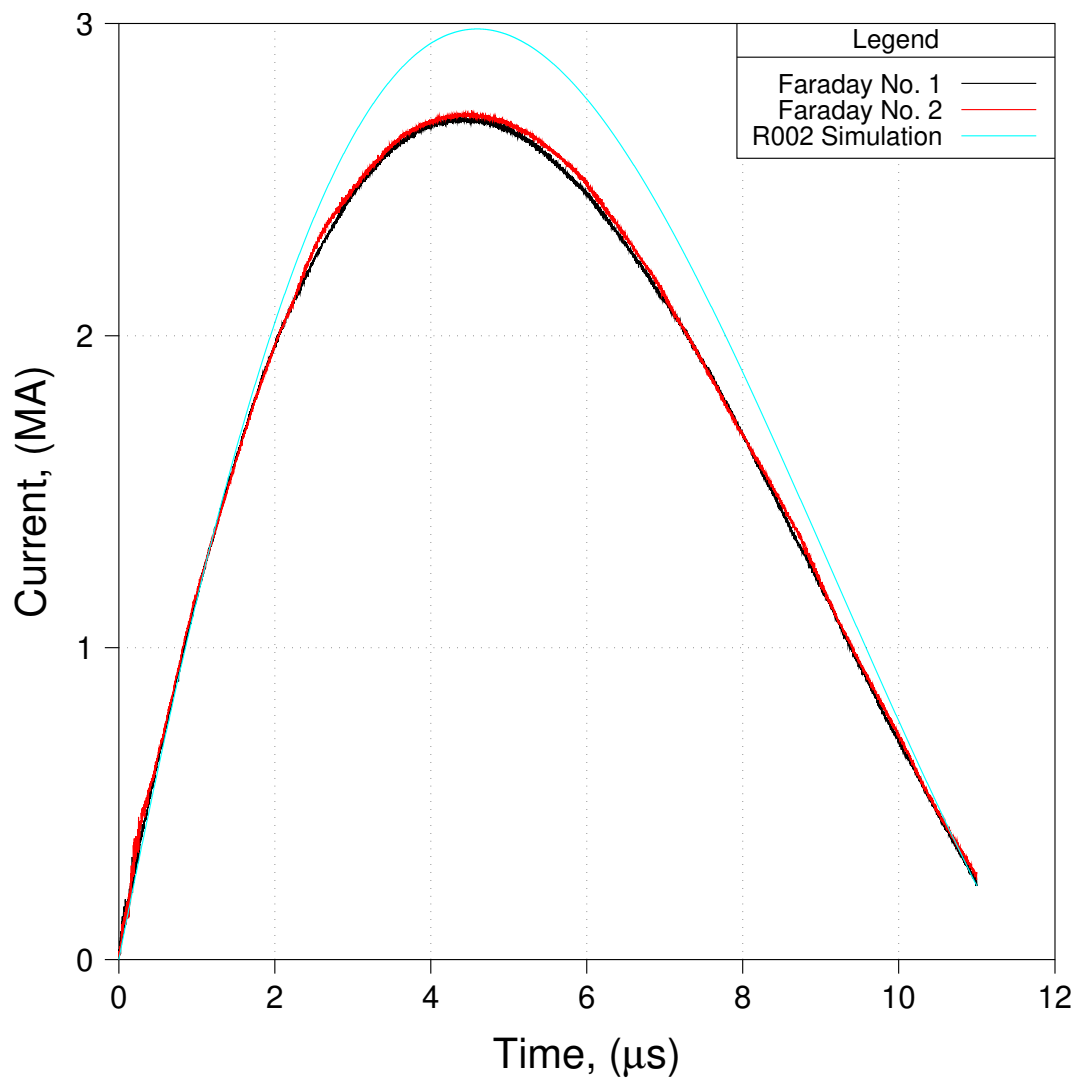


Figure 29: Predicted current compared to measured current – Test 1

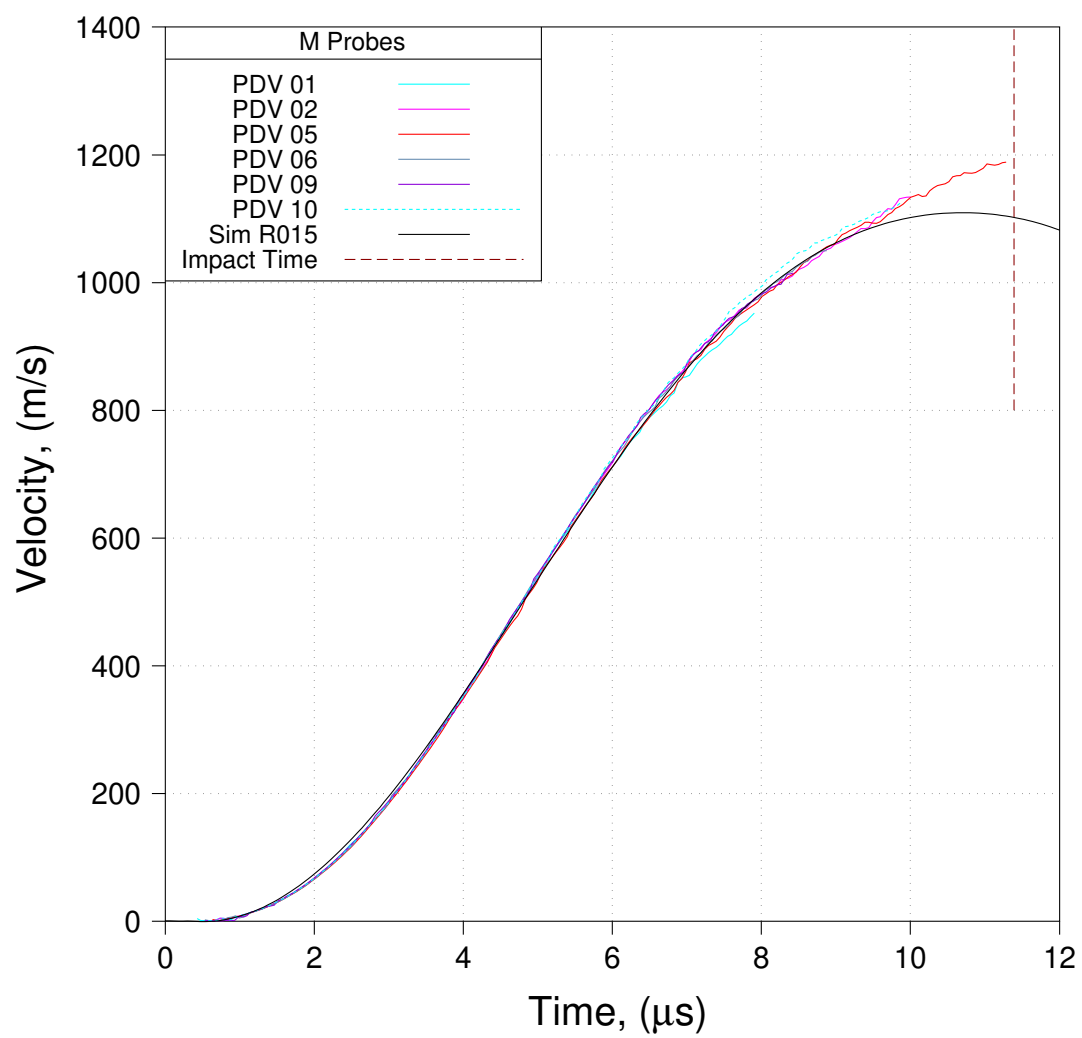


Figure 30: R015 simulation compared to data (M Probes)

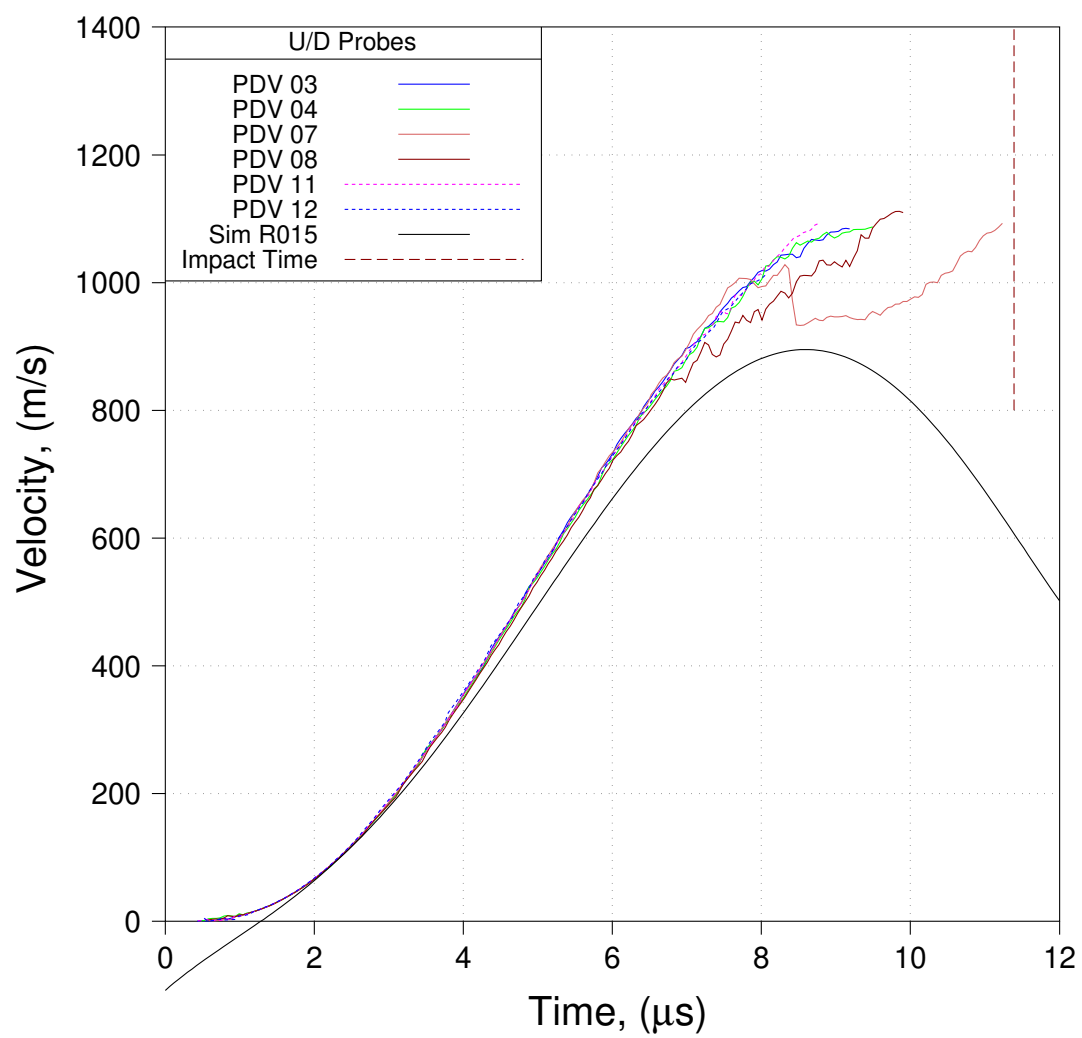


Figure 31: R015 simulation compared to data (U/D Probes)

5.2.2 R017

As mentioned in the previous section, our R015 prediction of midplane velocity was much improved (compare Fig. 27 to Fig. 30). However, our prediction of U/D velocity was appreciably worse (compare Fig. 28 to Fig. 31). Moreover, the R015 prediction of U/D velocities, as was the case with the R002 prediction, possesses two unreasonable features: (1) the liner is predicted to move in the wrong direction at early time, and (2) the U/D velocities are predicted to significantly decrease at late time in a manner that is not observed in the empirical data.

When we saw this we immediately suspected that the reason for negative velocities at early time might be related to an overly aggressive application of nodal relaxation and material mixing. In R002 and in R015 we applied fset relaxation over the entire mesh. Doing this makes simulation failures due to tangling, chevron or hourglassing problems, or Courant time limiting, to be much less likely, and is, in some cases, warranted. However, in this case, relaxation over the universe was, as we shall see, a mistake. Relaxing over the universe allows for material mixing throughout. In some cases this is reasonable; in other cases it is unreasonable. If you look at Figs. 14 - 24, you will note a very rough demarcation between vacuum and liner. This is because liner and vacuum are mixing in our simulation. Since the liner does not vaporize in the experiment (it does not even liquify), mixing of this nature is not physically reasonable. When this mixing occurs, FLAG uses an interface tracking model (in this case a Youngs method of interface reconstruction [8],[9]) in order to identify the demarcation between liner and vacuum. We suspected, based upon careful observation of the R015 simulation results, that at early time, when the liner and vacuum mix, the calculated interface moved into the liner (making the interface appear to move in the wrong direction). We surmized that this is the reason for predicted U/D velocities to be negative at early time.

To test this supposition, we modified our relaxation scheme such that mixing of liner and vacuum would not be allowed. In R017 we allowed relaxation and mixing to occur within a region (denoted R01) that included everything to the left of the liner, and we allowed relaxation and mixing to occur within a region (denoted R02) that included everything to the right of the liner. Predicted velocities from R017 are shown in Figs. 32 and 33. We observe that the prediction of M velocity is quite reasonable and we have eliminated the troublesome negative velocities in the U/D predictions at early time. Now if we can eliminate the significant decrease in U/D velocity prediction at late time then our simulation prediction will be greatly improved, and may even be thought to be reasonably accurate.

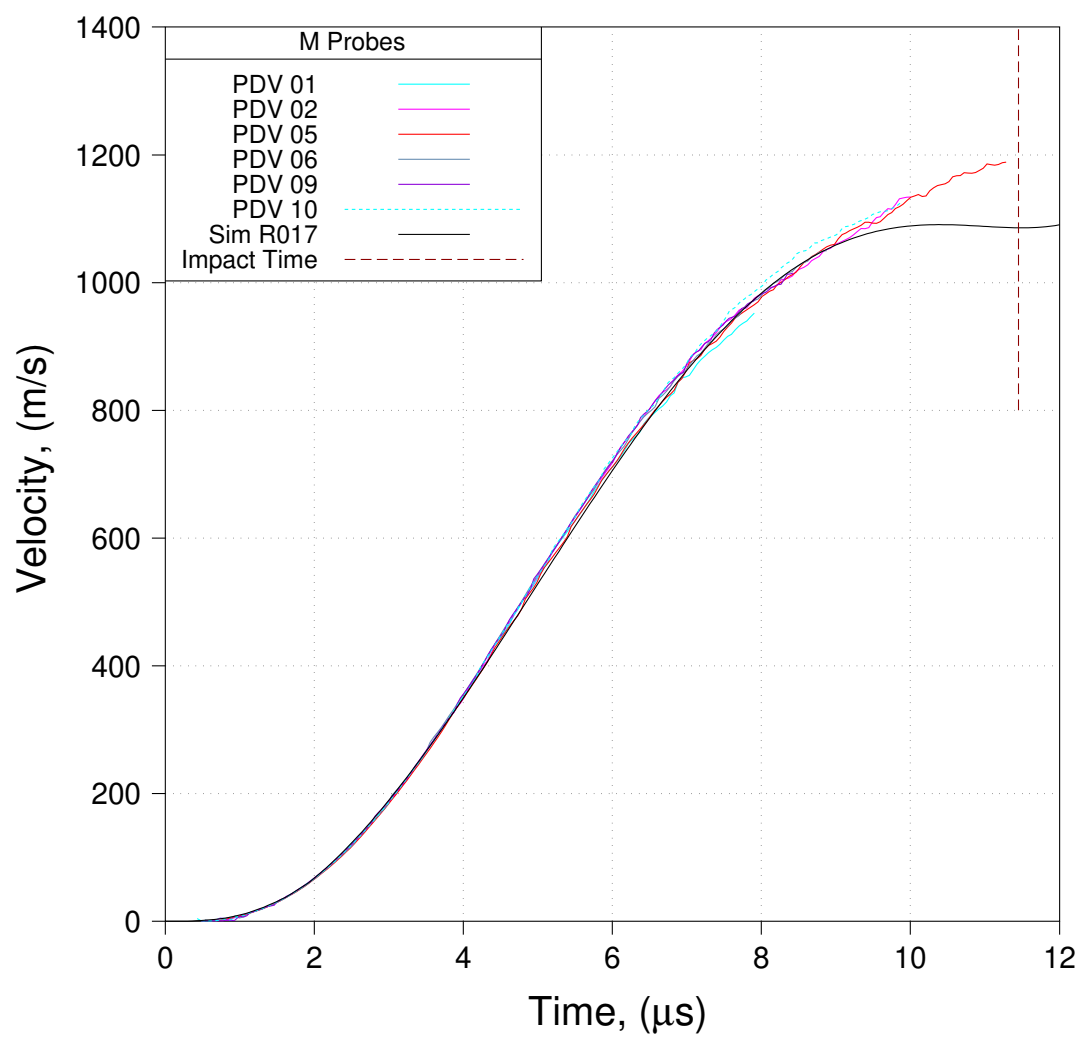


Figure 32: R017 simulation compared to data (M Probes)

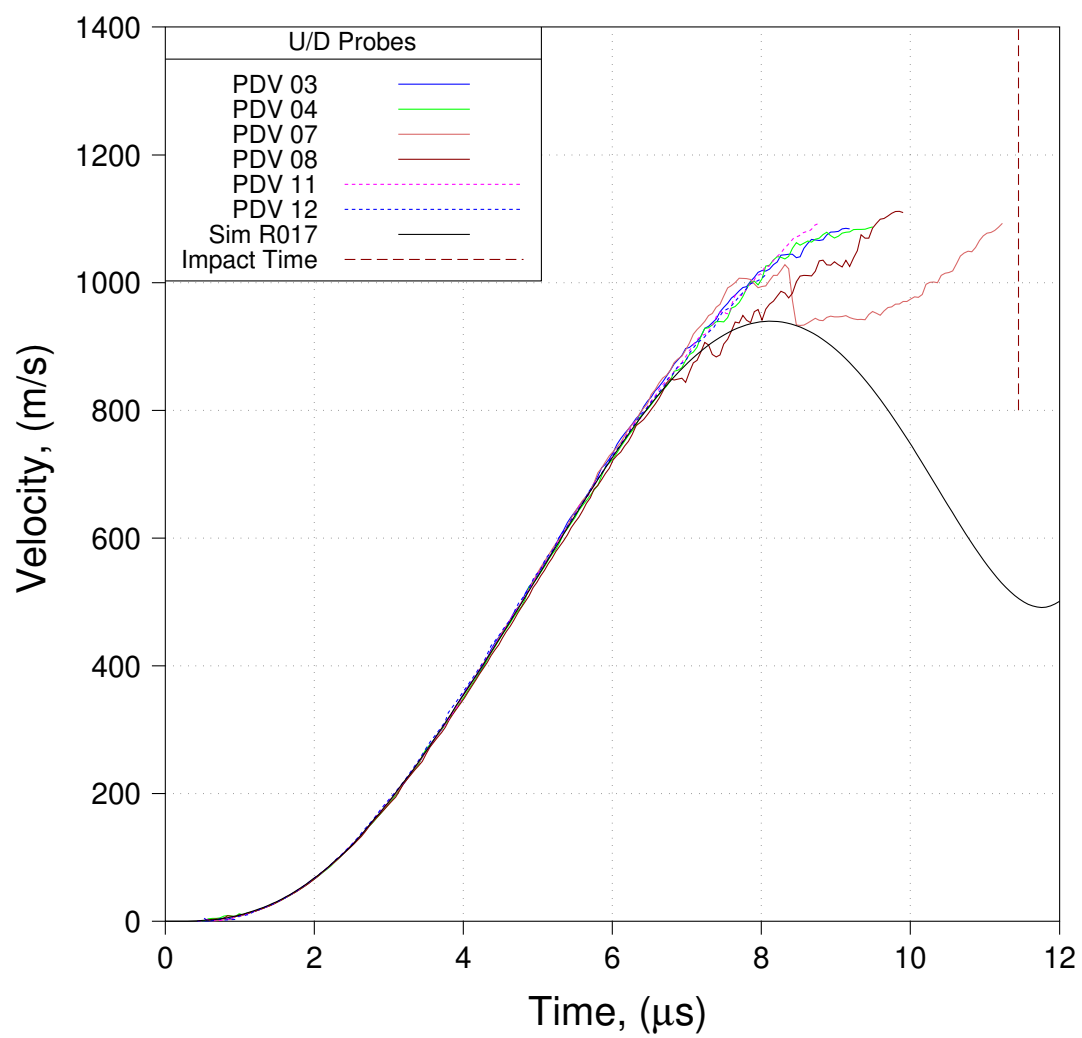


Figure 33: R017 simulation compared to data (U/D Probes)

5.2.3 R053

To this point in our discussion we have separated an evaluation of predicted midplane velocities from that of predicted upstream/downstream velocities. This is quite reasonable if there is an appreciable difference between measured midplane velocities and measured upstream/downstream velocities. However, if we carefully consider the empirical data presented in Figs. 4-6 and in Figs. 8-10, we note that there is no appreciable difference; midplane, upstream, and downstream velocities all track about the same. Consequently, we should expect that the leading edge of the liner should trace an approximately straight line between the upper and lower glide planes. This is not what is seen in the simulation results that we have considered thus far (see for example Fig. 24, which was obtained from R002). It is not what is seen in the results obtained from R015 or R017 either.

As seen in the previous section, the R017 predictions were reasonably accurate with the exception of a drop in U/D velocity starting at about $8.5 \mu\text{s}$. We also note, as just discussed, that in the R017 results there are significant differences between midplane and U/D velocity predictions, resulting in significant curvature of the leading edge of the liner between upper and lower glide planes. Careful evaluation of R017 (and previous runs) led the authors to believe that potential for improvement in predictive accuracy resides in improving mesh smoothness. We will not tire the reader with discussions of all of the many simulations that were conducted post-R017, but rather, will “fast-forward” to R053, which is really a culmination of what took place R018-R052.

Most of the modeling refinements that were employed post R017 focused on maintaining mesh smoothness. The first refinement, first employed in R025, was to replace the mesh shown in Fig. 12, which was not *a priori* completely smooth, with a fully uniform mesh. The new mesh is shown in Fig. 34. A second major refinement had to do with our relaxation scheme. In R053 we have four relaxation regions: Rel01-Rel03, and Rel05. Relaxation region 01 consists of everything to the left of the liner (this includes glide plane, end cap, driver, upper and lower air, and vacuum); relaxation region 02 consists of the liner; relaxation region 03 consists of everything to the right of the liner (this includes insulator and return conductor). Relaxation region 05 is shown (in grey) in Fig. 35. In the following paragraph we shall describe our R053 relaxation scheme.

For the most part the fset relaxer was active in relaxation regions 01-03 from $t = 0$ to end-of-run. However, relaxation in these three regions was turned off during six very short time periods. During these very short time periods when relaxation was turned off in relaxation regions 01-03, fset relaxation was turned on in relaxation region 05. This was done to accomplish localized smoothing in an area wherein smoothness suffered without this supplemental localized smoothing operation. The time periods during which relaxation was turned off in relaxation regions 01-03 (and was turned on in relaxation region 05) are provided in Table 9. The impact of this localized smoothing is illustrated in Figs. 36 and 37. We see in Fig. 36 that at $8.000 \mu\text{s}$, at the point where the glide plane, liner, and vacuum come together (approximately in the center of the figure), a localized loss of smoothness is developing. In Fig. 37 we see improvement in smoothness at that location at $8.001 \mu\text{s}$ (this is after $0.001 \mu\text{s}$ of relaxation within relaxation region 05). Similar localized improvements in smoothness occur during time periods 02-06 (Table 9). Figures 38 - 50 depict the evolution of the assembly from 0 to $11 \mu\text{s}$. You will note that the leading edge of the liner forms a practically a straight line between upper and lower glide planes in all of these figures, much straighter than what we saw previously (compare Fig. 24 to 49).

Finally, in Fig. 51 we compare predicted to measured velocities using the results from R053. The comparison has now greatly improved over what we started with (in R002). Note that the midplane and upstream/downstream predictions fall one on top of another (at least within the width of the lines drawn in Fig. 51. Note also that the predictions are in very good agreement with the empirical data.

Table 9: Time periods when relaxation in relaxation regions 01-03 is turned off and relaxation in relaxation region 05 is turned on

Time Period	Duration
01	8.000 t0 8.001 μs
02	9.000 t0 9.002 μs
03	10.000 t0 10.002 μs
04	10.500 t0 10.502 μs
05	11.000 t0 11.002 μs
06	11.500 t0 11.502 μs

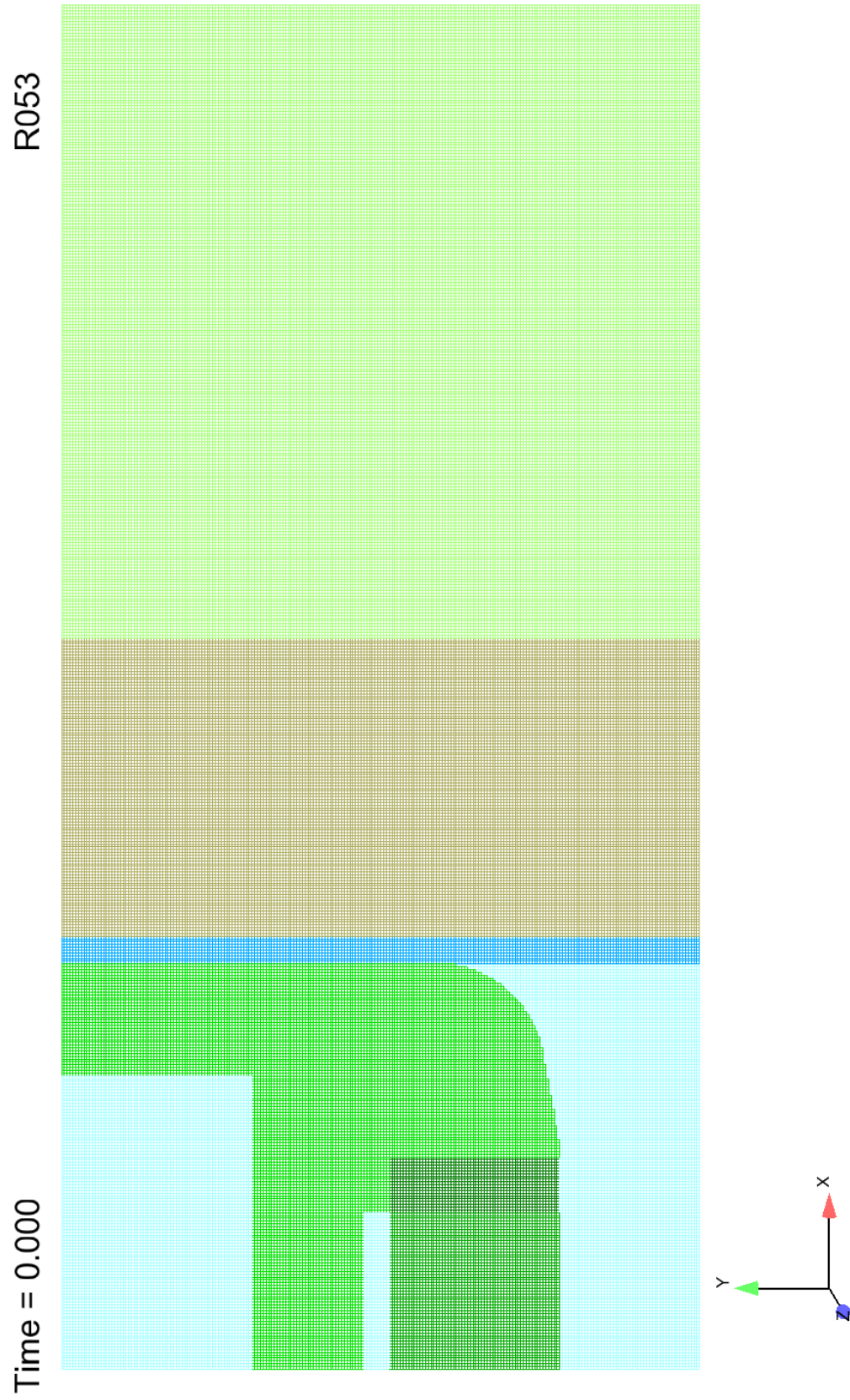


Figure 34: Uniform mesh used in R053

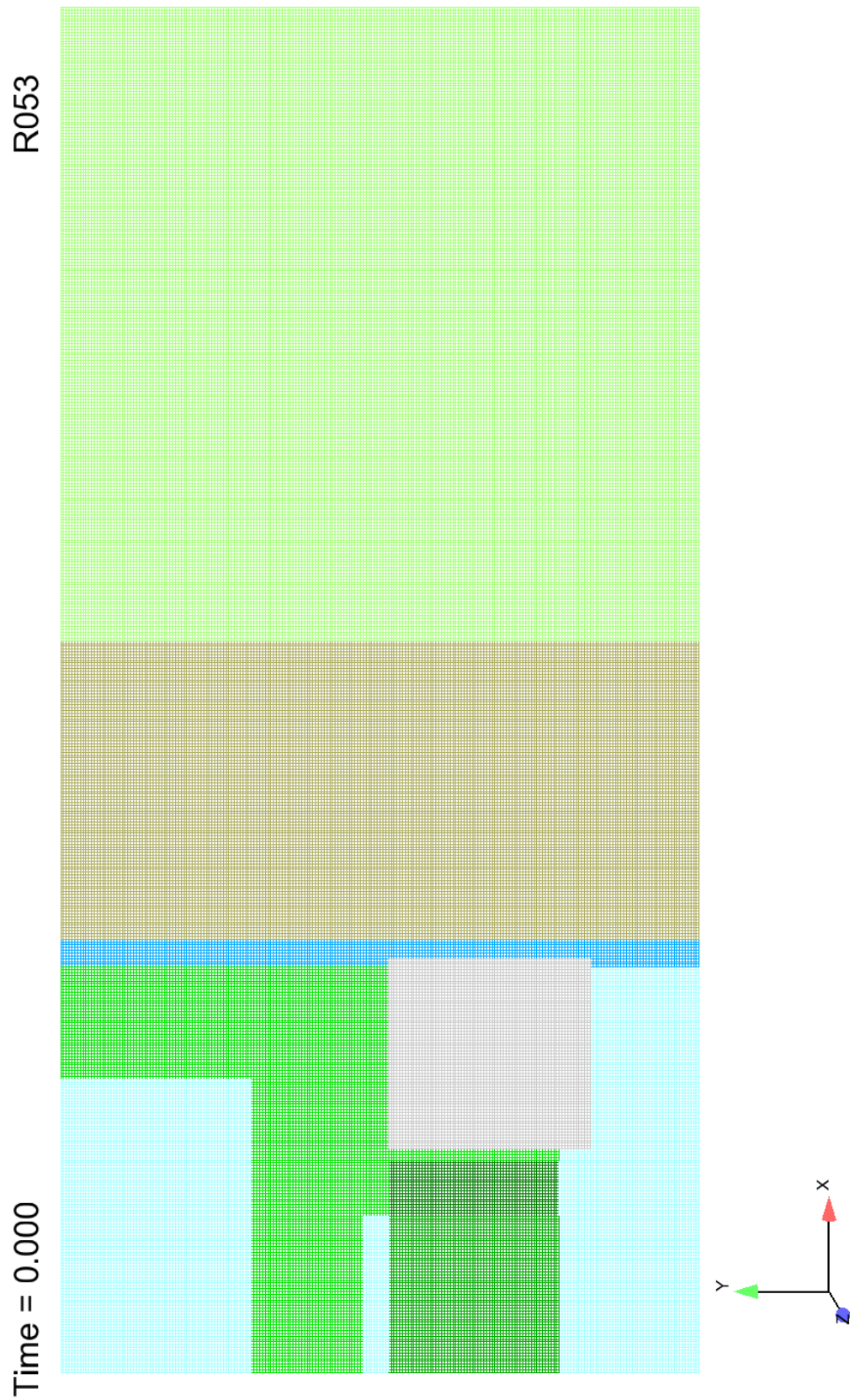


Figure 35: Relaxation region 05 (colored grey)

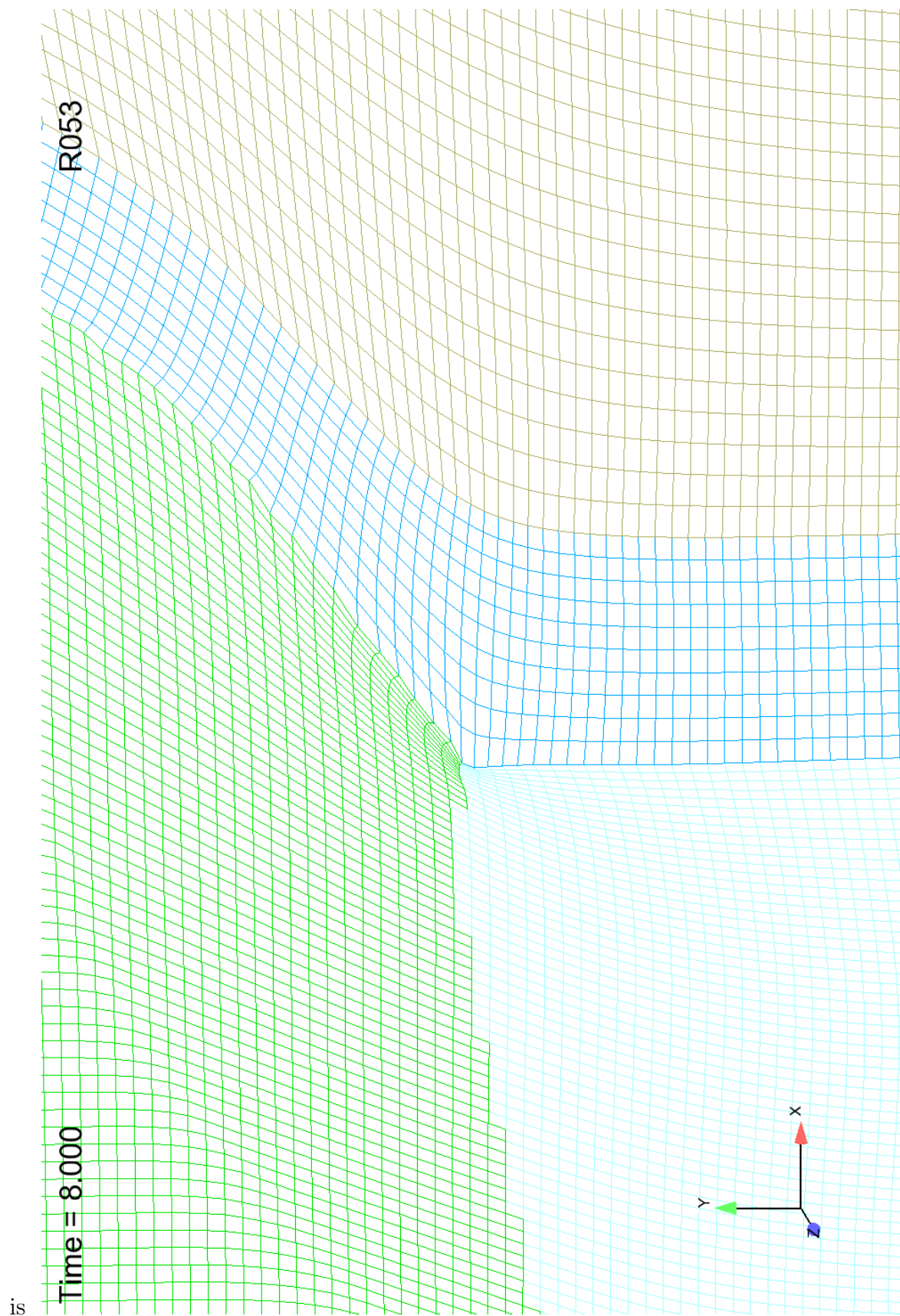


Figure 36: Localized diminishing of smoothness at $t = 8.0\mu s$

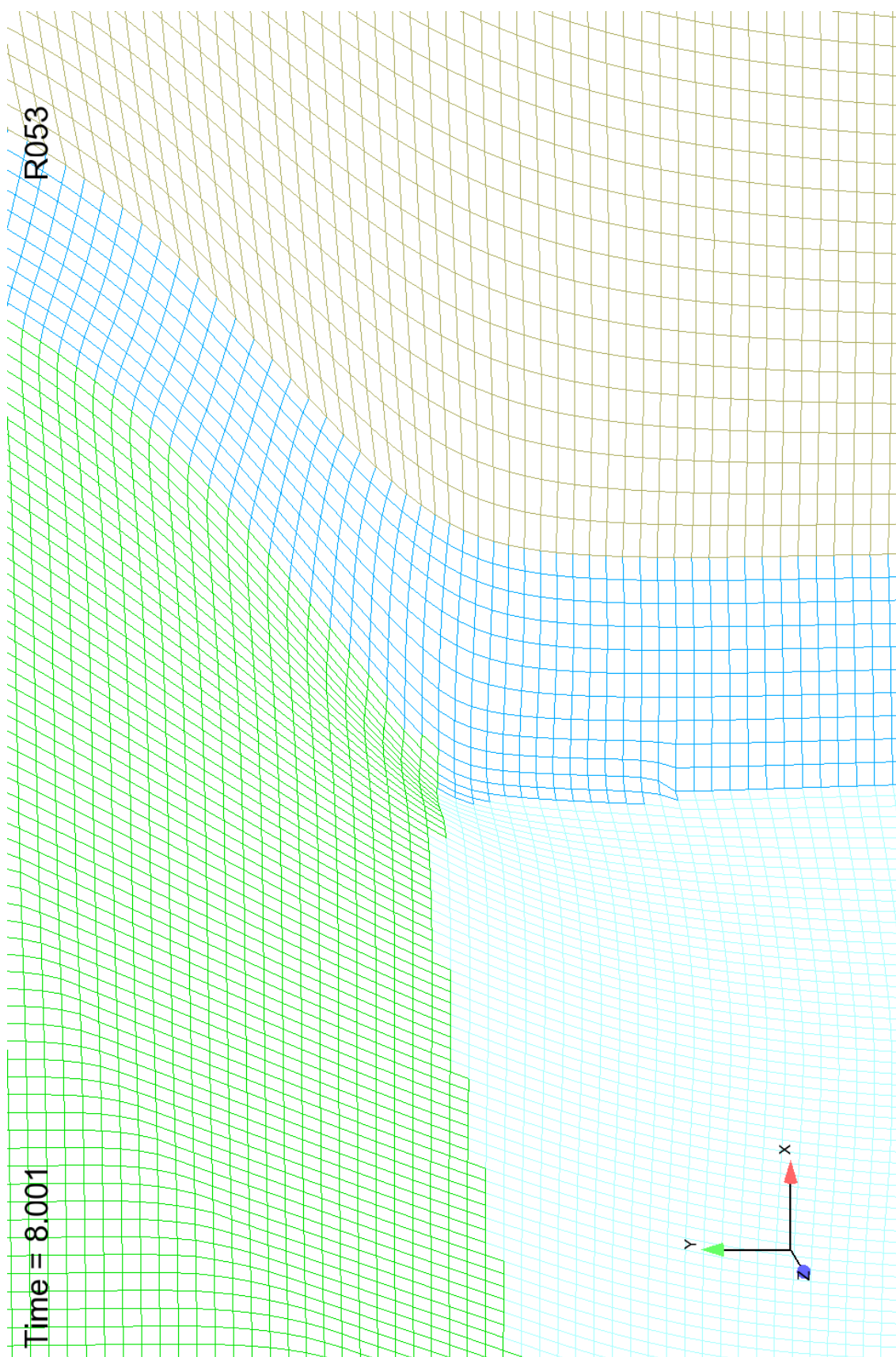


Figure 37: Localized improvement in smoothness at $t = 8.001\mu s$

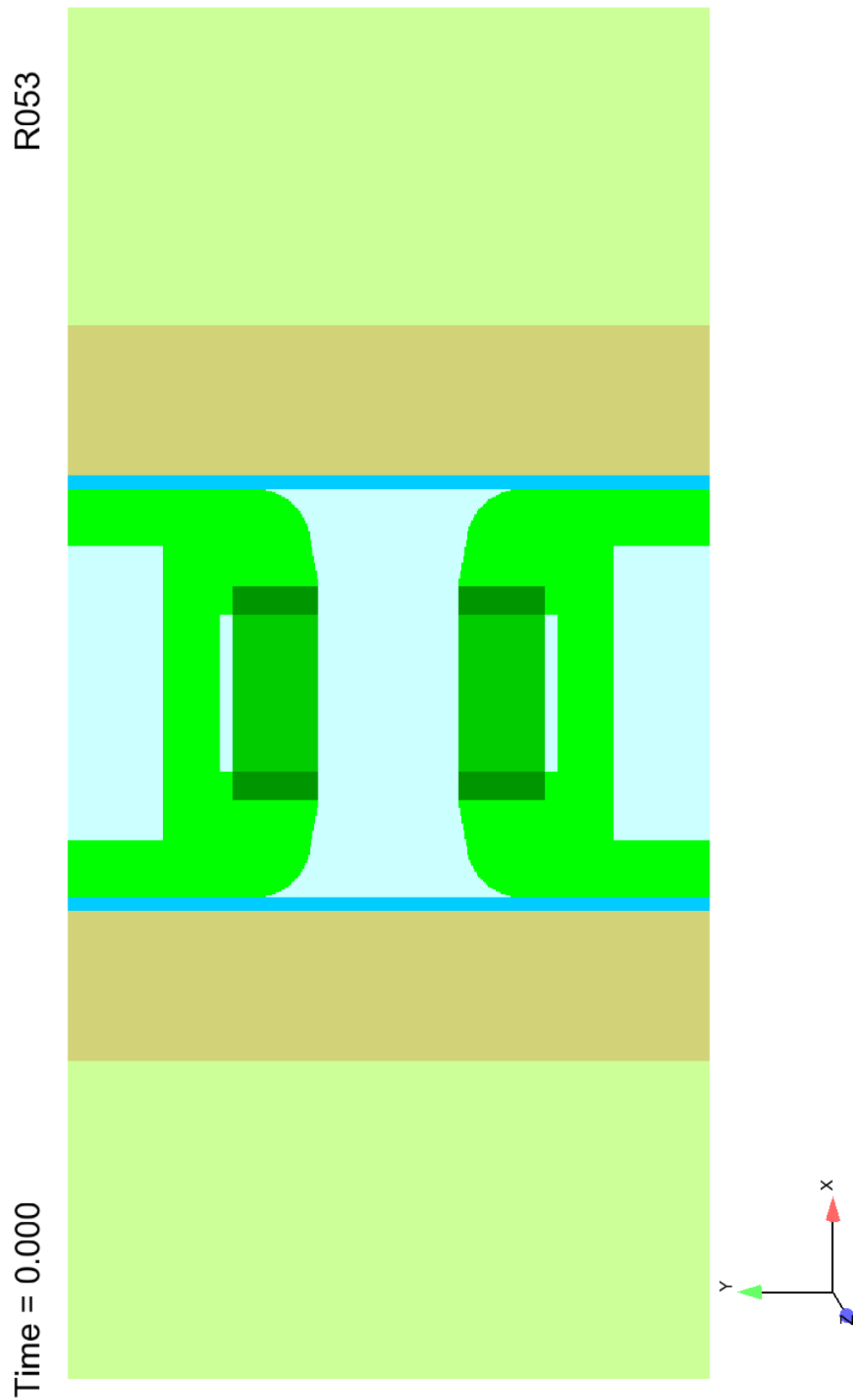


Figure 38: Assembly configuration at $t = 0\mu s$

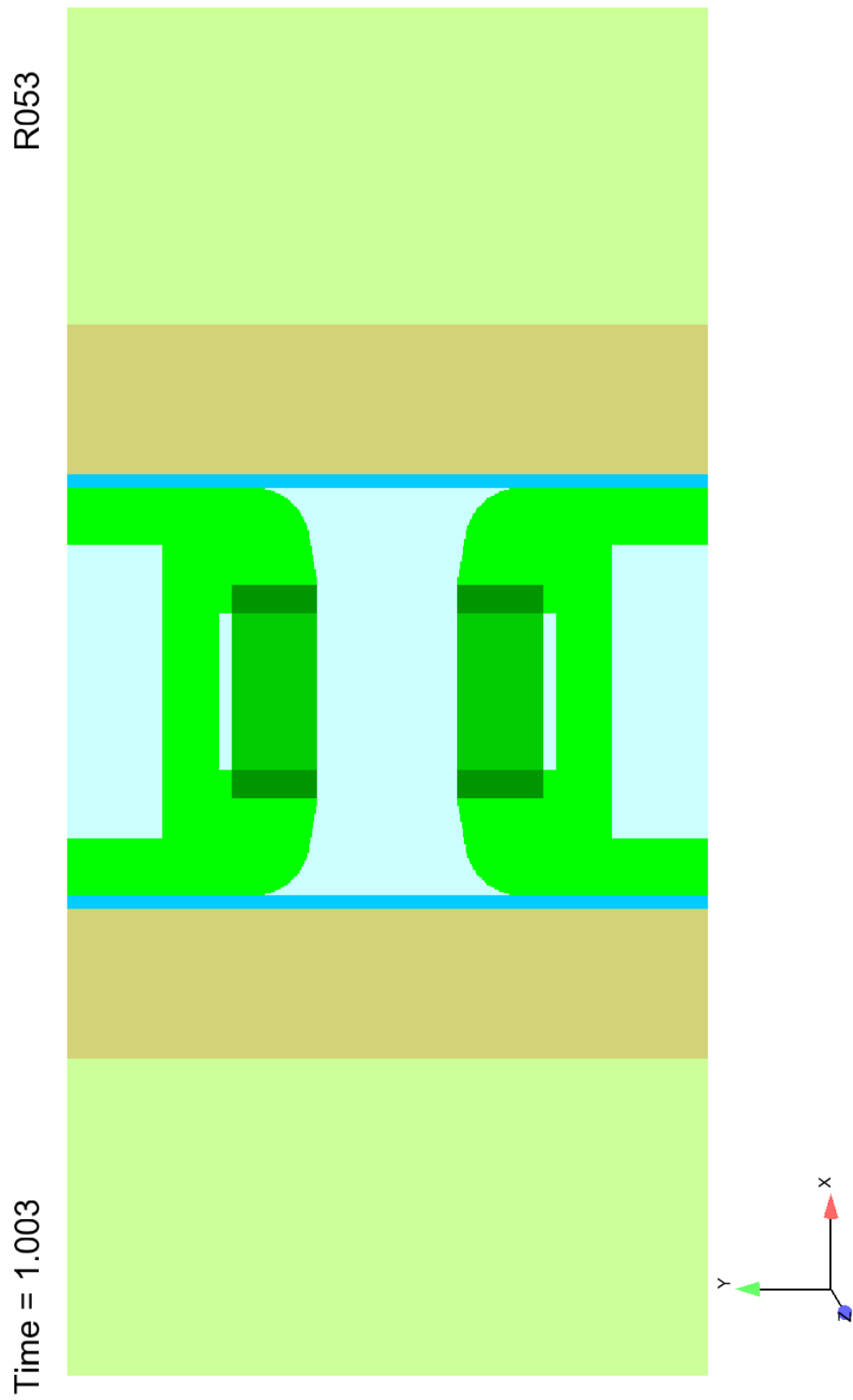


Figure 39: Assembly configuration at $t = 1\mu s$

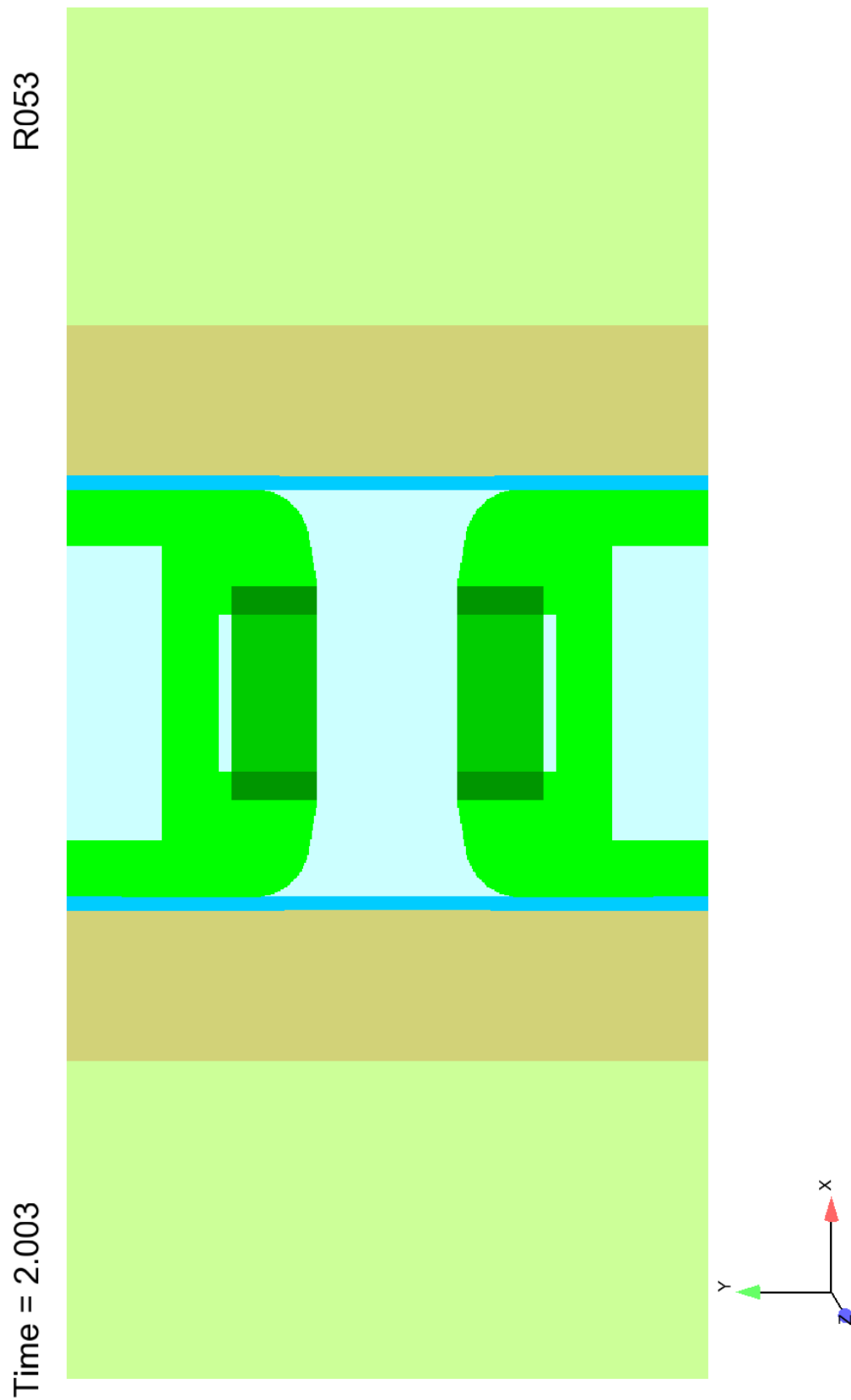


Figure 40: Assembly configuration at $t = 2\mu s$

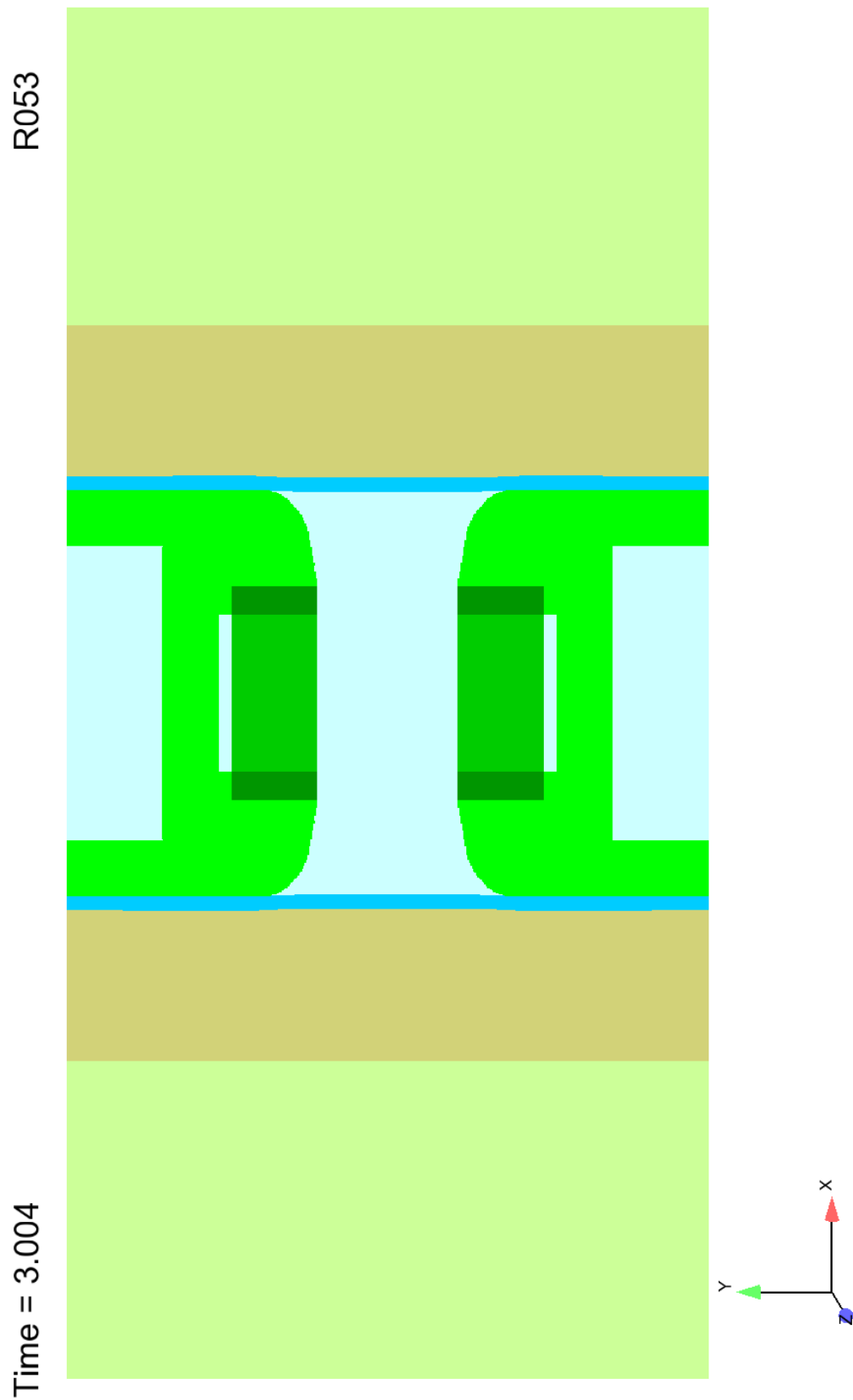


Figure 41: Assembly configuration at $t = 3\mu s$

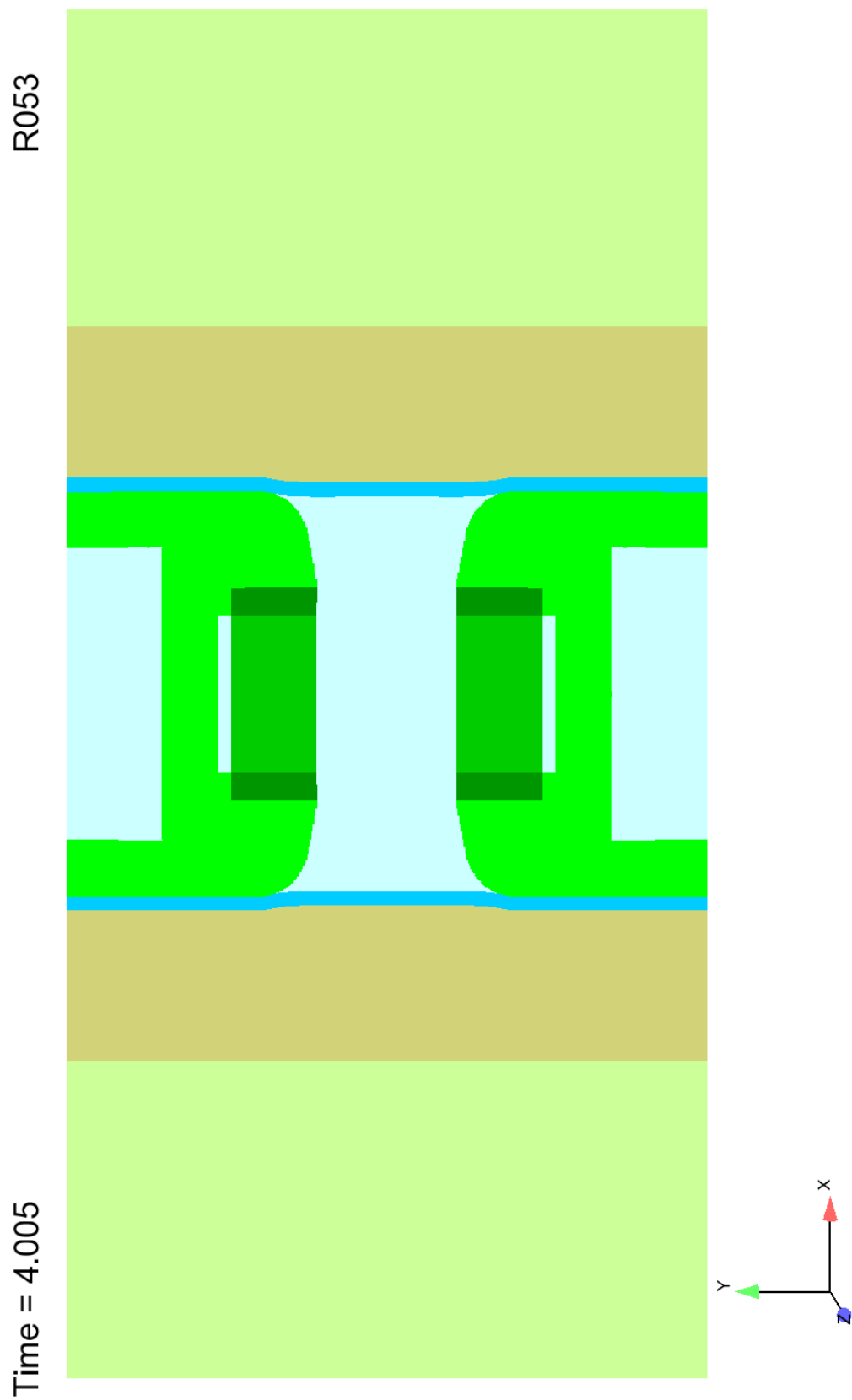


Figure 42: Assembly configuration at $t = 4\mu\text{s}$

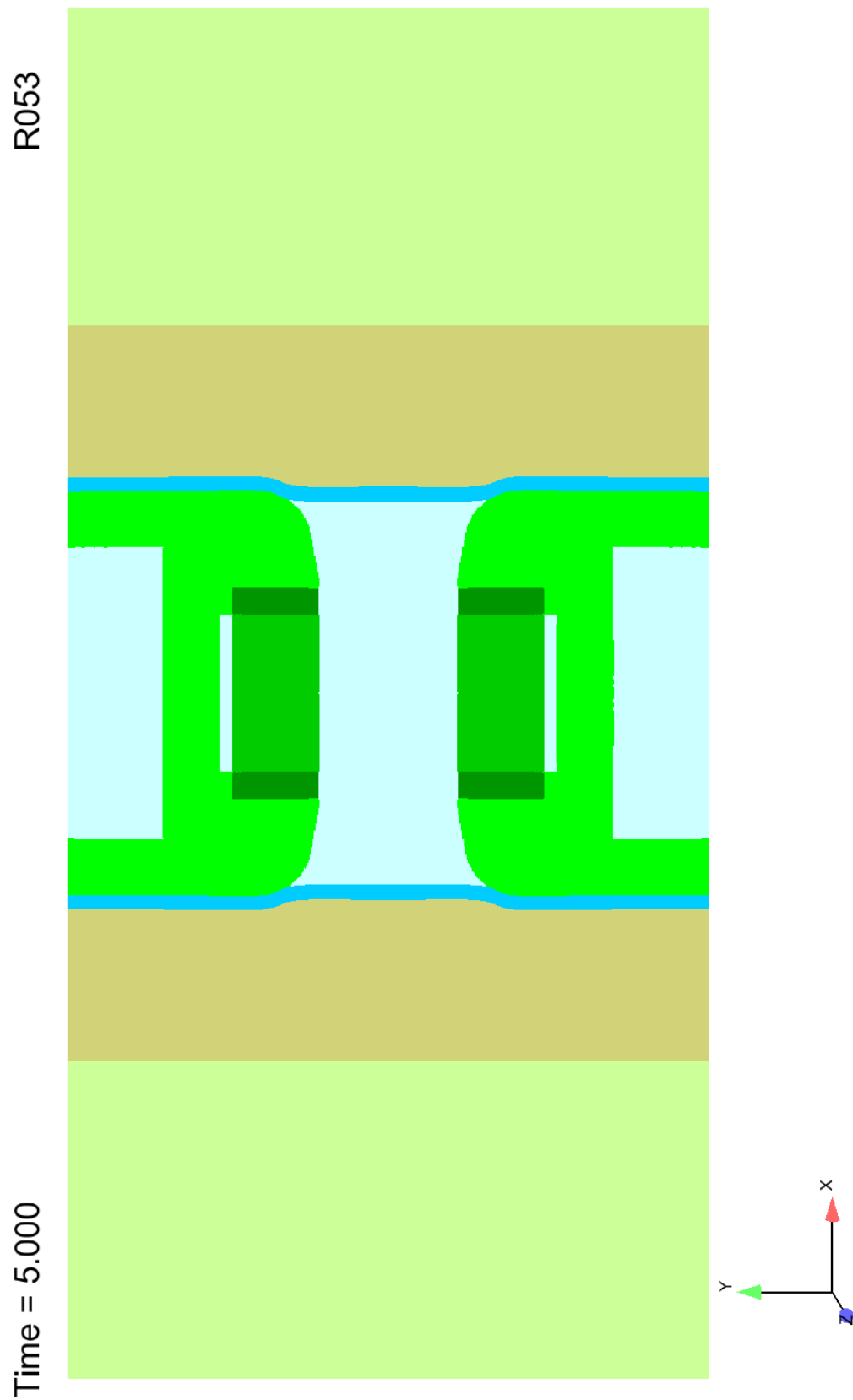


Figure 43: Assembly configuration at $t = 5\mu s$

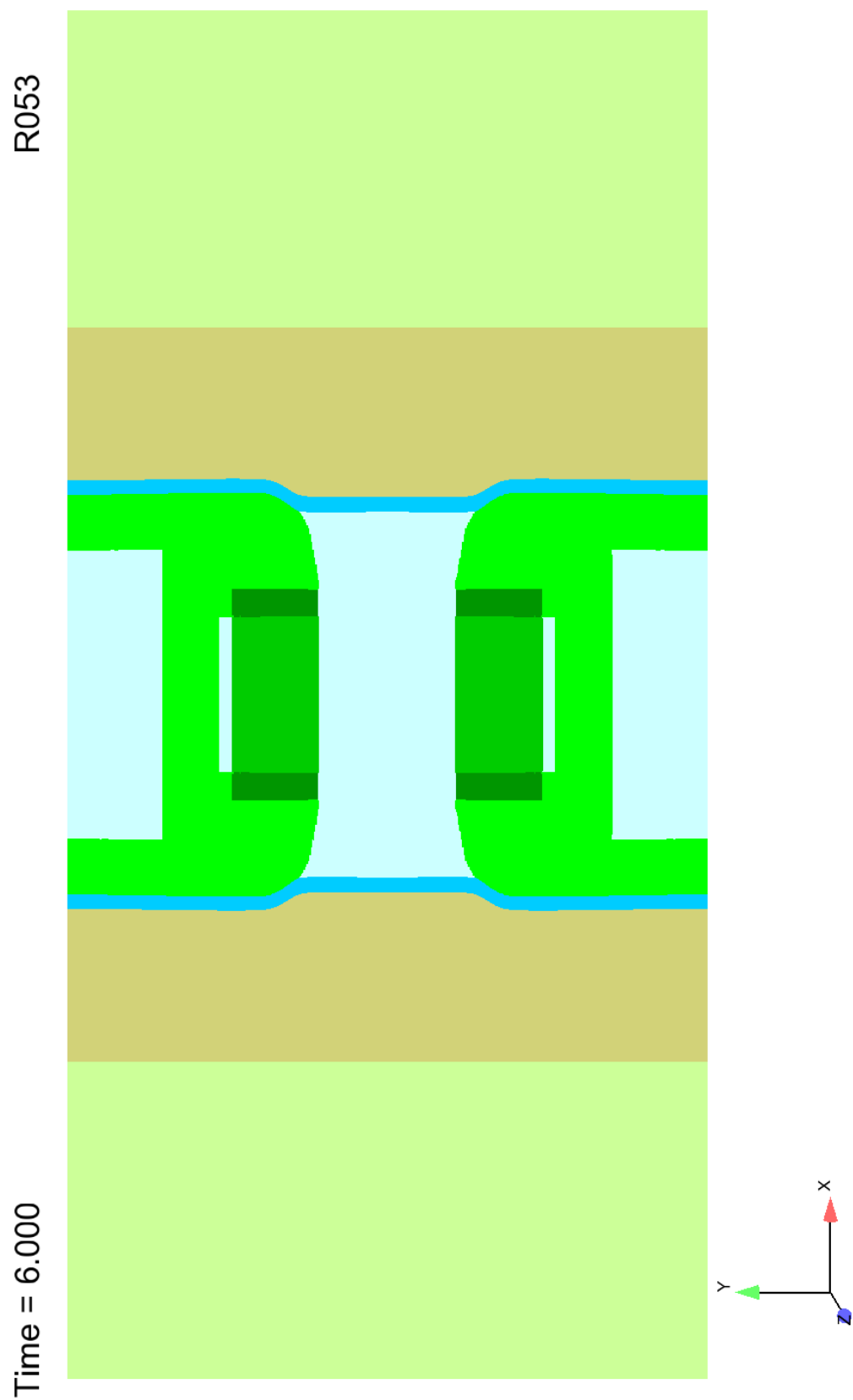


Figure 44: Assembly configuration at $t = 6\mu s$

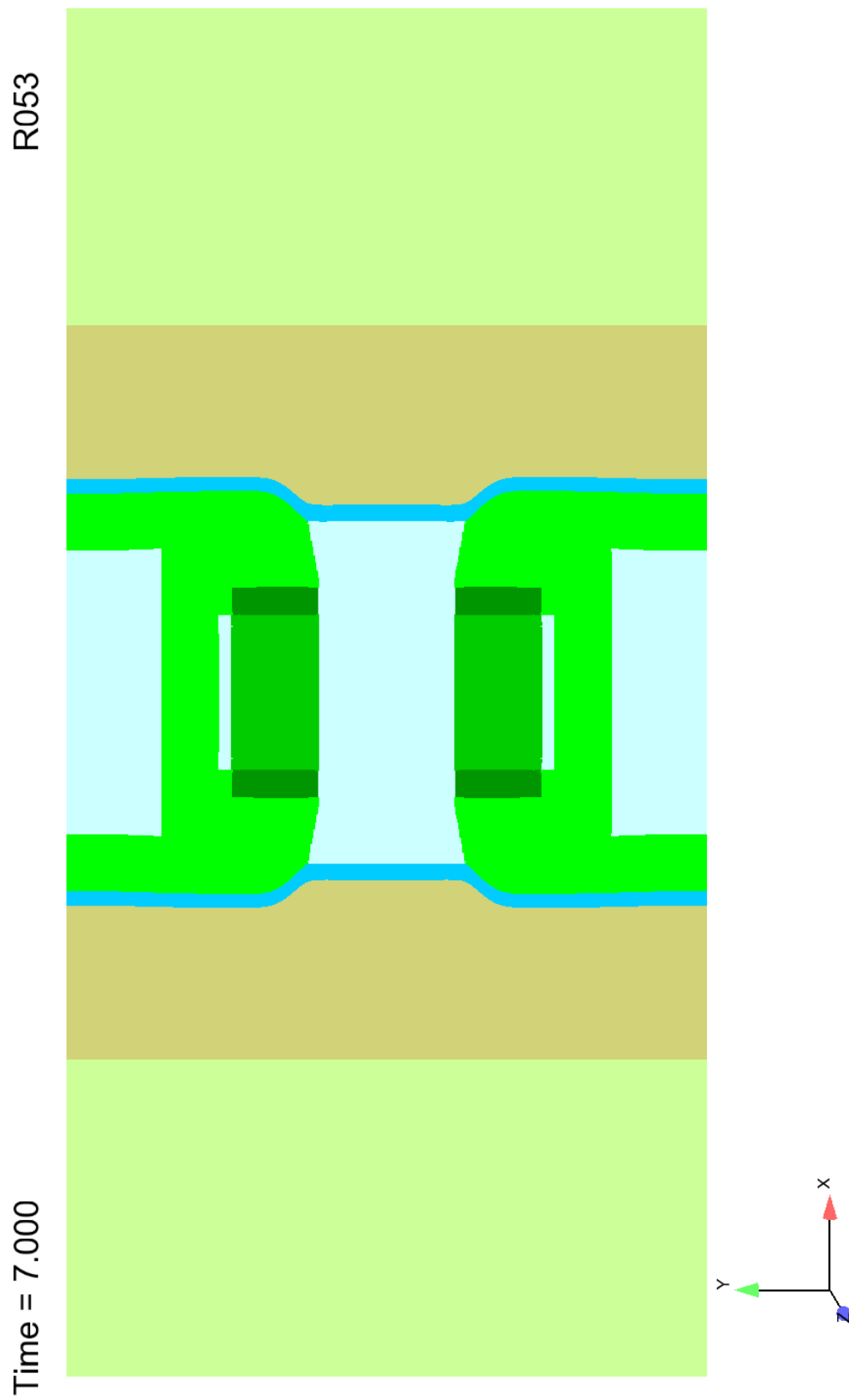


Figure 45: Assembly configuration at $t = 7\mu s$

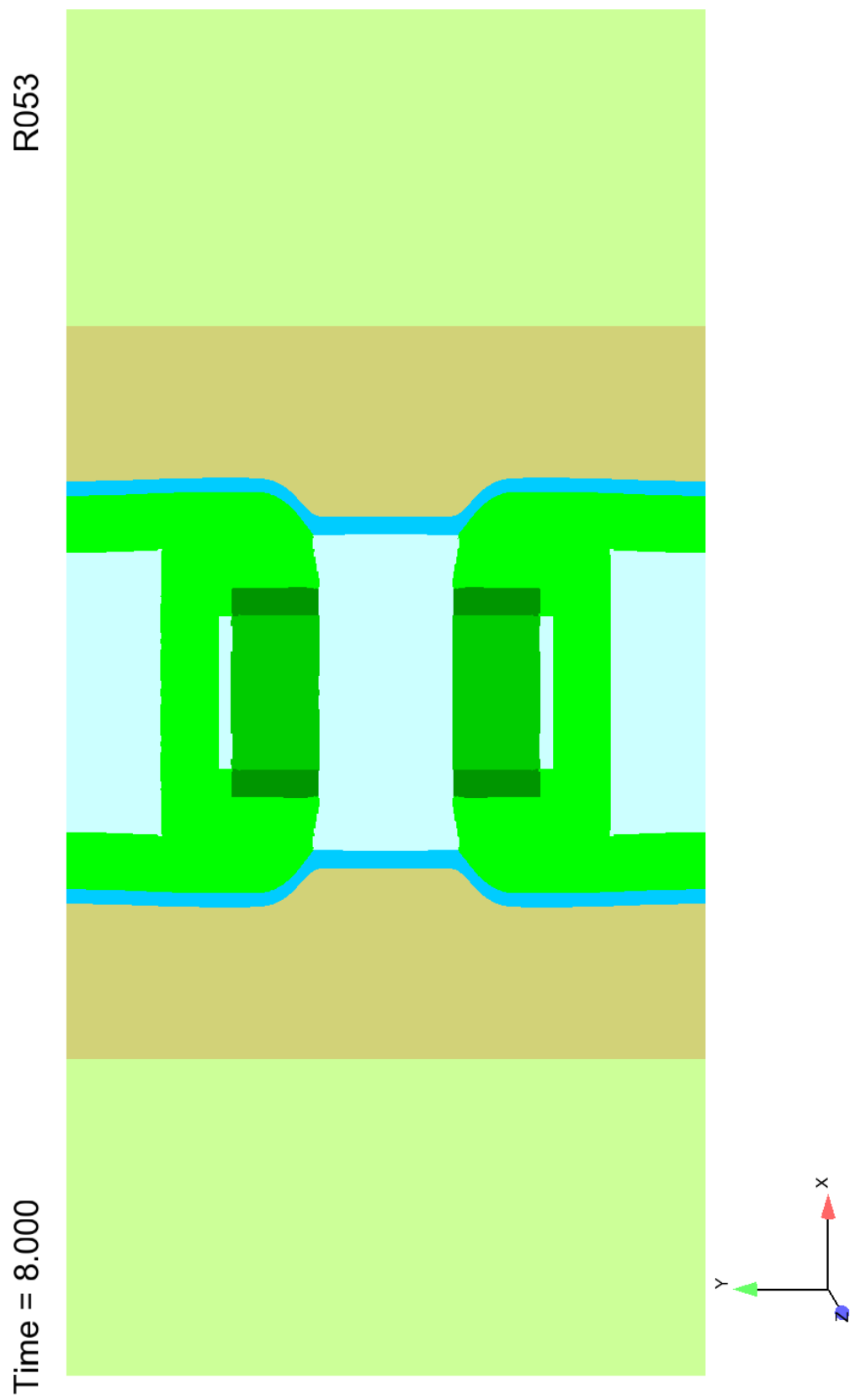


Figure 46: Assembly configuration at $t = 8\mu s$

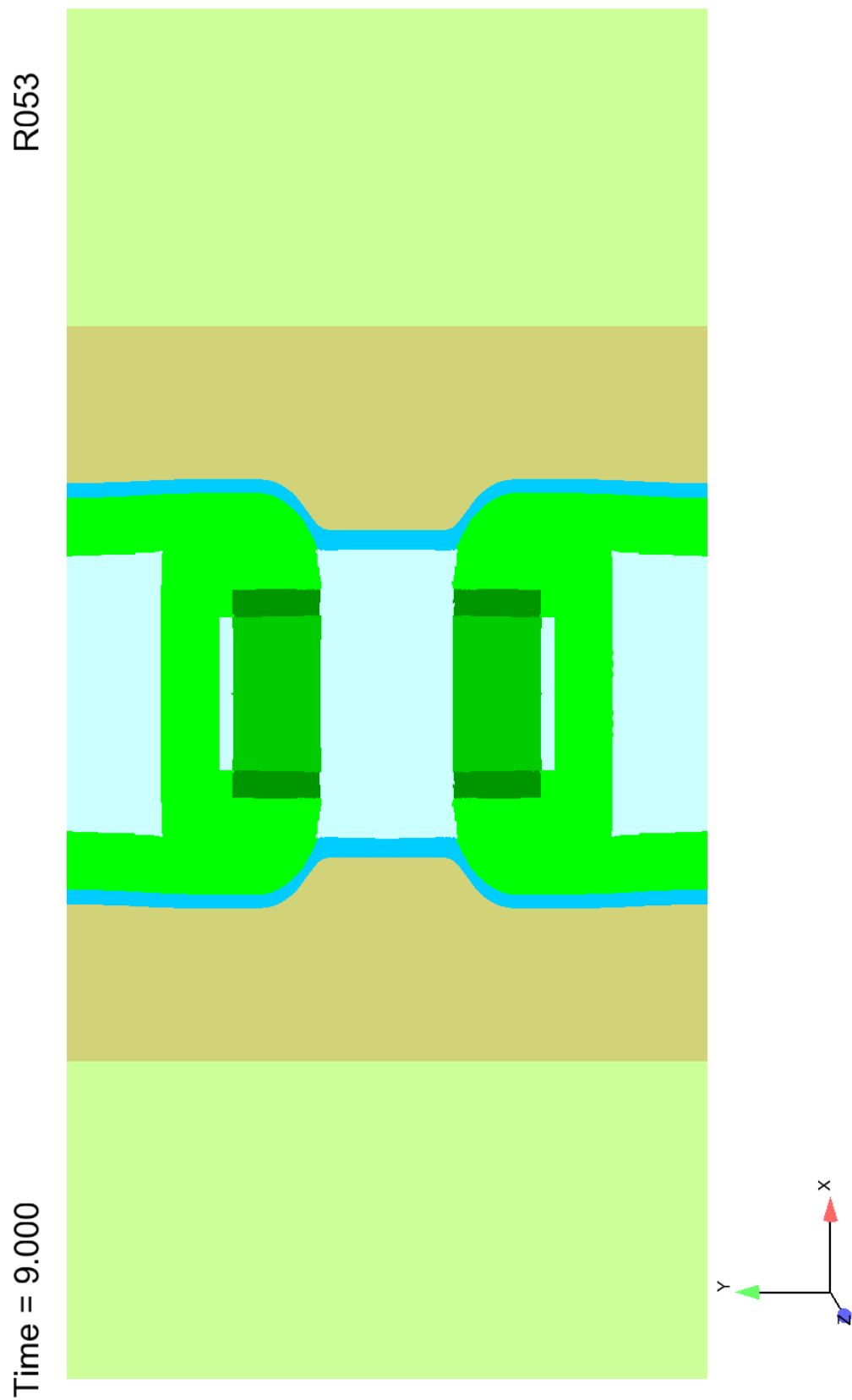


Figure 47: Assembly configuration at $t = 9\mu\text{s}$

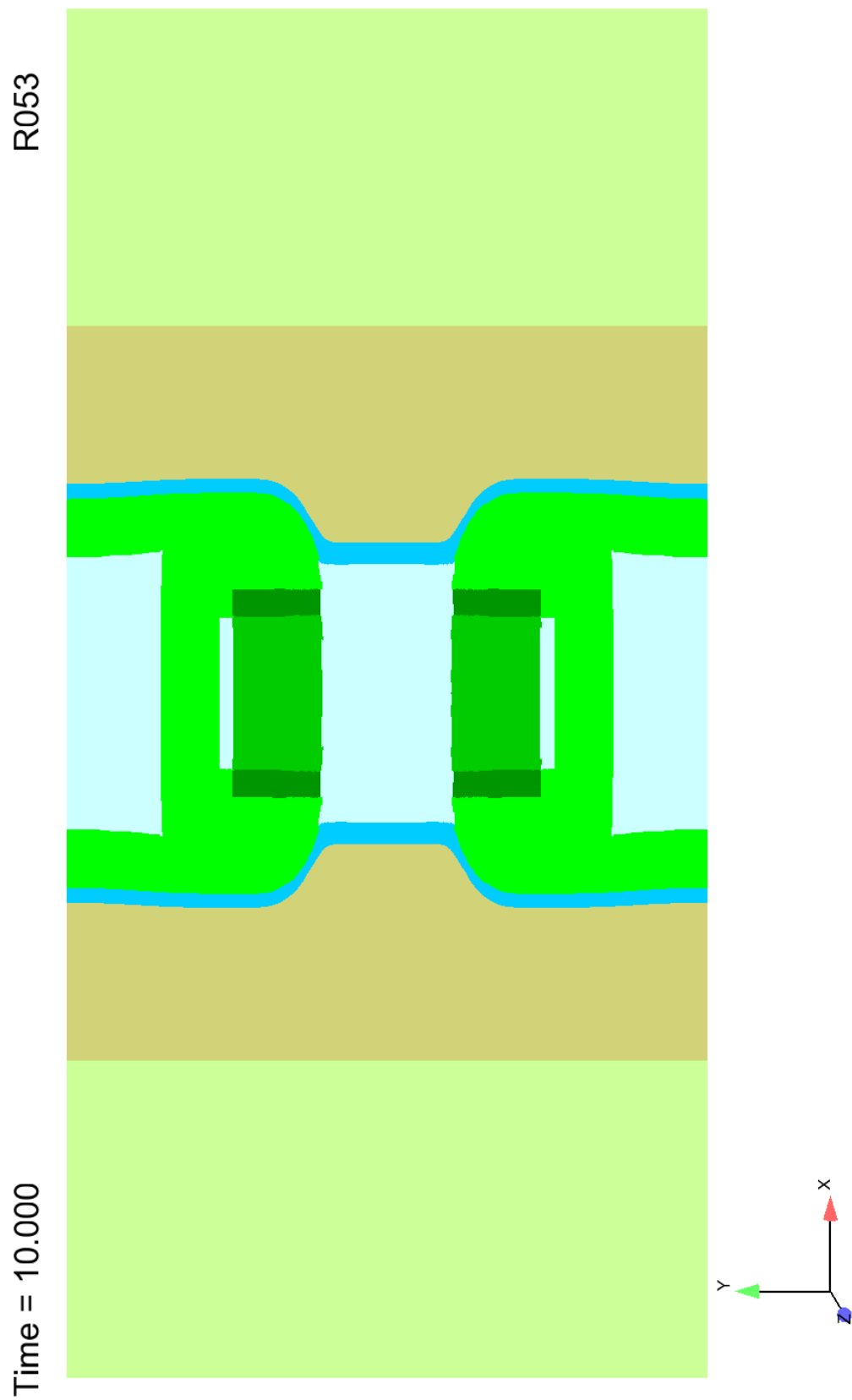


Figure 48: Assembly configuration at $t = 10\mu s$

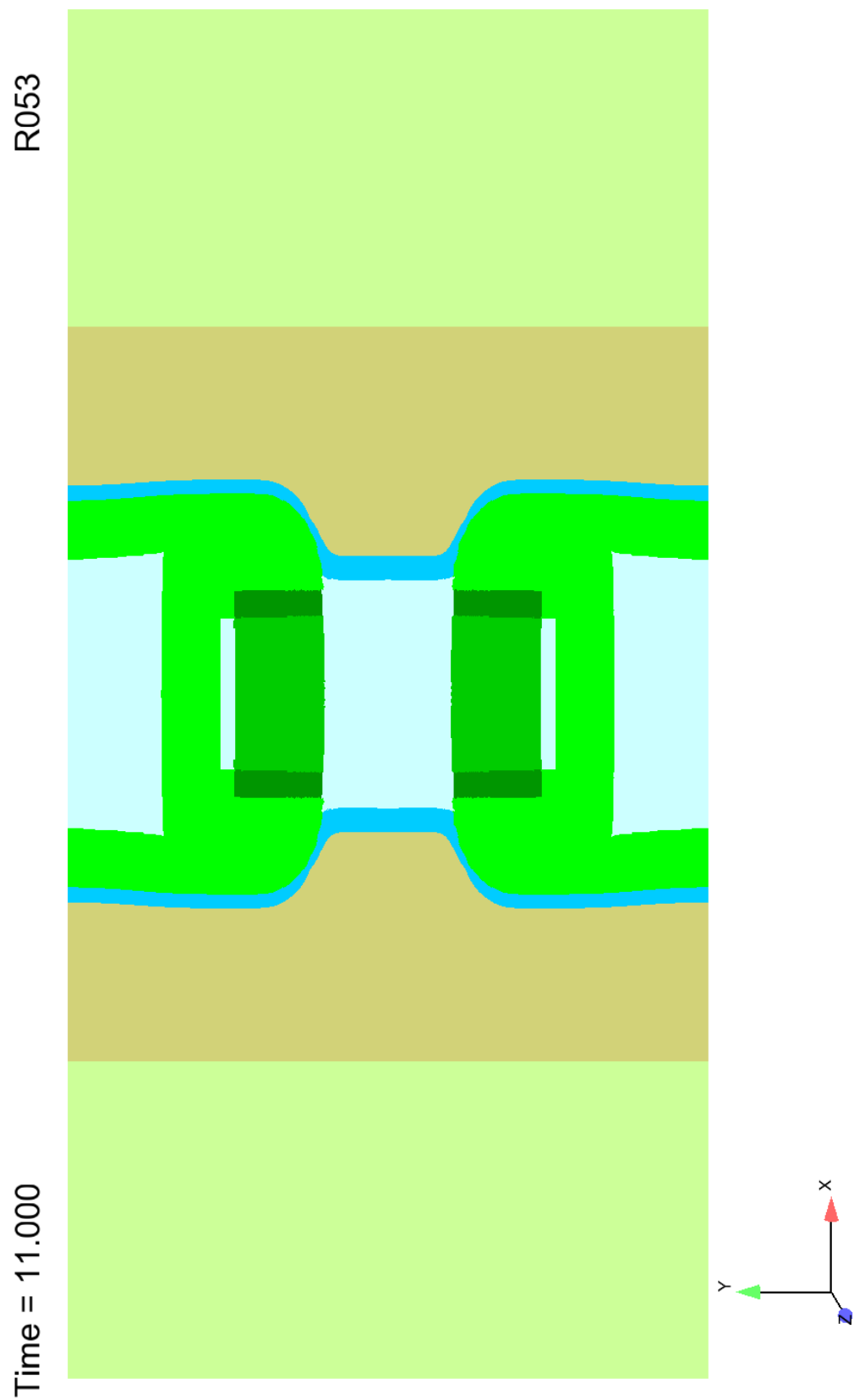


Figure 49: Assembly configuration at $t = 11\mu s$

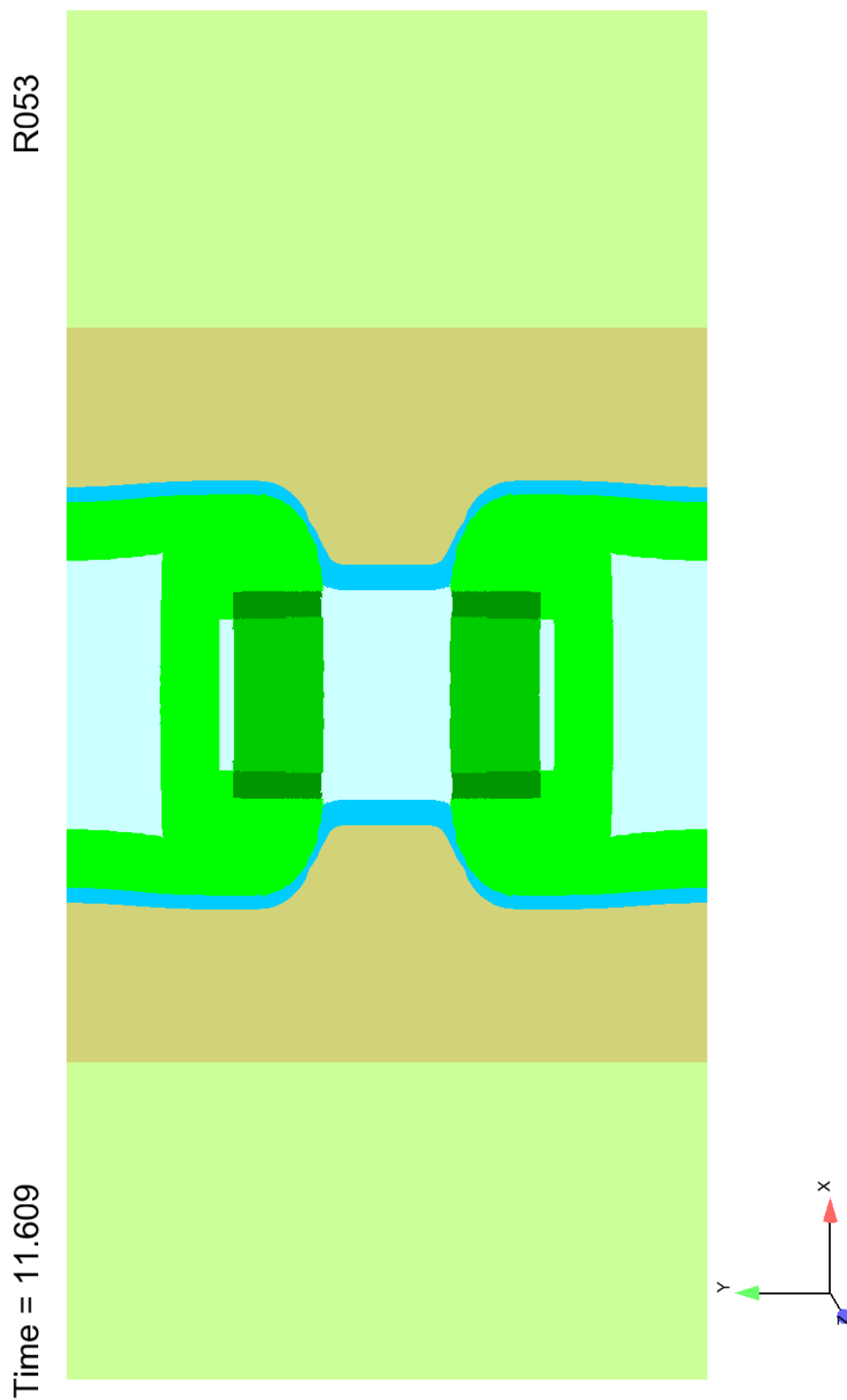


Figure 50: Assembly configuration at $t = 11.6\mu s$

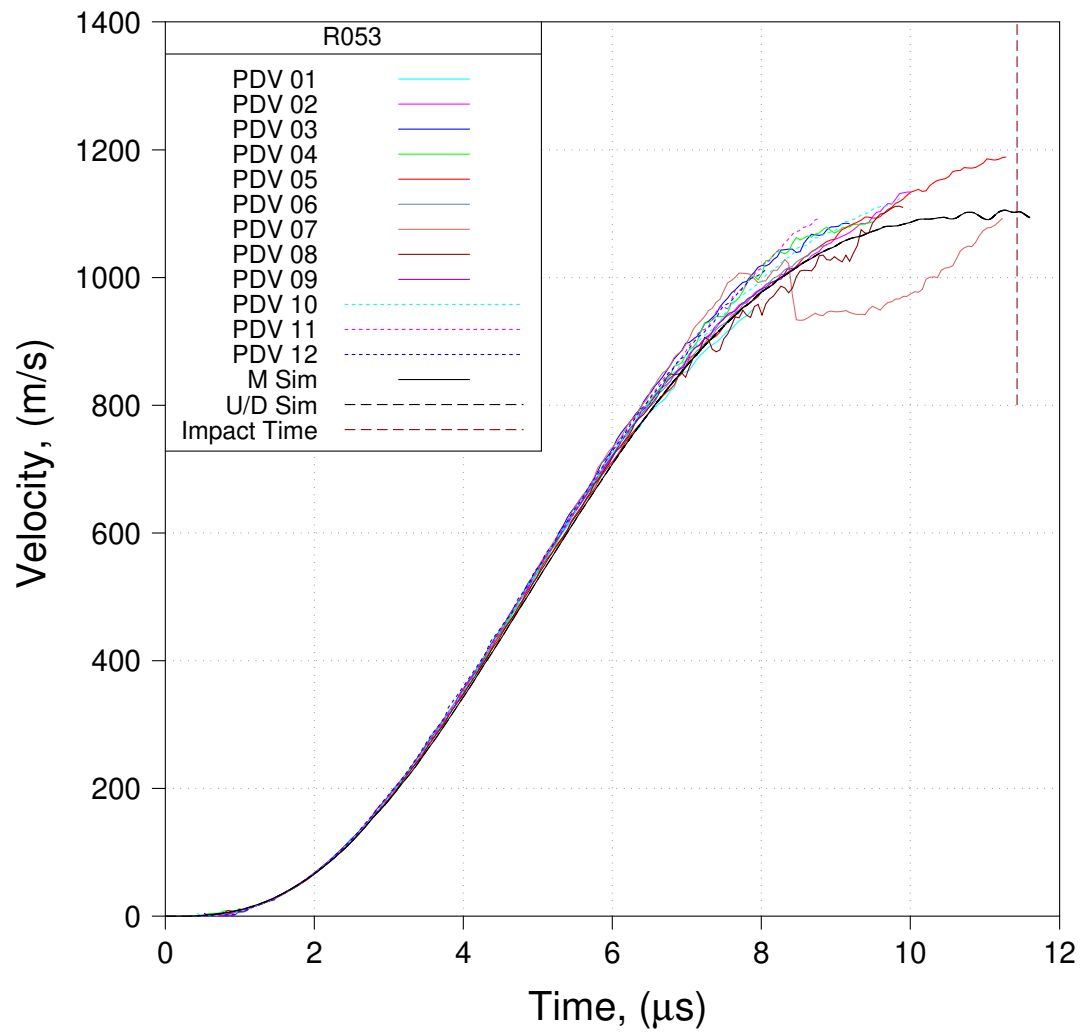


Figure 51: Comparison of predicted to measured velocities – R053

5.2.4 R054

While the results presented in the previous section look really good, it is important to realize that in obtaining those results we “cheated” a little. The nature of that “cheat” is that we used measured current as an input to our analysis rather than calculating the current. Thus we input a portion of the output to arrive at a better overall prediction. R054 is identical to R053 except that instead of using measured current as an input we calculate the current. The R054 results are presented in Fig. 52.

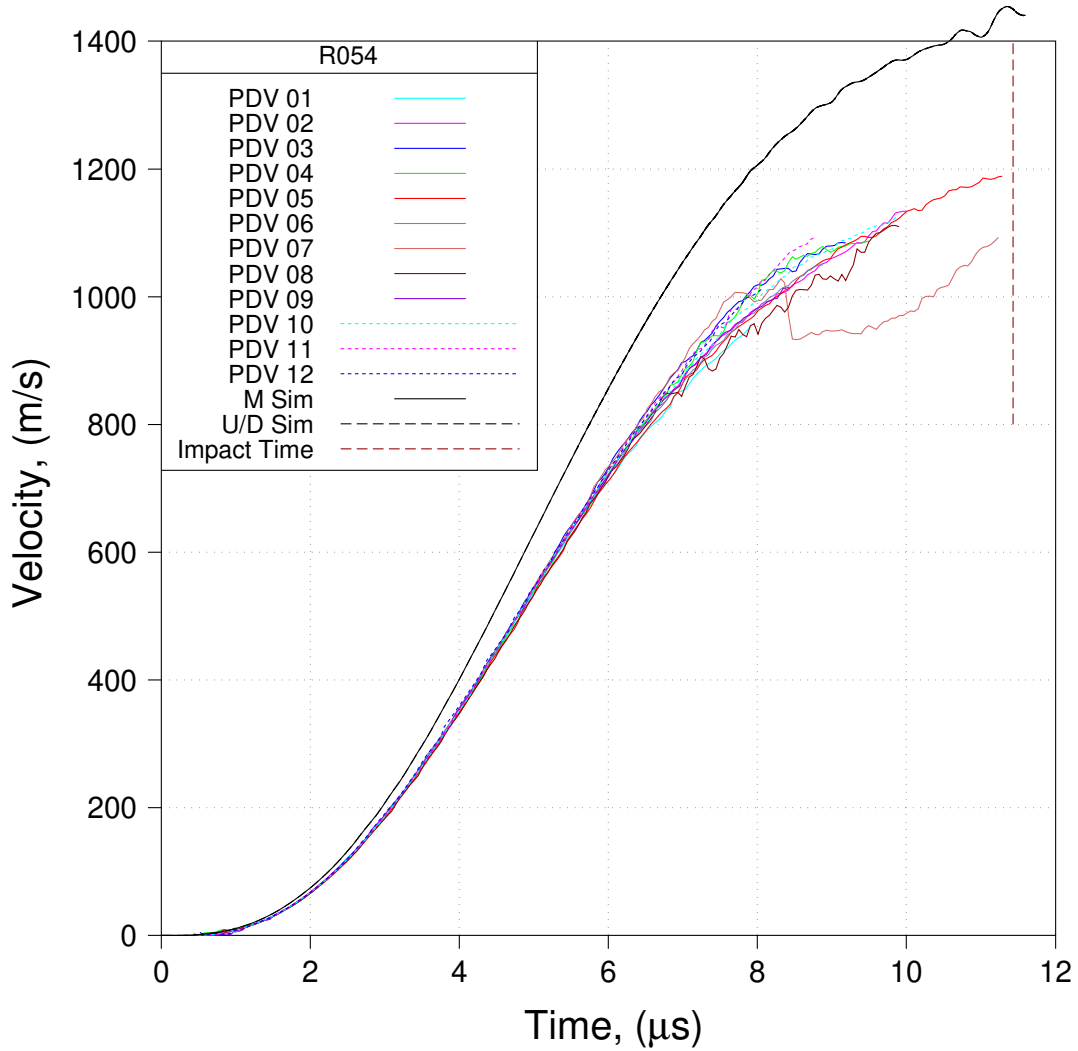


Figure 52: Comparison of predicted to measured velocities – Test 1 R054

5.3 Test 2 Pre-Shot Analysis

Our preshot simulations of Test 2 were conducted in identical fashion to those of Test 1, the only difference being the value of the driving potential, which was set to 75 kV in our simulation of Test 2. We note, for archival purposes, that our preshot simulation of Test 2 was conducted in Test 2: R000. We see no need to present in great detail the results of our pre-shot simulation of Test 2 (such as what was presented for Test 1 in Figs. 13-28) since those results differ little from those of Test 1.

We will state, however, that our pre-shot simulation of Test 2 suffered from the same inadequacies as our pre-shot simulation of Test 1. That is, we significantly over-predicted the peak midplane velocity, we predicted that at upstream/downstream locations the liner starts off moving in the wrong direction, and we observed a significant decrease in upstream/downstream velocities after about $9\ \mu\text{s}$ that was not observed in the experiment. See Figs. 53 and 54 for comparisons of pre-shot predictions to empirical data.

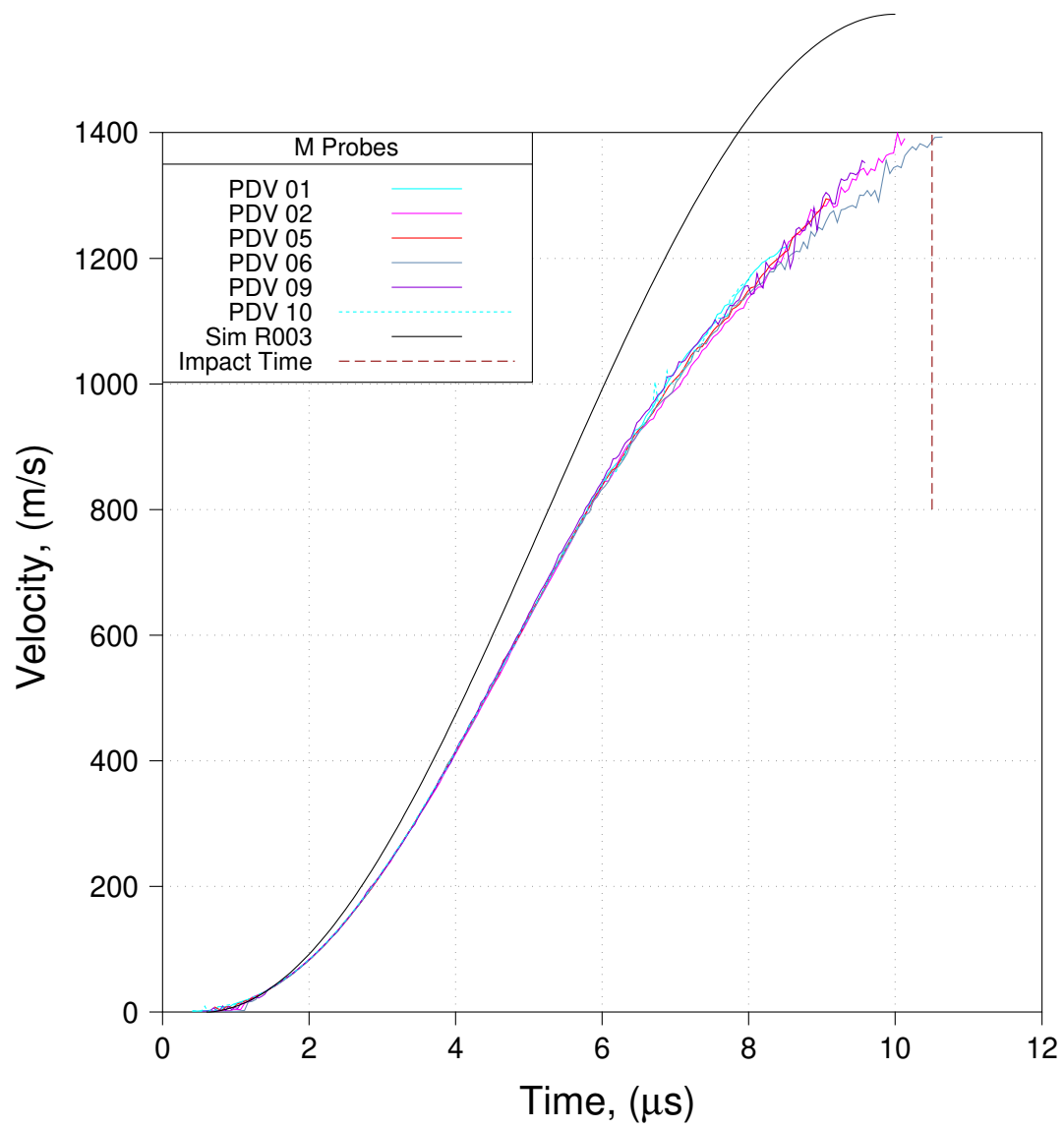


Figure 53: Comparison of pre-shot predicted to measured velocities – Test 2

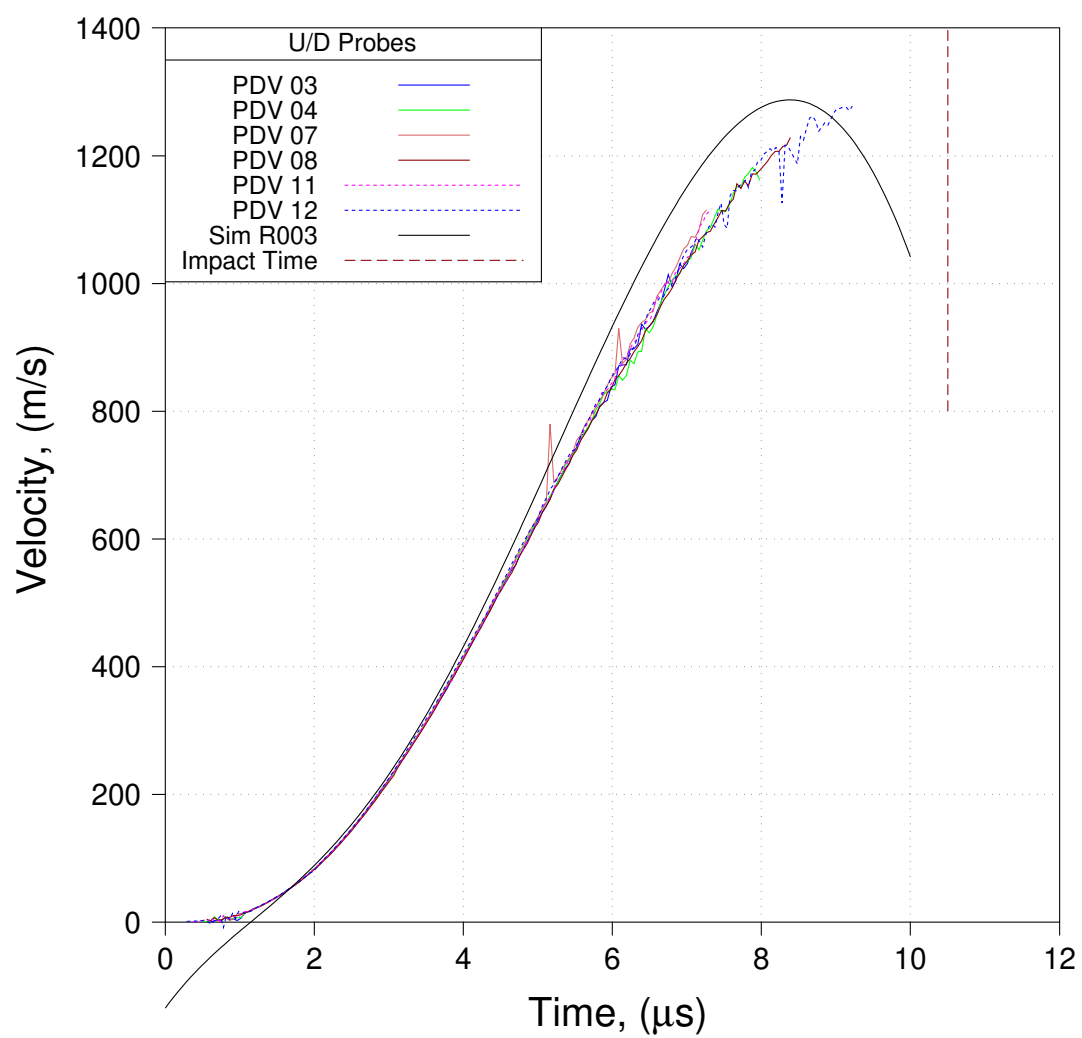


Figure 54: Comparison of pre-shot predicted to measured velocities – Test 2

5.4 Test 2 Post-Shot Analysis

5.4.1 R001

Test 2 simulation R001 corresponds exactly to Test 1 simulation R053. This is the simulation wherein measured current is used as an input in the analysis. The only difference between this run and Test 1 R053 is the driving potential is set here to 75 kV instead of 70 kV. Predicted velocities are compared to empirical data in Fig. 55.

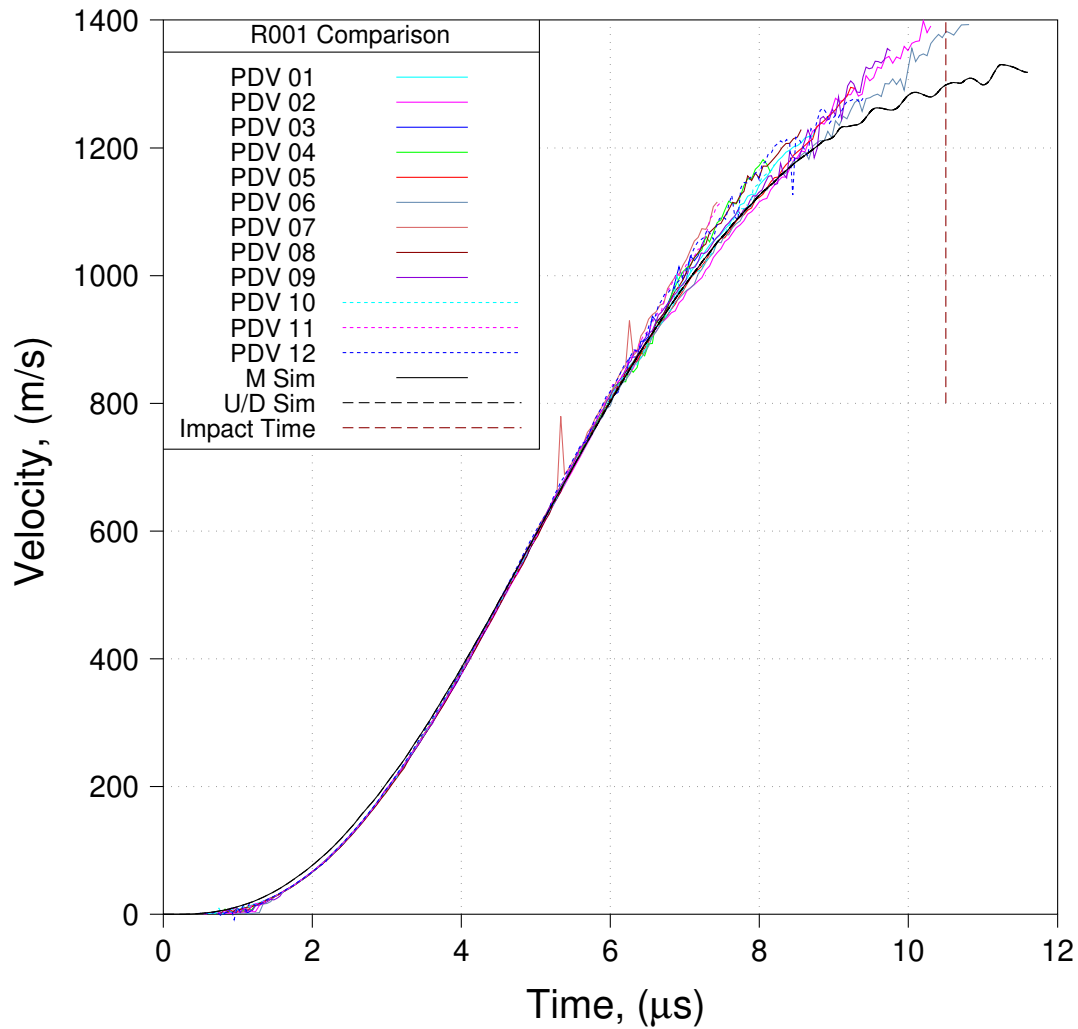


Figure 55: Comparison of pre-shot predicted to measured velocities – Test 2 R001

5.4.2 R002

Test 2 simulation R002 corresponds exactly to Test 1 simulation R054. This is the simulation wherein current is calculated within the analysis. The only difference between this run and Test 1 R054 is the driving potential is set here to 75 kV instead of 70 kV. Predicted velocities are compared to empirical data in Fig. 56.

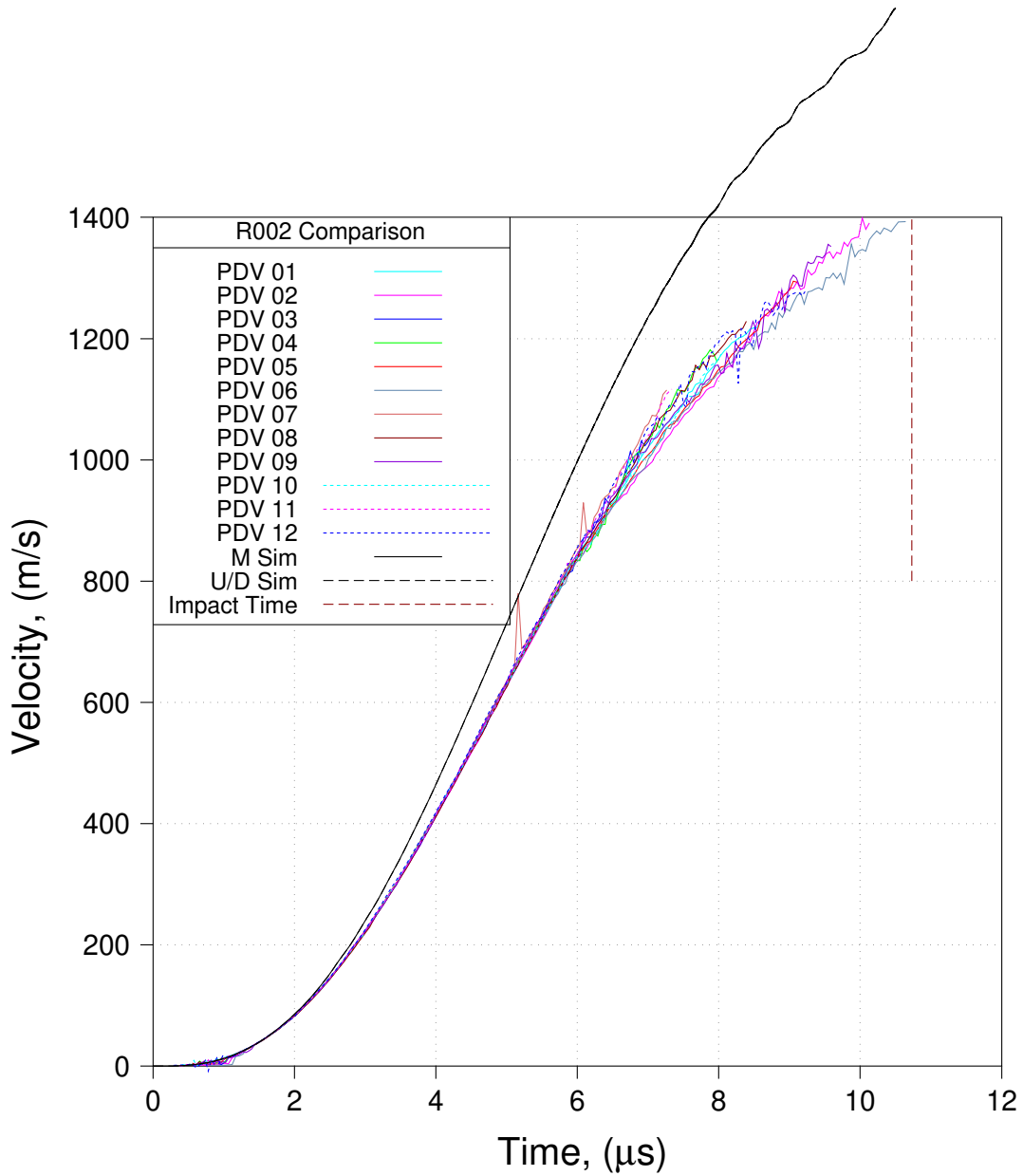


Figure 56: Comparison of pre-shot predicted to measured velocities – Test 2 R002

6 Conclusions

After following something of a trial-and-error-based approach to modeling these experiments, we have succeeded in demonstrating an ability to model, with reasonable accuracy, liner performance in the new shallow cassette PHELIX design configuration. At least this is the case when we get the electrical current right (see Figs. 53 and 55). It is worth mentioning that having to take something of a trial-and-error-based approach is not an indictment of the work conducted here, but rather an exercise of practicality in attempting to model a new design with many unknowns. For example, it was difficult to know *a priori* what would be the overall impedance of this new design.

We have also clearly demonstrated that our initial guesses (Table 8) as to what are the appropriate values of the various parameters required by the RLC circuit analysis are inadequate (see Figs. 29 and 57). This is not surprising, since as mentioned above, we were dealing with a new design and it was difficult to know *a priori* what the electrical characteristics of that new design would be. Work has commenced to determine what the parameter set for the RLC circuit analysis should be. We plan to present that work in a follow-up publication that is to appear in the very near future.

One final comment, relaxation region R05 is much larger than is necessary. In future analysis it is quite probable that refinement with respect to the overall relaxation scheme will result in a much smaller R05 region.

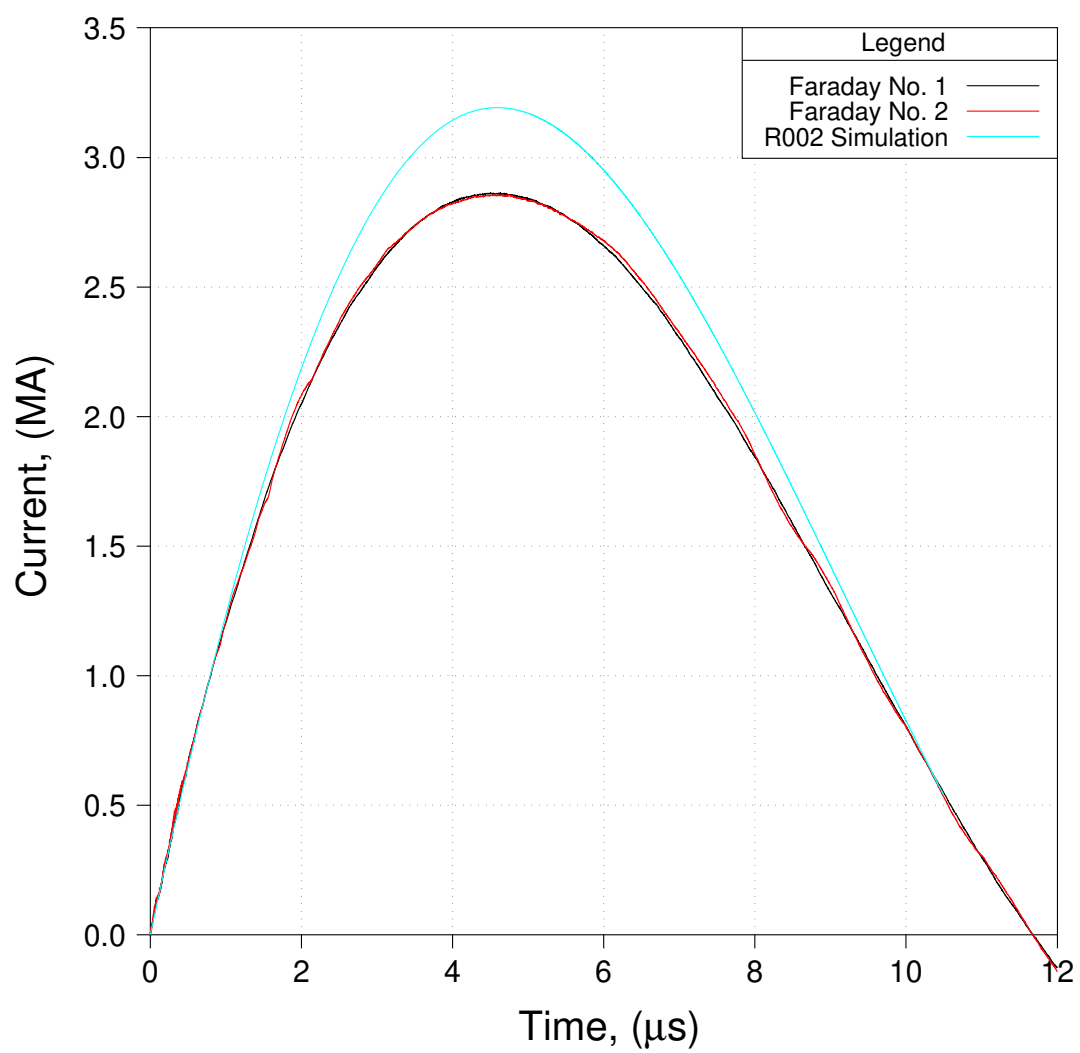


Figure 57: Predicted current compared to measured current – Test 2

References

- [1] D. E. Burton, “Lagrangian Hydrodynamics in the FLAG Code,” LANL Report No. LA-UR-07-7545, Los Alamos National Laboratory, Los Alamos, NM, USA, 2007.
- [2] M. Berndt, M. Kucharik, and M. Shashkov *Procedia Computer Science*, vol. 1, no. 1, pp. 1885–1892, 2010.
- [3] D. G. Steinberg, S. G. Cochran, and M. W. Guinan *Journal of Applied Physics*, vol. 51, no. 3, pp. 1498–1504, 1980.
- [4] F. A. Lindemann *Physikalische Zeitschrift*, vol. 11, pp. 609–612, 1910.
- [5] D. E. Burton, “Multidimensional Discretization of Conservation Laws for Unstructured Polyhedral Grids,” LLNL Report No. UCRL-JC-118306, Lawrence Livermore National Laboratory, Livermore, CA, USA, 1994.
- [6] D. L. Preston, D. L. Tonks, and D. C. Wallace *Journal of Applied Physics*, vol. 93, no. 1, pp. 211–220, 2003.
- [7] M. A. Zocher, J. Plohr, and L. Burakovsky *MDPI Applied Sciences*, vol. 10, no. 20, p. 7209, 2020.
- [8] D. L. Youngs, “Time-Dependent Multi-Material Flow with Large Fluid Distortion,” in *Numerical Methods for Fluid Dynamics* (K. Morton and M. Baines, eds.), pp. 273–285, Academic Press, 1982.
- [9] D. L. Youngs, “An Interface Tracking Method for a 3d Eulerian Hydrodynamics Code,” AWRE Technical Report 44/92/35, Atomic Weapons Research Establishment, Aldermaston, UK, 1984.